THE TRANSITION TO ADHESIVE WEAR OF LUBRICATED CONCENTRATED CONTACTS

Mark van Drogen

De promotiecommissie is als volgt samengesteld:

prof. dr. ir. L. van Wijngaarden, Universiteit Twente, voorzitter en secretaris
prof. dr. ir. D.J. Schipper, Universiteit Twente, promotor
prof. dr. ir. A. de Boer, Universiteit Twente
prof. dr. ir. Th.H. van der Meer, Universiteit Twente
prof. dr. ir. F.J.A.M. van Houten, Universiteit Twente
prof. dr. ir. P. de Baets, Universiteit Gent, België
prof. dr. ir. P.M. Lugt, Luleå Technical University, Zweden

Drogen, Mark van
THE TRANSITION TO ADHESIVE WEAR OF LUBRICATED CONCENTRATED CONTACTS
Ph.D. Thesis, University of Twente, Enschede, the Netherlands
December 2005

ISBN 90-365-2286-2

Keywords: Tribology, transition diagram, contact model, adhesive wear, contact temperature, roughness.

Printed by PrintPartners Ipskamp B.V., Enschede, the Netherlands

THE TRANSITION TO ADHESIVE WEAR OF LUBRICATED CONCENTRATED CONTACTS

PROEFSCHRIFT

ter verkrijging van
de graad van doctor aan de Universiteit Twente,
op gezag van de rector magnificus,
prof. dr. W.H.M. Zijm,
volgens besluit van het College voor Promoties
in het openbaar te verdedigen
op vrijdag 2 december 2005 om 15.00 uur

door

Mark van Drogen

geboren op 4 februari 1972
te Enschede

Dit proefschrift is goedgekeurd door:

Promotor: prof. dr. ir. D.J. Schipper

voor Eva
voor Bertus en Gré

Samenvatting

Machineonderdelen worden steeds zwaarder belast en daarom worden er steeds hogere eisen gesteld aan de ontwerpspecificaties. Om tot zo'n specificatie te komen heeft de ingenieur ontwerprichtlijnen nodig. In dit proefschrift wordt een ontwerpdiagram gepresenteerd dat gebruikt kan worden om te voorkomen dat twee in contact zijnde mechanische componenten falen als gevolg van adhesieve slijtage.

Adhesieve slijtage, ofwel vreten, kan voorkomen worden door te zorgen dat grenslagen, gevormd door additieven in het smeermiddel, onder alle bedrijfsomstandigheden aanwezig zijn tussen de beide contactoppervlakken. Er kan dan overigens nog steeds sprake zijn van slijtage, echter van een veel mildere vorm dan adhesieve slijtage en die niet tot sterk afnemend functioneel gedrag leidt. Het ontwikkelde ontwerpdiagram heeft betrekking op de voorspelling van de overgang van de milde naar de adhesieve slijtagevorm voor gesmeerde geconcentreerde contacten.

Op basis van de hypothese van Blok, die zegt dat een contact faalt als een bepaalde kritische contacttemperatuur wordt overschreden, is een analyse gemaakt waarbij de optredende contacttemperatuur berekend kan worden. Voorheen werden hiervoor alleen contacttemperatuurberekeningen gemaakt op basis van macro-contacteigenschappen en werden (flits)temperaturen in ruwheidscontacten niet meegenomen. In dit proefschrift wordt van een andere aanpak gebruik gemaakt, waarbij (flits)temperaturen tussen ruwheidtoppen wel worden meegenomen.

Om tot een thermisch model te komen, is er eerst een deformatiemodel nodig dat het contact voorspelt, zowel op macro- als microschaal. Hiervoor is een deterministisch contactmodel opgesteld, waarin per ruwheidscontact de belasting en contactoppervlak berekend kan worden. De deformatie van de ruwheidstoppen kan elastisch, plastisch of – in een gemengde vorm – elastisch-plastisch van aard zijn. Hiervan gebruik makend is het mogelijk de totale lokale contacttemperatuur te berekenen.

De contacttemperatuur is berekend als functie van diverse invloedsfactoren en is weergegeven in zgn. F/v-diagrammen. Tezamen met een bepaalde kritische temperatuur kan nu de transitie van een milde naar een adhesieve slijtagevorm aangegeven worden. Een gecombineerd transitiediagram is opgesteld waarin de invloedsfactoren langs de assen zijn weergegeven in de vorm van gemodificeerde F- en v-parameters.

Validatiemetingen zijn uitgevoerd in de vorm van pen-schijfmetingen, waarbij de pen bestaat uit een cilindrisch lichaam en dat in contact met de schijf resulteert in een lijncontact. Hiervoor is een speciale pen-schijftribotester ontworpen die geschikt is voor hoge belastingen. Er kan worden geconcludeerd dat de uit metingen resulterende transities goed worden voorspeld door het in dit proefschrift opgestelde contacttemperatuurmodel, dit in tegenstelling tot de uit de literatuur bekende berekeningsmethodes voor de contacttemperatuur.

Het ontwikkelde gecombineerde transitiediagram stelt de ontwerper in staat machineonderdelen veilig te laten functioneren in het milde slijtagegebied, omdat de overgang van milde naar adhesieve slijtage bekend is.

Summary

Engineering components are subjected to more extreme operating conditions nowadays and this leads to higher demands with regard to design specifications. In order to set-up these specifications, engineers need guidelines to achieve an optimal design. In this thesis an engineering diagram is presented which can be used to prevent two contacting mechanical components from failing by adhesive wear.

Adhesive wear or scuffing can be prevented by boundary layers, formed by additives in the lubricant, being present between the contacting surfaces under all operating conditions. Now, milder types of wear occur which do not lead to strong decreasing functional behaviour. The transition from mild to adhesive wear can be predicted using the engineering diagram which is developed for lubricated concentrated contacts.

An analysis is made based on the hypothesis of Blok, i.e. a contact fails when a certain critical contact temperature is exceeded. Up to now, contact temperature calculations were only made based on macro contact characteristics and (flash) temperatures due to roughness interactions were not considered. In this thesis a different approach is used, in which (flash) temperatures between the contacting roughness summits are taken into account.

In order to develop a thermal model, first a deformation model is needed which can predict the contact, both on macro and micro scale. For this purpose a deterministic contact model is developed, in which per summit contact the load and contacting area can be calculated. The deformation of the summits can be elastic, plastic or – in a mixed form – elastic-plastic. When knowing this, the total local contact temperature can be calculated.

The contact temperature is calculated as a function of several factors of influence and is presented in so-called F/v diagrams. Together with a certain critical temperature the transition from a mild to adhesive wear region can be determined. Furthermore, a combined transition diagram is constructed in which the factors of influence, in the form of adapted F and v parameters, are denoted along the axes.

Validation measurements are carried out by means of pin-on-disk measurements, in which the pin consists of a cylindrical element, resulting in a line contact situation in contact with the disk. For these measurements a special high load pin-on-disk tribotester has been developed. From the experiments can be concluded that the measured transitions are well predicted by the model which is developed in this thesis, in contrast to the calculation models known from literature.

The developed combined transition diagram enables the designer to allow engineering components to function safely in the mild wear region, because the transition from mild to adhesive wear is known.

Acknowledgements

I would like to thank everyone who contributed to this thesis.

I especially thank my promotor prof. dr. ir. D.J. Schipper, for his guidance, support, ideas and many useful discussions.

Special thanks to ir. W.E. ten Napel, who introduced me to the field of tribology with great enthousiasm.

I would like to thank my collegues for their contribution: Arie van der Velde, Arjan van der Leest, Arjen Brandsma, Duc Tran, Francis van der Sluis, Gabriël Plevier, Gerard van Dijnsen, Gert-Jan van Spijk, Ingmar Hupkes, Lili Crebolder, Maaike van der Laan, Marlène Lemmens, Paul Faes, Pieter Pennings and Toon van Hout. Very special thanks are deserved by Bert Pennings for countless enjoyable conversations and discussions, and for his assistance as paranimf.

Furthermore, special thanks to Antoine Melis who skilfully took care of everything involved with the tribotester and for great discussions and support, Jean-Pierre van Eijndhoven for numerous measurements and Bas Mutsaers and his group members for all the CAD work. Moreover, I would like to thank the students Jan van Cromvoirt and Erwin van de Louw who worked with me on this project.

As a distant member of the Surface Technology and Tribology group of the University of Twente, I very much enjoyed the nice working atmosphere with numerous discussions and lots of coffee, whenever I was in Twente. Thanks to the staff members: Belinda Bruinink, Dik Schipper, Erik de Vries, Kees Venner, Matthijn de Rooij, Walter Lette, Wijtze ten Napel and Willie Kerver, and all the Ph.D. students, especially Irinel Faraon for all the pleasant meetings and discussions, and for his assistance as paranimf.

I would like to thank Anouk Jansen for the improvement of the English language in this thesis.

Furthermore, I would like to thank my family and friends. Especially, my parents who supported me in every possible way and have always been there for me, literally (e.g. during all my stays after the UT visits) and figuratively. Last, but not least: I would like to thank my girl-friend Eva Kloosterboer for her love, care, support and patience.

Contents

Nomenclature

Roman symbols

a_x	semi axis of contact ellipse in x direction	[m]
a_y	semi axis of contact ellipse in y direction	[m]
a'_x	dimensionless semi axis of contact ellipse in x direction	[-]
a'_y	dimensionless semi axis of contact ellipse in y direction	[-]
A	area	[m^2]
A_{MRA}	measured roughness area	[m^2]
A_{Hertz}	Hertzian contact area	[m^2]
b	half Hertzian contact width	[m]
c_p	specific heat at constant pressure	[J kg^{-1} K^{-1}]
d_d	distance between mean plane of summit heights and mean plane of surface heights	[m]
E_i	Young's or elasticity modulus of body i	[Pa]
E'	reduced Young's or elasticity modulus	[Pa]
E	complete elliptic integral of the second kind	[-]
F	normal force	[N]
F^*	adapted normal force parameter	
F_f	friction force	[N]
h	separation	[m]
H	universal hardness	[Pa]
k	specific wear rate	[mm^3 N^{-1} m^{-1}]
k	parameter indicating initial yielding	[-]
K	thermal conductivity	[W m^{-1} K^{-1}]
K_{eff}	effective thermal conductivity	[W m^{-1} K^{-1}]
K	complete elliptic integral of the first kind	[-]
ℓ	contact length	[m]
L	lubrication number	[-]
m	elliptic integral parameter	[-]
p	pressure	[Pa]
p_{av}	average Hertzian pressure	[Pa]
p_h	maximum Hertzian pressure	[Pa]
Pe	Péclet number	[-]
P_f	friction power	[W]
P_{fi}	friction power intensity	[W m^{-2}]

P_{tfi}	true friction power intensity	[W m^{-2}]
Q	frictional heat per unit time	[W]
q	parameter in calculation of $\overline{\theta}_h^{kl}$	[-]
r	coefficient of determination	[-]
r_x	interferometry pixel size in x direction	[m]
r_y	interferometry pixel size in y direction	[m]
R_a	CLA surface roughness	[m]
R_r	running radius	[m]
R'	reduced radius of curvature	[m]
$R_{x,i}$	radius of curvature in x direction of body i	[m]
$R_{y,i}$	radius of curvature in y direction of body i	[m]
s	sliding distance	[m]
s_i	height of summit i	[m]
S	shape factor	[-]
t	time	[s]
T	torque	[N m]
V_w	wear volume	[m^3]
v	sliding velocity	[m s^{-1}]
v^*	adapted sliding velocity parameter	
v^+	sum velocity	[m s^{-1}]
w	load per unit length	[N m^{-1}]
$z_{x,y}$	summit height at coordinate (x,y)	[m]

Greek symbols

α	derivative of pressure with regard to approach at ω_e	[Pa m^{-1}]
$\beta_{x,i}$	summit radius in x direction	[m]
$\beta_{y,i}$	summit radius in y direction	[m]
β'	reduced summit radius	[m]
β	mean summit radius	[m]
β_m	alternative mean summit radius	[m]
γ	dimensionless approach parameter	[-]
η	density of asperities	[m^{-2}]
η_0	dynamic viscosity at ambient pressure	[Pa s]
κ	axis ratio of contact ellipse	[-]
κ_{th}	thermal diffusivity	[m^2 s^{-1}]
λ	ellipse ratio	[-]
Λ	oil film thickness over roughness	[-]
μ	coefficient of friction	[-]
ν	Poisson's ratio	[-]
ν_k	kinematic viscosity	[mm^2 s^{-1}]
ω	approach	[m]
ρ	summit curvature	[m^{-1}]

ρ_d	density	[kg m^{-3}]
σ	standard deviation of roughness height distribution	[m]
σ_s	standard deviation of summit height distribution	[m]
θ	temperature	[ºC]
ξ	radius ratio	[-]

Sub-, superscripts

1, 2	surface 1, 2
a	average
c, C	contact
cr	critical
e	elastic
ep	elastic-plastic
f	flash
f	friction
h	high velocity
i	friction intensity
max	maximum
mean	mean
l	low velocity
p	plastic
s	surface
x	*x* direction
y	*y* direction

Abbreviations

BL	Boundary lubrication
EHL	Elastohydrodynamic lubrication
HL	Hydrodynamic lubrication
ML	Mixed lubrication
RT	Room temperature

Chapter 1

Introduction

1.1 TRIBOLOGICAL CONTACTS

Tribology deals with contacting surfaces under relative motion. Due to friction in these contacts, wear may take place, and lubrication is considered to be an effective way to reduce friction and/or wear. Examples of applications in which tribology plays an important role include gears, cam and follower mechanisms, traction systems, brakes, bearings, cutting tools and clutches.

In Figure 1.1 a schematic representation of the tribosystem is presented. It is composed of two bodies in contact (1 and 2), with a lubricant (3) in between and operating in a certain environment (4).

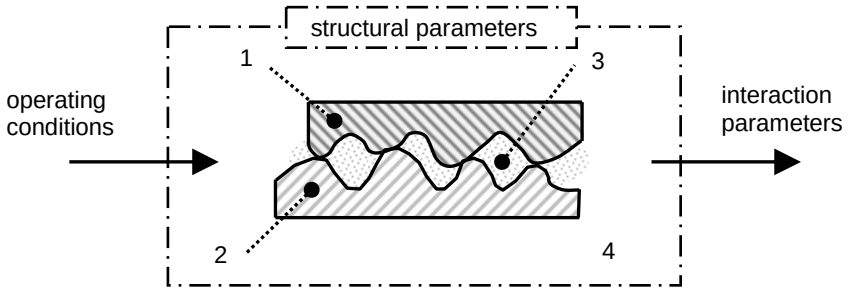

Figure 1.1 Schematic representation of a tribosystem.

Nowadays, engineering components are subjected to more and more extreme operating conditions due to economical and technological trends. In a tribosystem, these operating conditions play an important role and they include:

- Normal force F
- Sliding velocity v or sum velocity v^+
- Type of motion
- Contact time t or sliding distance s
- Temperature θ

These conditions strongly interact with the structural parameters of the tribosystem. These structural parameters are properties related to mechanical and thermal behaviour of the materials in the tribosystem and include:

- Composition and microstructure
- Roughness
- Elastic modulus
- Hardness
- Reactivity of the surfaces

Due to given operating conditions and structural parameters, the tribosystem leads to the following interaction parameters:

- Contact stress/deformation
- Friction
- Heat generation
- Wear

In order to focus further on the characteristics of a tribosystem, a few types of tribological contacts can be distinguished based on the shape of the contacting bodies: conformal, counterformal and flat-flat contacts. Together with a certain specific geometry of the bodies e.g. cylinder or sphere, these contacts result in line, circular or elliptical contacts. Furthermore, the type of motion is important, e.g. rolling or sliding motion; continuous or reciprocating motion. In this thesis only lubricated concentrated contacts are considered.

1.2 FRICTION AND LUBRICATION REGIMES

When two bodies are in contact, they may deform. By using the theory of Hertz [36], the resulting contact pressure, contact area and deformation can be calculated under the assumptions that the bodies deform elastically and that the total deformation is small compared to the overall geometry of the contacting bodies. Hertz also assumed that the bodies are continuous elastic half-spaces and frictionless.

Furthermore, the bodies were supposed to be smooth in Hertz' theory. In reality, however, surfaces are not smooth and the applied production process creates a certain roughness. Contact between rough surfaces takes place at the contacting asperities and hence the real contact area is much smaller than the nominal or apparent contact area as given by Hertz. This situation is shown in Figure 1.2.

Friction between surfaces under relative motion can be characterised by the coefficient of friction μ and is defined by

$$\mu = \frac{F_f}{F}, \tag{1.1}$$

where F_f is the friction force and F is the normal force.

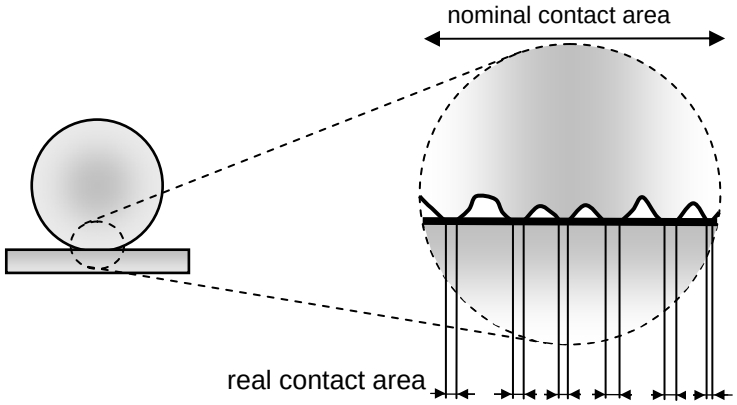

Figure 1.2 Nominal vs. real contact area.

Up to now the surfaces were assumed to be unlubricated, but in order to reduce friction and wear, very often a lubricant is present in the tribological contact. Friction in a lubricated contact is often characterised by the Stribeck curve [25][50], where the coefficient of friction μ is plotted against the sum velocity v^+ or a lubrication number L, which is defined by Schipper [50] as

$$L = \frac{\eta_0 \cdot v^+}{p_{av} \cdot R_a}, \tag{1.2}$$

with η_0 the dynamic inlet viscosity at ambient pressure, p_{av} is the average Hertzian nominal contact pressure (see Chapter 3) and R_a is the combined CLA roughness of the two surfaces and v^+ the effective sum velocity, in general given by (see [34])

$$v^+ = v_1 + v_2, \tag{1.3}$$

where v_1 and v_2 are the velocities of respectively body 1 and body 2 relative to the force vector. For a simple sliding contact, $v_1 = v$ and $v_2 = 0$, Eq. (1.2) becomes

$$L = \frac{\eta_0 \cdot v}{p_{av} \cdot R_a} \tag{1.4}$$

A schematic representation of the Stribeck curve is given in Figure 1.3.

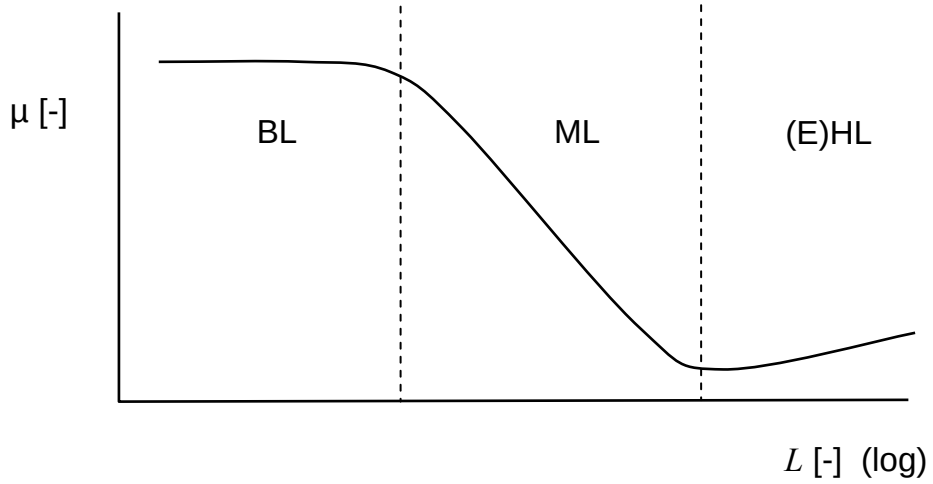

Figure 1.3 Schematic representation of a Stribeck curve.

Depending on the operating conditions three lubrication regimes can be distinguished:

1. (Elasto)hydrodynamic lubrication or full film lubrication: The applied load is entirely carried by the lubricant, as shown in Figure 1.4c. Depending on the pressure generated in the lubricant and elasticity of the contacting bodies, hydrodynamic or elastohydrodynamic lubrication may occur. For high pressure elastohydrodynamic lubrication (EHL) is present, where the geometry of the contacting bodies elastically deforms. And for low pressure hydrodynamic lubrication (HL) is present, where the elastic deformation of the bodies can be neglected. The coefficient of friction is determined by the shear strength of the lubricant, which is mainly dependent of the lubricant viscosity and existing shear rate.
2. Boundary lubrication (BL): The applied load is entirely carried by the interacting asperities separated by boundary layers, as shown in Figure 1.4a. The coefficient of friction is determined by the shear strength of the boundary layers.
3. Mixed lubrication (ML): This is the intermediate regime between the (E)HL and BL regimes, where the applied load is partly carried by the lubricant and partly by the asperities.

a. boundary lubrication b. mixed lubrication c. (elasto)hydrodynamic lubrication

Figure 1.4 Lubrication regimes

1.3 WEAR AND WEAR MECHANISMS

1.3.1 Wear

Wear can be defined as the surface damage or loss of material of one or both two solid surfaces in relative motion. In general, wear occurs through surface interactions at asperity level. Material on the contacting surface may be damaged and displaced, so that properties of the solid body, at least at or near the surface, are altered, but little or no material is actually lost. Furthermore, material may be removed from the surface and may result in the transfer to the mating surface or may break loose as a wear particle. In the case of transfer from one surface to another, net volume or mass loss of the interface is zero, although one of the surfaces is worn (with a net volume or mass loss). Wear damage precedes actual loss of material, and it may also occur independently.

Wear can be characterised in several quantitative ways. These include:

- wear volume V_w of the component(s)
- specific wear rate k and is defined by:

$$k = \frac{V_w}{Fs} \tag{1.5}$$

- wear coefficient K is defined by Archard's law according to:

$$K = kH = \frac{V_w H}{Fs}, \tag{1.6}$$

  where V_w is the wear volume, H the hardness, F the normal force and s represents the sliding distance.
- wear depth of the component(s)
- change of various roughness parameters

Definition of wear is generally based on loss of material, but it should be emphasised that damage due to material displacement on a given body, with no net change in weight or volume, also constitutes wear [6].

1.3.2 Wear Mechanisms

In general, it is possible to distinguish several mechanisms that lead to wear of an engineering component. These wear mechanisms are [18]

1. (tribo)chemical
2. abrasive wear
3. fatigue
4. adhesive wear

Whether a contact is lubricated or not is very important. In literature, a lot of attention is paid to unlubricated (dry) contacts in relation to wear. In lubricated contacts, lubrication regimes according to the Stribeck curve (see Figure 1.3 and Figure 1.4) have to be taken into account.

In full film lubrication and then particularly in EHL, the only possible wear mechanism is fatigue. In BL and ML (part of) the load is carried by asperities. The asperities make contact but there is no metal-metal contact due to surface films attached to the surface. Now, shearing takes place in those surface films. If the hardness of both materials is of the same order of magnitude, thus excluding abrasive wear, mild tribochemical wear may take place. Under extreme operating conditions boundary layers will not hold and metal-metal contact occurs and this may cause adhesive wear.

In the next four sections, the wear mechanisms are explained in more detail. In the last section attention is paid to running-in.

1.3.2.1 (Tribo)Chemical Wear

Under conditions of boundary lubrication (and partly mixed lubrication) asperities come in close proximity, and the lubricant viscosity is relatively unimportant. The physical and chemical interactions of (additives in) the lubricant with the solid surfaces, control friction and wear.

Surface film formation occurs according to three mechanisms, listed in order of increasing film bonding strength, Godfrey [26]:

- physical adsorption
- chemical adsorption
- chemical reaction

Friction may change the kinetics of the chemical behaviour and the surface films may be removed. The base material will react again to form surface films trying to protect the interacting asperities and these films will again be removed by asperity contacts. Although shear occurs in the surface films, chemical reactions change the surface and mild wear will take place. The most obvious mechanism by which friction increases the rate of chemical reaction is frictional heat produced at contacting asperities. Tribochemical wear is the mildest form of wear. If the material removal is purely tribochemical, no microfracture or plastic deformation takes place, Bhushan [6].

1.3.2.2 Abrasive Wear

Abrasive wear occurs when asperities of a rough hard surface or hard particles slide against a softer surface and damage the interface by plastic deformation or fracture. The general rule of thumb is that if one surface is more than 20% harder than the other, asperities of the harder surface will plough through the softer surface ($H_1 > 1.2\ H_2$), Landheer and de Gee [42]. This type of abrasive wear is called two body abrasion. Another type of two body abrasion occurs, if for example work hardened debris is embedded in the soft surface which hence leads to hard asperities. Three

body abrasive wear may occur if these particles (third body) are able to move in the contact area and are not embedded in a fixed position.

1.3.2.3 Fatigue

Surface fatigue takes place due to repeated loading. The repeated loading and unloading cycles lead to the formation of (sub)surface cracks. After an incubation period and a critical number of cycles the formation of large fragments will occur. These lead to large pits in the surface and this is often called pitting. During the incubation period negligible wear takes place. Hence fatigue is different from the other wear mechanisms where a gradual deterioration of the surface is observed.

1.3.2.4 Adhesive Wear

If the adhesion forces in a sliding contact are high, shear takes place in the weakest material instead of at the surface interface. This may result in detachment of fragments of one surface and attachment to the other surface. At continued sliding, material will be transferred across the contact.

When the initial condition is boundary lubrication (only tribochemical wear), a transition to adhesive wear may take place. Under conditions of increased contact severity, protective surface layers will not withstand, and metal-metal contact will occur. First (at e.g. increasing normal force and/or sliding velocity) mild material transfer will take place at a microscopic scale. This condition is called incipient or micro scuffing. At even more serious conditions, severe adhesive wear will occur. This condition is commonly referred to as scuffing.

1.3.2.5 Running-in

Another important phenomenon is running-in. Running-in results in a decrease of roughness as a function of time or running distance (see Figure 1.5) and is often considered as beneficial during machine life. During the first stage (A) plastic deformation as a result of normal stresses occurs at the highest roughness summits and this will result in a fast decreasing roughness. Strictly speaking this cannot be called wear because this decrease in roughness only originates from normal forces/stresses.

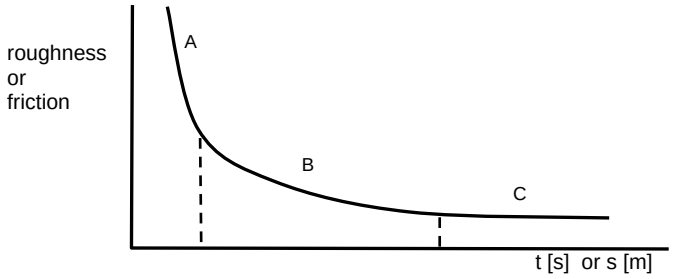

Figure 1.5 Schematic representation of roughness and friction as a function of time *t* or sliding distance *s* during running-in.

During the next stage (B) tribochemical wear at surface asperities as a result of lubricated friction occurs at a slower decreasing roughness value and this will gradually transfer into the last stage (C) which constitutes a stable situation of process roughness.

Besides this it is possible to distinguish two levels of severity in running-in (and wear in general):

1. Micro wear: contact pressure does not change in time (p_{av} is constant) and the roughness decreases. The area that is worn off equals more or less the Hertzian contact area.
2. Macro wear: contact area increases and therefore the contact pressure decreases (p_{av} is not constant).

1.4 WEAR TRANSITIONS IN TRIBOLOGICAL CONTACTS

The Stribeck curve usually maps (lubrication) regimes by means of the coefficient of friction as a function of operating conditions under mild wear conditions (as stated in Section 1.2).

To map transitions in wear mechanisms or failure modes as a function of operating conditions another diagram is needed. In literature these are known as transition diagrams, wear (mechanism) maps or failure diagrams. For example the thermomechanical wear diagrams by Lim and Ashby [43][44], the F-v-θ transition diagrams as described by Czichos [15][16][17], PV-diagrams by Bhushan [6], IRG transition diagrams by de Gee/Begelinger [3][4][23] and the mild-severe wear map for ceramics by Pasaribu [48].

Failure modes in tribological contacts are depending on both operational parameters and structural parameters. Examples of failure modes are:

- Pitting, a form of (sub)surface fatigue as experienced in highly loaded machine components e.g. gears and roller bearings, see [12].
- Severe thermomechanical wear due to plastic surface deformation in (un)lubricated contacts, see [13][43] [57].
- Severe wear in unlubricated ceramics, see [47].
- Scuffing, which is initiated by the transition from a mild to an *adhesive* wear region in lubricated contacts (this thesis).

1.5 THESIS OBJECTIVE

This thesis focusses on the transition from mild to adhesive wear of lubricated contacts. This transition can lead to scuffing and hence catastrophic failure of machine compenents. Due to this failure, replacement of damaged machine components is often necessary. Therefore, the transition to adhesive wear as a function of the complex interaction of operational and structural parameters has to be mapped in order to be able to optimise the tribosystem with regard to scuffing resistance.

In order to lower the high costs involved with identifying and verifying the most important parameters with regard to scuffing resistance by means of measurements, a mathematical model has to be developed which can predict the transition from mild to adhesive wear of lubricated systems.

1.6 OUTLINE OF THIS THESIS

In Chapter 2 a literature review is given on the transition from mild to adhesive wear and the failure mode of scuffing. In Chapter 3 an elastic/plastic deformation model of an anisotropic deterministic rough contact is developed. In Chapter 4 the development of a model that predicts the contact temperature is discussed. In Chapter 5 the deformation and temperature model are incorporated in a model that predicts the transition to adhesive wear. Chapter 6 describes the design of a pin-on-disk type tribotester that is capable of accurately measuring the adhesive wear transition for a cylinder against a disk. Furthermore, a pin-on-disk tribotester which is capable of testing at high temperatures is discussed. In Chapter 7 the experimental results are presented. These results are used to validate the mild-adhesive wear transition model. Finally, Chapter 8 summarises the results and gives the final conclusions together with some recommendations for further research.

Chapter 2

Transition from Mild to Adhesive Wear

2.1 INTRODUCTION

As outlined in Chapter 1, scuffing is the catastrophic failure of lubricated machine components and is initiated by a transition from mild to adhesive wear. Due to metal-metal adhesion, the surface will be severely damaged and material will be transferred from one body to the other. The physical manifestations during scuffing are a sudden increased friction and wear level, accompanied by noise and vibration.

First, diagrams based on measurements reported in literature will be presented which characterise this transition as a function of several operational parameters. Next, from these measurement based observations and additional theoretical studies, conclusions are drawn by several researchers with regard to possible failure mechanisms and failure criteria.

2.2 WEAR TRANSITION DIAGRAMS

2.2.1 Introduction

The transitions in dominant wear mechanisms occur when loads and sliding velocities are changed. In some cases, changes also occur as a function of sliding time or distance. The dominant wear mechanisms are based on mechanical strength and interfacial adhesion. Increase in both normal load and sliding velocity results in a monotonic increase in contact temperature. High interface temperature results in formation or breakdown of surface protecting films at the contact interface. Furthermore, high temperatures may result in a decrease in mechanical strength and in some cases structural changes occur. At very high temperatures very severe adhesive wear will take place (more details are given in Section 2.3).

2.2.2 The IRG Transition Diagram

Diagrams that cover the transition from mild to adhesive wear of lubricated concentrated contacts include the IRG transition diagram (see below) and the F-v-θ diagram by Czichos [16] (note: Czichos uses T instead of θ for the temperature). The wear transition is mapped as a function of a set of operational parameters. The IRG transition diagram distinguishes between regions of efficient and inefficient performance in non-conforming lubricated sliding contacts, see [3][4][23][52]. This diagram is commonly used and representative for other operational parameter based transition or failure diagrams. The failure criterion used is based on the change of friction level. For a contact situation in a machine element or test rig, this is a very useful criterion for in-situ detection.

An example of an IRG transition diagram for point contacts is schematically shown in Figure 2.1, reproduced from de Gee [24]. In this diagram, where the load-carrying capacity F is presented as a function of the sliding velocity v, three regions, separated by two transition curves, can be distinguished. These regions are governed by the measured friction-time characteristics according to Figure 2.2. The recorded friction signal is usually less than 5 minutes.

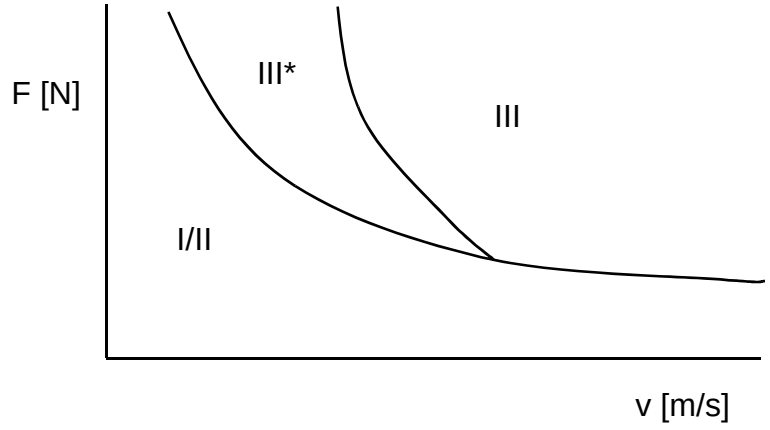

Figure 2.1 IRG transition diagram [24].

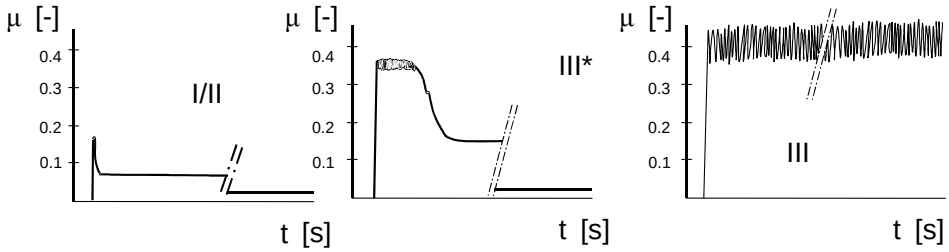

Figure 2.2 Friction coefficient-time curves [24].

Region I/II is considered to be a 'safe' region, where friction is relatively low (Stribeck curve values; roughly: $\mu = 0.15$ or less) and wear is virtually negligible (wear rate $k \approx 10^{-8}$ $mm^3N^{-1}m^{-1}$). The lubricating conditions in this region are BL, ML and EHL. If the contact operates in region III, it fails immediately by scuffing, with $\mu \approx 0.5$ and $k \approx 10^{-3}$ $mm^3N^{-1}m^{-1}$. In this region very severe adhesive wear (material transfer) will take place [51].

In the intermediate region III* there is incipient or micro scuffing i.e. adhesive wear and material transfer takes place at a microscopic scale, and the average contact pressure decreases. Initial values of $\mu \approx 0.35$ and $k \approx 5 \cdot 10^{-6}$ $mm^3N^{-1}m^{-1}$ occur in this region, both decreasing with time. From a practical point of view this region should be avoided for machine components. Although the contact restores from adhesive to mild wear, the macro geometry is lost. Therefore, the transition from I/II to III*/III is the interesting one to predict.

2.2.3 Determination of Transitions – Test Procedures

In order to obtain the transition diagram, a set of experiments has been carried out. At each experiment the friction-time characteristic is measured at a certain combination of F and v. Based on this characteristic it can be determined whether this contact situation belongs to region I/II, III* or III (see Figure 2.1 and Figure 2.2).

A few different test procedures are possible depending on the initial state of a specimen at each experiment and are described in detail by Schipper et al. [52]. The first procedure (A) uses new, virginal specimens for each experiment, i.e. the test is performed at a certain load and velocity. Consequently, the order of each experiment does not matter. This procedure is the traditional IRG method.

A second procedure (B) uses the same specimens at a certain velocity but uses several increasing load steps. As a result, there is a stepwise growth of the developing contact area during each load step. This influences the location of the transitions significantly (see Figure 2.3). The transitions shift to higher values for F. In other words, when using this loading procedure, the load carrying capacity increases. Worth noting is that the friction time characteristics for region III* and III are also different, whereas the region I/II stays the same. In regions III* and III the friction time characteristic starts with an incubation period, during which the μ value is equal to the one measured during the previous step. This is followed by a sharp increase in friction values, virtually equal to those found in procedure A.

An explanation for the occurrence of the incubation period or dwell time is given by Begelinger and de Gee [4]: it is possibly associated with the presence of surface films (boundary layers), formed during running-in. Such films modify the heat transfer characteristics of the surfaces, thus delaying the establishment of thermal steady state in the contact zone.

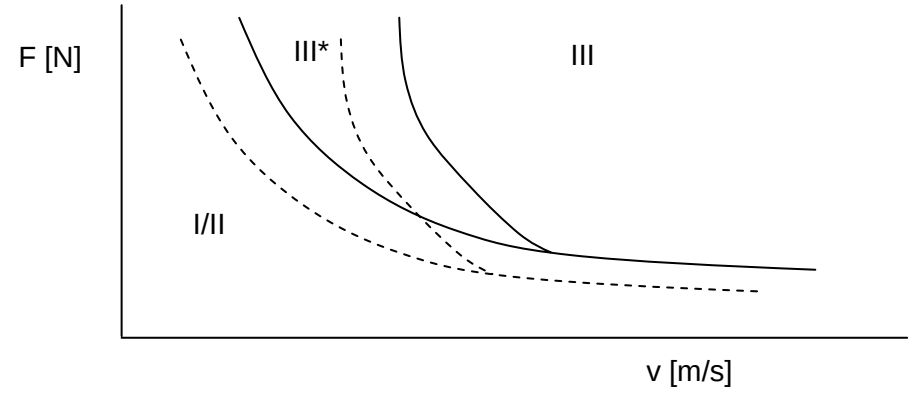

Figure 2.3 Transition diagram determined in case of procedure B (drawn line) compared with procedure A (dotted line) [52].

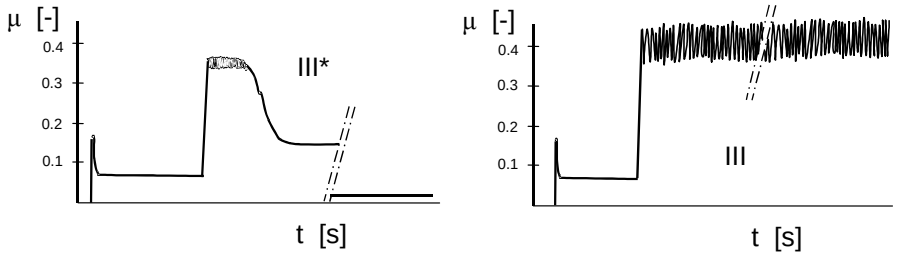

Figure 2.4 Friction-time characteristics for region III* and III for procedure B [52].

A third procedure (C) uses the same specimens at a certain load but uses several increasing velocity steps. Now the contact area does not grow during the experiment (the load does not change). When starting a test in which procedure A regime I/II conditions apply, at increasing v the specimens remain running in regime I/II until regime III* or III occurs (see the transition in Figure 2.5). Furthermore, the friction time characteristics of procedure C are comparable with those of procedure B.

Performing subsequent tests (B and C) with the same specimens, instead of with new specimens, leads to a substantial shift of the transitions. Under the assumption that performing in regime III* (and III of course) is not allowed, procedure B can be used to increase the load carrying capacity, which is defined as the transition value for the load at a certain velocity. In other words, the maximum load that is allowed at a certain velocity.

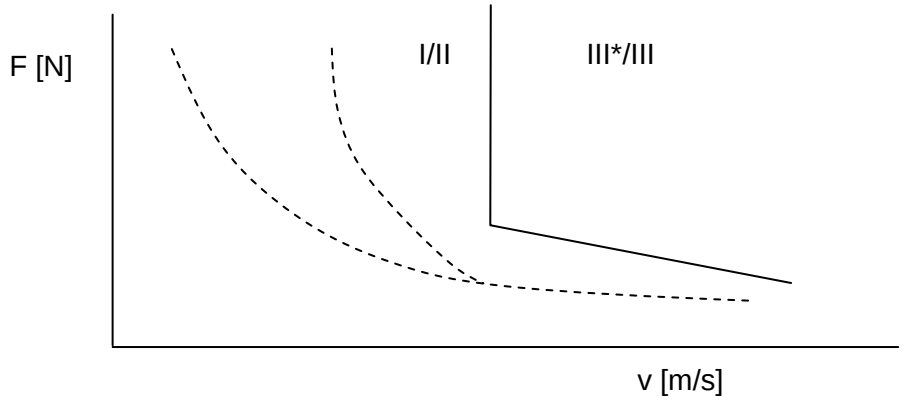

Figure 2.5 Transition diagram determined in case of procedure C (drawn line) compared with procedure A (dotted line) [52].

2.3 FAILURE MECHANISMS

In order to explain why the transitions take place, why a contact fails due to scuffing and to find the failure mechanism accordingly, a closer look at the tribosystem from Figure 1.1 is necessary. With regard to the contact situation in a lubricated sliding contact, three levels of protection against scuffing can be distinguished, i.e.

1. (E)HL films
2. Surface films
3. Material strength

2.3.1 (E)HL Films

The (elasto)hydrodynamic action, as described in Section 1.2, completely separates the two moving surfaces and obviously prevents the contact from scuffing. The separation is often characterised by the Λ-ratio, defined as the oil film thickness over roughness [25]. Several researchers have been investigating the relation of the breakdown of the EHL film with the onset of scuffing, see for instance Dyson [19]. In this work of Dyson, a model is proposed where the Λ-ratio needs to reach a certain critical value for scuffing to take place. However, this relationship could not be found. Ku et al. [40] stated that the basic objection against this model is that it is just a physical proposition, which does not account for the known oil-metal-surface treatment-environmental effects on scuffing.

When under more harsh conditions asperities are capable to penetrate the (E)HL film, scuffing/adhesive wear may occur in absence of surface films. However, with the presence of additives in lubricants and the formation of oxide films, the breakdown of an (E)HL film is just a necessary condition for the occurrence of scuffing, but not a sufficient condition for scuffing to actually happen.

Furthermore, a lot of contacts in machines operate under conditions of BL or ML, without the surfaces being fully separated by an (E)HL film and without adhesive wear/scuffing taking place. These lubrication regimes can be added to the IRG transition diagram according to Schipper [51] and is presented in Figure 2.6. In this figure, region I is represented by the (E)HL regime, region II by the BL regime and in between the ML regime can be found (see Figure 1.3). It can be seen that the transition often takes place from a BL or a ML region. In addition to Schipper, Horng [38] also presented measurements in which scuffing occurred from an initial ML condition. The contacts operating in ML and BL are protected by the next line in defense against scuffing: the surface films.

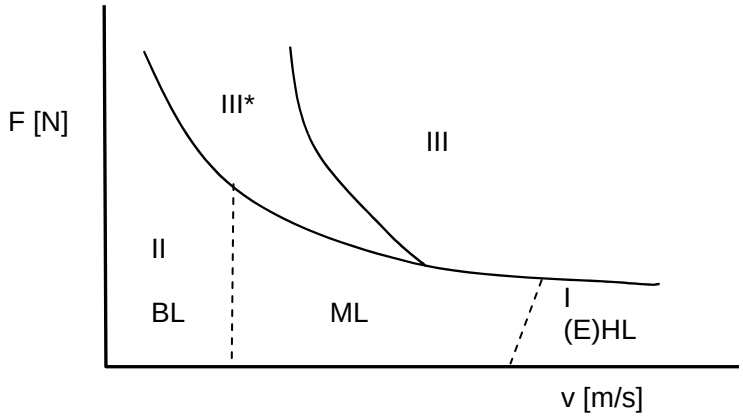

Figure 2.6 Schematic representation of the IRG transition diagram combined with the Stribeck curve.

2.3.2 Surface Films

Surface protecting films include films of adsorbed lubricant molecules and oxide films. Surface film breakdown is researched by several investigators, in relation to temperature. Spikes and Cameron [53] show the occurrence of film breakdown when the rate of adsorbed layers reaches a critical level in relation to the increasing rate of desorption at higher temperatures.

Cutiongco and Chung [14] demonstrated the influence of the competitive kinetics of oxide formation and removal with temperature, in relation with the occurrence of scuffing. A diagram is constructed with the Arrhenius plots of oxide formation and removal rates and the critical failure temperature is assigned to the intersection of these plots, as shown in Figure 2.7. Bjerk [7] conducted measurements on a gear-roller test machine using plain mineral oil lubrication. He showed the surface protection against scuffing by the formation of oxides in the contact.

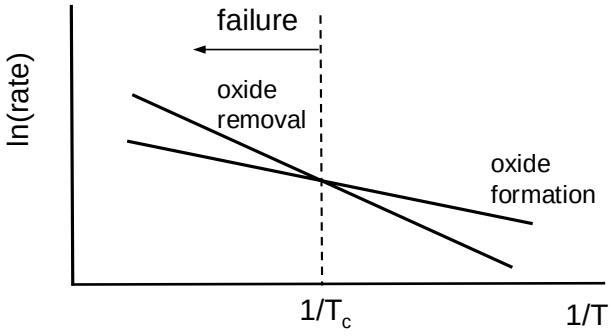

Figure 2.7 Schematic diagram showing the variation of oxide formation and removal rates as a function of the temperature. Failure occurs when the oxide removal rate is greater than the oxide formation rate [14].

When the surface films are broken through, the next line in defence of scuffing appears: the material strength. This is presented in the next section.

2.3.3 Material Strength

During sliding, shear between two bodies takes place at the interface or in the subsurface of the weaker of the two bodies. When the protecting (E)HL and surface films are absent or broken down and the interfacial adhesion strength is high compared to the shear strength of the subsurface regions, shear may occur and small fragments may become attached to the other surface. In the previous section this is addressed towards adhesive wear on the micro scale. When asperities start to heat up even more due to scuffing on the micro scale, surface temperatures increase even further. This has a large effect on the temperature dependent material strength and can lead to large scale and very severe wear.

Yu et al. [58] report the effects of thermal softening of asperity contacts. This reduction of mechanical strength due to temperature dependent yield strength will cause the asperities to plastically deform and this will lead to scuffing. This corresponds to the transition from III* to III as described in Section 2.2. Cowan et al. [13], Yang et al. [57] and Wang et al. [55] also ascribe the occurrence of scuffing to exceeding the material yield stress by thermomechanical loading. Zhang et al. [59] state, that after the loss of all protective layers, scuffing would occur when the maximum tangential traction is larger than the modified shear strength. Hershberger et al. [35] attribute the moment of scuffing initiation to adiabatic shear instability (unstable plastic deformation) at asperity level when increasing thermomechanical contact severity causes the rate of thermal softening to exceed the rate of work hardening.

2.3.4 Conclusion

The following timeline of events in relation to the loss of surface layers and exceeding the material critical strength can be constructed with regard to the IRG transition diagram (see Section 2.2.2):

1. The increase in contact severity (i.e. increase in F and/or v) and hence the production of more frictional heat Q ($= \mu Fv$) is accompanied by an increase in surface temperature, especially at the asperity contacts.
2. If the contact reaches a certain critical temperature, the surface films will break down, as suggested by Blok [10]. First, breakthrough is mainly to be expected at the highly pressurised asperity contacts. A number of asperities is now unprotected, and metal-to-metal contact occurs. Together with strong adhesion and relatively low cohesion/material subsurface strength, this will lead to plastic deformation of these asperities, and this process is accompanied by a sharp increase in friction, up to μ values of 0.35 and 0.4, respectively for transitions to III* and III (see Figure 2.3). Now, there are two possibilities for the continuation of this event.
   A. The first is that the coefficient of friction stays a while at the $\mu = 0.35$ level and then comes down to common Stribeck values (0.15 or less, depending on L). This "healing" effect can be attributed to the lowering of the overall contact pressure due to wear. This process is called incipient scuffing or micro scuffing (III*). According to tests performed by de Gee et al. [22] oxygen content also plays an important role in relation to the dwell time at $\mu = 0.35$. More oxygen leads to smaller dwell times, no oxygen at all leads to a continued stay at high friction levels.
   B. The second possibility of continuation is that the coefficient of friction μ goes directly to higher unstable values for μ of around 0.5. No healing occurs, and severe adhesive wear takes place. Apparently, the loss of surface layers in combination with much higher heat development leads directly to exceeding the material critical strength.

In conclusion, it can be stated that the transition from I/II to III* can be attributed to the breakthrough of surface layers. The transition from III* to III needs, besides a breakthrough of surface layers, some extra severity to come to the next critical level: exceeding the material strength. The transition from I/II directly to III is a limit situation where directly after the breakthrough of the surface layers, enough heat is generated to exceed the material strength as well. Due to the high velocity there is not enough time for the healing effect to take place. Alternatively, it can be stated that region III* is very small here. Therefore, Figure 2.8 gives a better representation of the mechanisms involved, although verification through measurement is difficult.

Furthermore, it must be stressed that the transition from III* to III is not of practical interest. In region III* already too much damage is accumulated in machine elements which prevents further smooth operation. Hence, the transition from I/II to III* (or III) must be examined with regard to scuffing prevention in machine design.

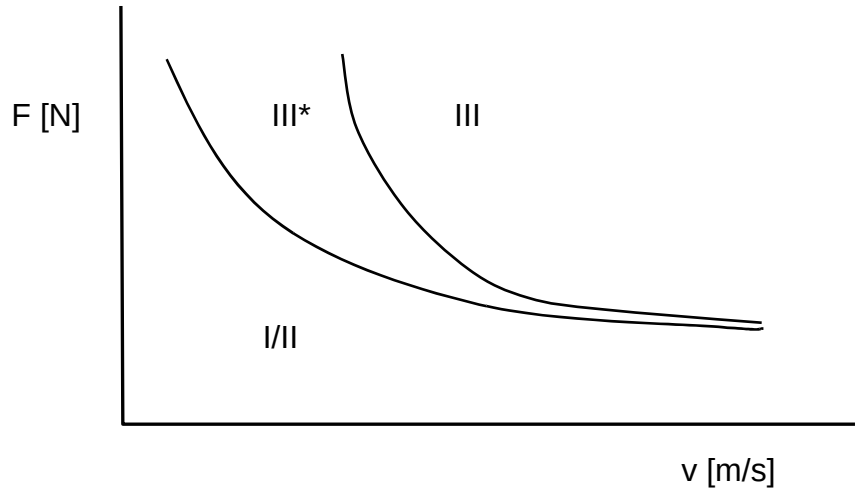

Figure 2.8 Schematic transition diagram.

2.4 FAILURE CRITERIA

In literature, criteria to describe the transition from mild to adhesive wear are either based on a set of critical parameters taken from measurements, in which certain operational variables are varied or based on a certain, more fundamental, hypothesised mechanism and are then often accompanied by calculations.

The friction power P_f is defined as the generated frictional heat per unit time Q, according to

$$P_f = Q = \mu F v \,. \tag{2.1}$$

Meng [46] suggested a friction power (FP) criterion which implies that scuffing occurs when the friction power P_f of the sliding contact reaches a critical value.

Matveevsky [45] proposed a friction power intensity (FPI) criterion based on scuffing measurements of lubricated point and line contacts. The friction power intensity P_{fi} is defined as the friction power divided by the Hertzian nominal contact area A_{Hertz}

$$P_{fi} = \frac{\mu F v}{A_{Hertz}} = \mu p_{av} v \,. \tag{2.2}$$

Bell et al. [5] showed that this criterion fitted their sliding/rolling measurements on a two disk machine rather well. However, for measurements carried out by Horng [37] for lubricated line contacts on a pin-on-disk configuration, the friction power intensity criterion did not predict the occurrence of scuffing very well.

Furthermore, from the viewpoint that the breakdown of layers originates from micro contact heating, Horng decided to take into account the true contact area A_t instead of the nominal Hertzian area and suggested a true friction power intensity (TFPI) criterion accordingly. The friction power intensity P_{tfi} is given by

$$P_{tfi} = \frac{\mu F v}{A_{Hertz}} \cdot \frac{A_{Hertz}}{A_t} = \frac{\mu F v}{A_t} . \tag{2.3}$$

The TFPI criterion improved the scuffing prediction for Horng's experiments, but still, scuffing could not be characterised by a single P_{tfi} value. Therefore, a fit has been constructed, taking into account additional effects of relative velocity v and surface roughness (combined RMS value: σ), which gave a constant value for Horng's measurements, according to

$$P_{tfi} \cdot v^{-1.2} \cdot \sigma^{-0.6} = C , \tag{2.4}$$

where $C = 1.5 \cdot 10^8$. Horng stressed that C is still dependent on a combination of lubricant, materials, and other variables.

Czichos [16] carried out four-ball tests and constructed an F-v-θ failure surface, which is similar to the IRG transition diagram with inlet temperature θ_j as an additional parameter and in which scuffing is attributed to lubricant failure. Based on these measurements a failure formula is fitted in the form

$$F^a \cdot v^b \cdot t^c \cdot \theta_j = const . \tag{2.5}$$

Fits have been made with regard to a, b, c and $const$, based on reported own measurements and other results of four ball systems from literature. Unfortunately, different fit parameters are necessary for the measurement results from literature; for identical four ball systems as well as for other configurations like pin-on-ring.

Begelinger and de Gee [3] conducted tests on a ball-on-ring tribometer and suggested a so-called collapse parameter C_{col}, given by

$$C_{col} = v^{1/6} p_{av} . \tag{2.6}$$

These authors state that the collapse parameter is constant for a particular system, but with different constants for different systems, e.g. lower roughness specimens gave higher values for the constant. Furthermore, the collapse (scuffing) is associated with desorption of adsorped boundary layers.

Already in the 1930s, Blok [10] presented a more fundamental approach to the onset of scuffing with the presentation of the critical temperature hypothesis. In this hypothesis Blok postulated that scuffing will occur when the maximum surface temperature in the contact reaches a critical constant value ($\theta_c = \theta_{cr}$). The total surface temperature rise θ_c in a contact consists of a quasi-steady surface

temperature θ_s and an instantaneous surface temperature rise i.e. the flash temperature θ_f according to

$$\theta_c = \theta_s + \theta_f \,. \tag{2.7}$$

According to Blok's hypothesis, the critical temperature θ_{cr} now reads

$$\theta_{cr} = \theta_c = \theta_s + \theta_f \,. \tag{2.8}$$

Furthermore, Blok [9] developed a model for the flash temperature θ_f, given by

$$\theta_f = 0.63\mu\left(v_1^{1/2} - v_2^{1/2}\right)\left(\frac{F}{\ell}\right)^{3/4}\left(\frac{E'}{R'}\right)^{1/4}\left(K\rho_{th}c_p\right)^{-1/2} . \tag{2.9}$$

For the quasi-steady surface temperature θ_s, Blok used the term bulk temperature. Ku et al. [41] found the following relation for the quasi-steady surface temperature θ_s

$$\theta_s = C\cdot\left(\mu F v\right)^n + \theta_j \,, \tag{2.10}$$

where θ_j represents the oil inlet temperature; n is a correlation exponent, close to unity and C is a correlation coefficient, which is a function of system design and other variables affecting heat transfer.

Many researchers have tried to link their measurements to Blok's hypothesis. Ku et al. [40] conducted over 500 sliding-rolling scuffing tests. Based on a statistical analysis of the test data it was found that the critical contact temperature may be taken as substantially constant for a given oil-metal-surface treatment combination over a wide range of design and operating variables. Dyson pointed out in the discussion of this paper, however, that for a broader range of slide-to-roll ratios, the critical surface temperature can be significantly different, based on [5].

Czichos [16] showed results of critical temperatures in an F-v-θ diagram (failure surface). For high velocities, the critical temperature is quite constant, but for low velocities it is not. In the discussion of [40] he suggested that the constancy of the critical temperature as defined by Blok is only valid for systems operating under BL conditions, and for systems operating under ML conditions, the macroscopically determined average coefficient underestimates the flash temperature calculation. As most systems operate in the ML regime, a model is needed which takes into account this regime.

2.5 DISCUSSION AND CONCLUSION

The last section showed that there are roughly two classes of failure criteria. The first class is based on the critical scuffing power intensity or its variants. The second class is postulating a critical scuffing temperature of some sort. The first class only takes into account the heat generation and does not pay attention to heat transfer effects. On the contrary, the temperature based criteria do account for heat transfer effects. Therefore, they are assumed to be more realistic.

As outlined in Section 2.3.2, the surface protecting film will be broken through due to high asperity contact temperatures, therefore the basic objection against Blok's temperature model is that the influence of the real area of contact is not covered. Horng already showed much improvement when incorporating the real area of contact instead of the nominal area in his true friction power intensity model (Eq. (2.4)). Unfortunately, in his work this approach was not used in order to improve the critical temperature criterion.

Improvement of results when evaluating Blok's critical temperature criterion is thus to be expected by incorporating asperity contact characteristics in the calculation of the flash temperatures θ_f. Moreover, taking into account the governing lubrication regime, i.e. incorporating the Stribeck curve, is assumed to lead to further enhancement. This approach is used in this work. In Chapter 3 a contact model for lubricated concentrated contacts will be developed in which detailed mechanical information about the asperity contacts can be obtained. Then, in Chapter 4 this contact model will be implemented in a new thermal model. With this model it will be possible to calculate both the individual asperity flash temperatures and the quasi-steady surface temperature as a function of operational variables and structural parameters.

Chapter 3

Elastic/Plastic Deformation of an Anisotropic Deterministic Rough Contact

3.1 INTRODUCTION

In Chapter 2, a literature review is given on comprising factors which influence the transition from mild to adhesive wear. In order to set up a design tool, more parameters than only the normal load F and sliding velocity v have to be taken into consideration. Based on the hypothesis that the transition will take place if the temperature of roughness summit contacts exceeds a certain critical temperature, an analysis of the asperity contact temperature distribution has to be carried out. In order to calculate this temperature distribution, detailed information about the contact situation is needed. Therefore, it is important to understand the way asperities deform under loading.

In this chapter, the implementation of a deterministic description of the roughness into a deformation model is presented. The deformation of the roughness summits can be elastic, plastic or a mixed form: elastic-plastic.

3.2 CONTACT MODEL

Before going into the details of micro contacts, the macro contact can be described as the contact of two elastic surfaces (indicated by index 1 and 2). The elastic behaviour can be characterised by the so-called reduced elastic or Young's modulus E', taking into account the modulus and Poisson's ratio ν of both contacting surfaces. The reduced elastic or Young's modulus E' is given by [39]

$$\frac{1}{E'} = \frac{1}{2}\left(\frac{1-\nu_1^2}{E_1} + \frac{1-\nu_2^2}{E_2}\right). \tag{3.1}$$

A similar approach can be carried out with regard to the geometry of the two contacting surfaces. The reduced radius R' can be defined as a combination of the radii in x and y direction of surface 1 and 2 according to

$$\frac{1}{R'} = \frac{1}{R_x} + \frac{1}{R_y}, \text{ where } \frac{1}{R_x} = \frac{1}{R_{x,1}} + \frac{1}{R_{x,2}} \text{ and } \frac{1}{R_y} = \frac{1}{R_{y,1}} + \frac{1}{R_{y,2}}. \tag{3.2}$$

Several contact models dealing with surface roughness can be found in literature [25][28][29]. Most of them are an extension of the Hertzian theory for smooth surfaces with a statistical description of the surface roughness superimposed. In these statistical contact models the surface is characterised by a few statistical parameters like the mean radius of the asperities β, the number of asperities η and the standard deviation of asperity summit height distribution σ_s.

Detailed information, like contact area, approach and contact force/pressure per summit, is needed for an accurate calculation of the temperature in a micro contact. In order to get a more realistic description of the surface contact situation a deterministic model is needed in which the deformation of all individual roughness summits is covered. Therefore, in this work a deterministic contact model is developed in order to give optimal information about the deformation of individual roughness summits.

For the moment, the contact between one rough surface and a smooth surface will be considered. The contact of the summits of one rough surface against a smooth flat plane will be studied as shown in Figure 3.1. The bodies in contact are assumed to deform elastically, whereas the summits are assumed to deform elastically and plastically as a function of the applied normal force. In this work, the line contact situation of a smooth cylinder against a rough disk will be taken as a reference case.

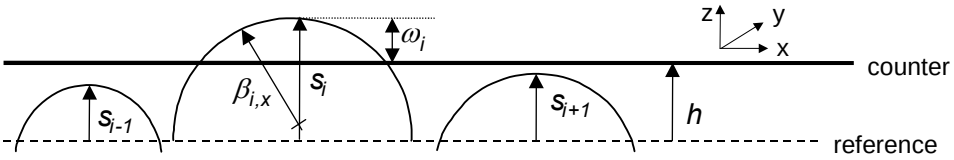

Figure 3.1 Summit contact situation: rough surface against smooth counter body.

Furthermore, many engineering surfaces have strongly anisotropic roughness patterns, e.g. by turning and grinding processes or after running-in. This is reflected in the way the summits are defined, i.e. for anisotropic surfaces the summits are assumed to have different radii in running and tangential direction.

3.3 ROUGHNESS CHARACTERISATION

3.3.1 Introduction

The surface roughness can be characterised by means of an optical phase shift interferometry profiler [49][56]. The outcome of these roughness measurements is a three-dimensional surface height distribution with heights $z = z(x,y)$ at equidistant co-ordinates x and y. In order to get a suitable surface for a plan-parallel contact situation, a reference shape (e.g. cylinder, sphere or quartic) is subtracted from the measured surface to eliminate the overall surface shape. Furthermore, a correction is applied for missing points (interpolation) and spikes (spike removal) [49].

3.3.2 Summit Height Distribution

The interacting surfaces make contact at asperity level and in this case at their summits. A summit is defined as a point with a local surface height higher than its neighbouring points [27]. Different definitions can be used to characterise the surface extremes (see [49]): peaks (I), five-point summits (II) and nine-point summits (III) as shown in Figure 3.2. De Rooij [49] advises to use the nine-point definition because this minimises the probability of detecting 'false summits'. This comes down to

$$z_{x,y} > z_{x-1,y-1}, z_{x-1,y}, z_{x-1,y+1}, z_{x,y-1}, z_{x,y+1}, z_{x+1,y-1}, z_{x+1,y}, z_{x+1,y+1}\,. \tag{3.3}$$

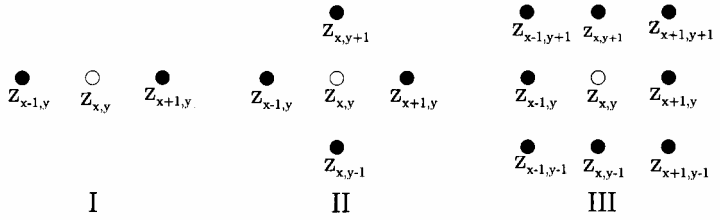

Figure 3.2 Summit definitions [49].

The summits are assumed to have a certain curvature ρ in the (measured) x and y direction. The radius of the summit can be related to the local curvature at the surface. The three point definition based on finite differences of a summit curvature ρ_i and its inverse parameter, the summit radius β_i, will be used and is defined as

$$\rho_{x,i} = -\frac{1}{\beta_{x,i}} = \frac{z_{x-1,y} - 2z_{x,y} + z_{x+1,y}}{r_x^2} \tag{3.4}$$

and

$$\rho_{y,i} = -\frac{1}{\beta_{y,i}} = \frac{z_{x,y-1} - 2z_{x,y} + z_{x,y+1}}{r_y^2}, \tag{3.5}$$

where $z_{x,y}$ is the local surface height at summit location (x,y) and r_x, r_y denote the interferometer pixel size in x and y direction respectively.

The mean curvature of a surface in x direction is given by taking the x curvatures of all n summits of the surface

$$\overline{\rho}_x = \frac{1}{n}\sum_{i=1}^{n}\rho_{x,i} . \tag{3.6}$$

The mean curvature in y direction is given by

$$\overline{\rho}_y = \frac{1}{n}\sum_{i=1}^{n}\rho_{y,i} . \tag{3.7}$$

Finally, the mean curvature $\overline{\rho}$ and the corresponding mean summit radius β is given by

$$\overline{\rho} = -\frac{1}{\beta} = \frac{1}{2}\left(\overline{\rho}_x + \overline{\rho}_y\right) \quad \text{or} \quad \beta = -\frac{2}{\overline{\rho}_x + \overline{\rho}_y} . \tag{3.8}$$

Alternatively, van der Heide [33] used another definition for the mean summit radius denoted by β_m based on the square root of the radii's product and is defined by

$$\beta_m = \frac{1}{n}\sum_{i=1}^{n}\sqrt{\beta_{x,i}\beta_{y,i}} . \tag{3.9}$$

Next to the mean summit radius β or β_m, two other statistical roughness parameters are commonly used in the characterisation of a summit height distribution. The first is the standard deviation of summit heights σ_s and is given by

$$\sigma_s^2 = \frac{1}{n}\sum_{i=1}^{n}\left(s_i - d_d\right)^2 , \tag{3.10}$$

with s_i the height of summit i, n the total number of asperities of the surface and d_d the distance between the mean line of the summits and the mean line through all the surface points. The third parameter is the density of asperities η and is given by

$$\eta = \frac{n}{A_{MRA}}, \tag{3.11}$$

with A_{MRA} the measured roughness area from interferometry.

Furthermore, for an isotropic rough surface a single summit can be characterised by an equivalent curvature ρ and is defined as

$$\rho_i = -\frac{1}{\beta_{sphere,i}} = \frac{\rho_{x,i} + \rho_{y,i}}{2}, \quad \frac{1}{\beta_{sphere,i}} = \frac{1}{2}\left(\frac{1}{\beta_{x,i}} + \frac{1}{\beta_{y,i}}\right) \tag{3.12}$$

and

$$\beta_{sphere,i} = 2\beta_i'. \tag{3.13}$$

Note the factor 2 difference between $\beta_{sphere,i}$ and the so-called reduced radius β_i' (see Eq. (3.2)). For anisotropic rough surfaces ($\beta_{x,i} \neq \beta_{y,i}$) the individual curvatures according to Eqs. (3.4) and (3.5) have to be applied.

3.3.3 Example

In Figure 3.3 the summit radius distribution in *x* and *y* direction as a function of the normalised separation (s_i/σ_s) is presented for a rough (reference) surface. It can be concluded that statistical roughness parameters do not provide an accurate description of individual surface roughness features. Therefore, the actual individual summit radii have to be taken into account in the deformation model.

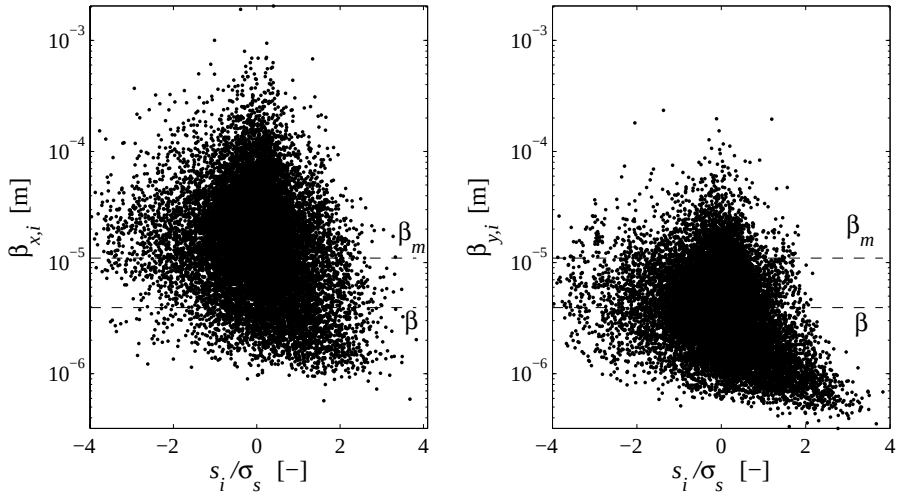

Figure 3.3 Summit radius distribution in *x* and *y* direction of a rough (reference) surface as a function of the normalised summit height, with β and β_m according to Eqs. (3.8) and (3.9).

Table 3.1 Statistical roughness characteristics of a rough ('reference') surface.

surface	β [m]	β_m [m]	σ_s [m]	η [m^{-2}]
rough	$3.93\ 10^{-6}$	$1.10\ 10^{-5}$	$2.33\ 10^{-7}$	$6.01\ 10^{10}$

3.4 AN ELLIPTIC ELASTIC/PLASTIC DEFORMATION MODEL OF A MICRO CONTACT

3.4.1 Introduction

The deformation of a roughness summit can be elastic, elastic-plastic or plastic depending on the applied load and contact characteristics like elasticity modulus, hardness and contact geometry. In this thesis it is assumed that a surface roughness summit can be regarded as an ellipsoid with curvatures in x and y direction cf. Eqs. (3.4) and (3.5), taking into account an anisotropic surface roughness. The contact situation of a smooth against a rough surface is adopted for simplicity.

3.4.2 Elastic Contact

When an ellipsoid with radii β_x and β_y is brought into contact with a flat counter surface according to the linear elasticity theory, an area of contact is formed with the shape of an ellipse, given by

$$\left(\frac{x}{a_{x,e}}\right)^2+\left(\frac{y}{a_{y,e}}\right)^2=1\,,\quad \text{with } a_{x,e}\le a_{y,e}\,, \tag{3.14}$$

where $a_{x,e}$ and $a_{y,e}$ are the minor and major semi axes of the contact ellipse respectively.

Hertz [36] demonstrated that the dimensions of the contact ellipse and the mutual approach of the contacting surfaces are determined by the axis ratio κ_e of the contact ellipse as a function of the ellipse ratio λ of principal curvatures ρ or radii β. κ_e and λ are given by

$$\kappa_e=\frac{a_{x,e}}{a_{y,e}}\quad\text{and}\quad \lambda=\frac{\rho_y}{\rho_x}=\frac{\beta_x}{\beta_y}\,. \tag{3.15}$$

Furthermore dimensionless elliptic axes $a'_{x,e}$ and $a'_{y,e}$ and a dimensionless mutual approach γ_e can be defined as

$$a'_{x,e} = \left(\frac{2\kappa_e \mathbf{E}(m)}{\pi} \right)^{1/3}, \; a'_{y,e} = \frac{a'_{x,e}}{\kappa_e} \quad \text{and} \quad \gamma_e = \frac{2\mathbf{K}(m)}{\pi a'_{y,e}}, \tag{3.16}$$

where $m = 1 - \kappa_e^2$ and $\mathbf{K}(m)$ and $\mathbf{E}(m)$ are the complete elliptic integrals of the first and second kind, respectively. Hertz [36] showed that the relation between κ_e (or m) and λ is given by

$$\lambda = (1-m)\frac{\mathbf{K}(m) - \mathbf{E}(m)}{\mathbf{E}(m) - (1-m)\mathbf{K}(m)}. \tag{3.17}$$

For the case $a_{x,e} > a_{y,e}$ a similar analysis can be carried out for calculating κ_e and λ substituting $a_{x,e}$ and ρ_x for $a_{y,e}$ and ρ_y respectively.

The contact area A_e will be calculated with the Hertzian theory for elliptical contacts. Ellipse (half) dimensions $a_{x,e}$ and $a_{y,e}$ are

$$a_{x,e} = a'_{x,e}\left(\frac{3F\beta'}{E'} \right)^{1/3} \quad \text{and} \quad a_{y,e} = a'_{y,e}\left(\frac{3F\beta'}{E'} \right)^{1/3}, \tag{3.18}$$

in which the reduced micro contact radius β' of two contacting surfaces is defined similarly as R', see Eq. (3.2) and taking into account that one surface is rough and the other smooth. This leads to the following equation

$$\frac{1}{\beta'} = \frac{1}{\beta_x} + \frac{1}{\beta_y}. \tag{3.19}$$

The contact area A_e follows from

$$A_e = \pi a_{x,e} a_{y,e}. \tag{3.20}$$

The mean Hertzian pressure $p_{e,mean}$ is given by

$$p_{e,mean} = \frac{F}{\pi a_{x,e} a_{y,e}} \tag{3.21}$$

and the maximum Hertzian pressure $p_{e,max}$ now follows from

$$p_{e,\max} = \frac{3F}{2\pi a_{x,e} a_{y,e}} = \frac{3}{2} p_{e,mean}. \tag{3.22}$$

The approach ω (see Figure 3.1) is given by

$$\omega = \gamma_e \left(\frac{9F^2}{8E'^2 \beta'} \right)^{1/3} . \tag{3.23}$$

Eq. (3.23) can be substituted into Eq. (3.18), then

$$a_{x,e} = a'_{x,e} \sqrt{\frac{2\omega\beta'}{\gamma_e}} \qquad \text{and} \qquad a_{y,e} = a'_{y,e} \sqrt{\frac{2\omega\beta'}{\gamma_e}} . \tag{3.24}$$

The summit contact area A_e follows from Eqs. (3.18) and (3.20)

$$A_e = \pi a_{x,e} a_{y,e} = \pi a'_{x,e} a'_{y,e} \left(\frac{3F\beta'}{E'} \right)^{2/3} . \tag{3.25}$$

In terms of the approach ω this micro contact area A_e is calculated by substituting Eq. (3.24) into Eq. (3.25)

$$A_e = \frac{2\pi a'_{x,e} a'_{y,e} \beta' \omega}{\gamma_e} . \tag{3.26}$$

The normal force F_e of the summit contact according to Eq. (3.23) is

$$F_e = \sqrt{\frac{8E'^2 \beta'}{9}} \left(\frac{\omega}{\gamma_e} \right)^{3/2} . \tag{3.27}$$

The mean Hertzian pressure $p_{e,mean}$ can be calculated by $p_{e,mean} = F_e / A_e$ and in terms of the approach ω this then becomes

$$p_{e,mean} = \frac{E'}{3\pi a'_{x,e} a'_{y,e}} \sqrt{\frac{2\omega}{\gamma_e \beta'}} . \tag{3.28}$$

The maximum Hertzian pressure $p_{e,max}$ follows from $p_{e,\max} = \frac{3}{2} p_{e,mean}$

$$p_{e,\max} = \frac{E'}{2\pi a'_{x,e} a'_{y,e}} \sqrt{\frac{2\omega}{\gamma_e \beta'}} . \tag{3.29}$$

3.4.3 Plastic Contact

So far the summits were assumed to deform only elastically. However, the asperities start to deform plastically at high values for the approach ω, say ω_e. Tabor [54] indicated that when the average Hertzian contact pressure reaches a value of 0.4 times the hardness H, initial yielding occurs. The value for ω_e can be found when combining Eqs. (3.21) and (3.23) and inserting $p = kH$ (with $k = 0.4$), this yields

$$\omega_e = \frac{9\gamma_e \beta'}{2}\left(\frac{\pi a'_{x,e} a'_{y,e} kH}{E'}\right)^2 . \tag{3.30}$$

At even higher values for the approach ω, say ω_p, the summit will deform fully plastically. This occurs for average Hertzian pressures equal to the (universal) hardness. The pressure does not increase any further than this value and remains at the value for H, thus

$$p_{mean,p} = H . \tag{3.31}$$

The contact area in the plastic regime is equal to the geometrical intersection of a flat with the original undeformed profile according to Abbot and Firestone [1]. This leads to the following expression for the approach ω

$$\omega = \frac{a_{x,p}^2}{2\beta_x} = \frac{a_{y,p}^2}{2\beta_y} \tag{3.32}$$

or

$$a_{x,p}^2 = 2\beta_x \omega \quad \text{and} \quad a_{y,p}^2 = 2\beta_y \omega . \tag{3.33}$$

Combining Eq. (3.33) with the elliptical contact area $A_p = \pi a_{x,p} a_{y,p}$ gives

$$A_p = 2\pi\omega\sqrt{\beta_x \beta_y} = 2\pi\omega\sqrt{\beta'(\beta_x + \beta_y)} . \tag{3.34}$$

The axes ratio in the plastic regime κ_p can now be defined as

$$\kappa_p \equiv \frac{a_{x,p}}{a_{y,p}} = \sqrt{\frac{\beta_x}{\beta_y}} = \sqrt{\lambda} . \tag{3.35}$$

Now, $a_{x,p}$ and $a_{y,p}$ can be determined by combining Eq. (3.35) and $A_p = \pi a_{x,p} a_{y,p}$, according to

$$a_{x,p} = \sqrt{\frac{\kappa_p A_p}{\pi}} \quad \text{and} \quad a_{y,p} = \sqrt{\frac{A_p}{\kappa_p \pi}} \,. \tag{3.36}$$

The force per asperity contact F_p follows from

$$F_p = p_{mean,p} A_p = H A_p = 2\pi\omega H \sqrt{\beta_x \beta_y} \,. \tag{3.37}$$

No solid expression is known for the critical approach, but according to Zhao et al. [60] an estimation can be found with a simple analysis. At $\omega = \omega_p$ the load carried by the contact is equal to F_p and in the elastic case the force at $\omega = \omega_p$ would be equal to Eq. (3.27). Then, the following inequality can be constructed

$$2\pi\omega_p H \sqrt{\beta_x \beta_y} < F_e = \sqrt{\frac{8E'^2\beta'}{9}} \left(\frac{\omega_p}{\gamma_e} \right)^{3/2} \tag{3.38}$$

or

$$\omega_p > \frac{9}{8} \frac{4\pi^2 \beta_x \beta_y H^2 \gamma_e^3}{E'^2 \beta'} = \left\{ \frac{9\gamma_e \beta'}{2} \left(\frac{\pi a'_{x,e} a'_{y,e} kH}{E'} \right)^2 \right\} \frac{\gamma_e^2}{a'^2_{x,e} a'^2_{y,e}} \frac{\beta_x \beta_y}{\beta'^2} \frac{1}{k^2} \,. \tag{3.39}$$

Substitution of Eq. (3.30) into Eq. (3.39) yields

$$\omega_p > \frac{\gamma_e^2}{a'^2_{x,e} a'^2_{y,e}} \frac{\beta_x \beta_y}{\beta'^2} \frac{1}{k^2} \omega_e \tag{3.40}$$

and hence as an approximation for ω_p Eq. (3.41) is given

$$\omega_{p,Zhao} \approx \frac{\gamma_e^2}{a'^2_{x,e} a'^2_{y,e}} \frac{\beta_x \beta_y}{\beta'^2} \frac{1}{k^2} \omega_e \,. \tag{3.41}$$

Another estimation can be found based on experimental results. Johnson [39] found for the indentation of a sphere on a plane, that fully plastic deformation takes place when the contact load $F_p(\omega_p)$ equals to 400 times $F_e(\omega_e)$ (at initial yielding). With Eqs. (3.26), (3.37) and $p = kH$, this results in

$$\frac{F_p(\omega_p)}{F_e(\omega_e)} = \frac{2\pi\omega_p H \sqrt{\beta_x \beta_y}}{2\pi a'_{x,e} a'_{y,e} \gamma_e^{-1} \beta' \omega_e kH} = 400 \,. \tag{3.42}$$

Now the expression for the critical approach at the elastic-plastic transition ω_p can be found by rearranging Eq. (3.42). The resulting Eq. (3.43) will be used throughout this thesis.

$$\omega_{p,Johnson} = 400k \frac{a'_{x,e} a'_{y,e}}{\gamma_e} \frac{\beta'}{\sqrt{\beta_x \beta_y}} \omega_e \,. \tag{3.43}$$

In Figure 3.4, the importance of taking into account the elastic-plastic regime is shown by means of the ratio ω_p/ω_e as a function of the ellipticity ratio $\lambda = \beta_x / \beta_y$ for both relations for ω_p. It can be seen that in case of Zhao's expression for ω_p, the elastic-plastic regime is much smaller (ω_p/ω_e is about 25) than in the case of the expression based on Johnson's experiments (ω_p/ω_e is about 80). Furthermore, Figure 3.4 shows that at increasing ellipticity Johnson's relations reaches full plasticity earlier than for $\lambda = 1$, this in contrast to Zhao's case.

Johnson's expression comes from measurements instead of a mathematical analysis like in Zhao's case. Therefore, Johnson's relation is more reliable and will be used throughout this thesis.

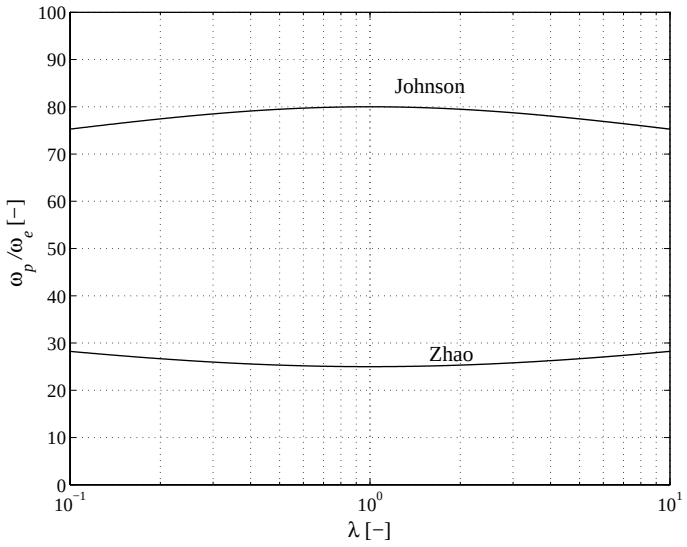

Figure 3.4 Ratio ω_p/ω_e, indicating the relative importance of the elastic-plastic regime, as a function of the ellipticity ratio λ.

3.4.4 Elastic-Plastic Contact

From the previous section it can be concluded that the importance of the elastic-plastic regime may not be underestimated. The relation for the contact area in the elastic-plastic regime is given by Zhao et al. [60], for spherical contacts. They use a cubic polynomial segment template of the form $y = -2x^3 + 3x^2$ to connect the elastic and the plastic asymptotes smoothly. For x is taken

$$x = \frac{\omega - \omega_e}{\omega_p - \omega_e}. \tag{3.44}$$

This relationship for the elastic-plastic contact area A_{ep} now reads

$$A_{ep} = A_e + \left(A_p - A_e\right)\left(-2x^3 + 3x^2\right). \tag{3.45}$$

With the assumption that this also holds for elliptical contacts and inserting Eqs. (3.26), (3.34) and (3.44) in Eq. (3.45), the relation for A_{ep} becomes

$$A_{ep} = 2\pi\beta'\omega\frac{a'_{x,e}a'_{y,e}}{\gamma_e} + \left\{\left(2\pi\omega\sqrt{\beta'(\beta_x+\beta_y)} - 2\pi\beta'\omega\frac{a'_{x,e}a'_{y,e}}{\gamma_e}\right)\times \left[-2\left(\frac{\omega-\omega_e}{\omega_p-\omega_e}\right)^3 + 3\left(\frac{\omega-\omega_e}{\omega_p-\omega_e}\right)^2\right]\right\}. \tag{3.46}$$

Furthermore, the same template that is used for A_{ep} i.e. $y = -2x^3 + 3x^2$ can now be applied to determine the axes ratio $a_{x,ep}/a_{y,ep} = \kappa_{ep}$ in the elastic-plastic regime. Now, Eq. (3.47) connects κ_e, given by Eq. (3.15) and κ_p, given by Eq. (3.35):

$$\kappa_{ep} = \frac{a_{x,ep}}{a_{y,ep}} = \kappa_e + \left\{\left(\kappa_p - \kappa_e\right)\left[-2\left(\frac{\omega-\omega_e}{\omega_p-\omega_e}\right)^3 + 3\left(\frac{\omega-\omega_e}{\omega_p-\omega_e}\right)^2\right]\right\}. \tag{3.47}$$

Now, $a_{x,ep}$ and $a_{y,ep}$ can be determined by

$$a_{x,ep} = \sqrt{\frac{\kappa_{ep}\,A_{ep}}{\pi}} \quad \text{and} \quad a_{y,ep} = \sqrt{\frac{A_{ep}}{\kappa_{ep}\,\pi}}. \tag{3.48}$$

For the elastic-plastic regime, Zhao et al. [60] presented a relationship between the average contact pressure and the approach for spherical indentations by Francis [21] and this relation is given by

$$p_{ep,mean} = H - \left[H(1-k)\frac{\ln\omega_p - \ln\omega}{\ln\omega_p - \ln\omega_e}\right], \tag{3.49}$$

with $k = 0.4$ and H the universal hardness. The assumption is made again that this also holds for elliptical contacts.

From Figure 3.6, it can be seen that this elastic-plastic pressure evolution has a discontinuity towards the fully plastic region (i.e. the hardness value), due to non-equal derivatives at $\omega = \omega_p$. An alternative expression for $p_{ep,mean}$ which connects the elastic and plastic pressures at ω_e and ω_p and has no discontinuities for these points, can be constructed in the form of an e-power curve fit according to

$$p_{ep,mean} = H - H(1-k)\exp\left(-\alpha \frac{\omega_p - \omega_e}{H(1-k)}\left(\frac{\omega - \omega_e}{\omega_p - \omega}\right)\right), \tag{3.50}$$

with

$$\alpha = \left(\frac{dp_e}{d\omega}\right)_{\omega=\omega_e}. \tag{3.51}$$

The contact load F_{ep} follows from

$$F_{ep} = p_{ep,mean} A_{ep}, \tag{3.52}$$

where $p_{ep,mean}$ and A_{ep} are according to Eqs. (3.46) and (3.50).

3.4.5 Results for Single Summit Contact

In this section the above mentioned expressions will be applied to evaluate the elastic, elastic-plastic and plastic (mechanical) contact characteristics for an example *single* summit contact. In Table 3.2 the mechanical properties of the rough and the smooth surface are presented. These values are used throughout this thesis (reference case).

Table 3.2 Mechanical properties of the smooth and rough surface (reference case).

surface	H [GPa]	E [GPa]	ν [-]
1. smooth	6.6	210	0.3
2. rough	6.6	210	0.3

In Figure 3.5, Figure 3.6 and Figure 3.7 the summit contact area is normalised with respect to the contact area at $\omega = \omega_e$, the summit contact pressure according to $p/(0.4H)$, the summit contact force is normalised with regard to $F(\omega_e)$ and the approach ω is normalised to ω_e.

From Figure 3.5, it can be seen that the elastic-plastic contact area A_{ep} for both ω_p according to Zhao and Johnson is smoothly connected to its elastic and plastic asymptotes, A_e and A_p. However, the summit contact pressure evolution according to Zhao (Eq. (3.49)) as shown in Figure 3.6, shows a discontinuity towards the plastic region at $\omega = \omega_p$. It can be seen that the e-power relation (Eq. (3.50)) smoothly connects at $\omega = \omega_p$.

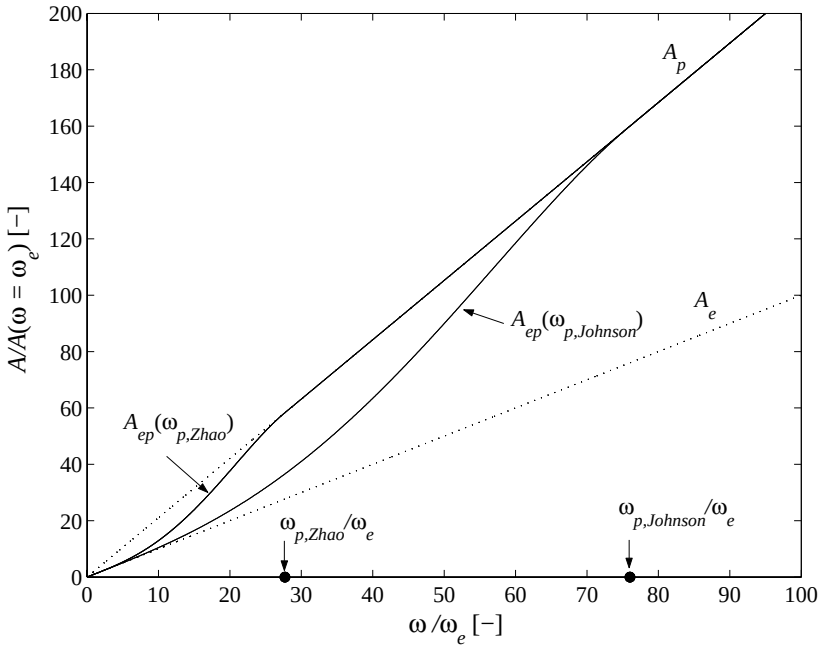

Figure 3.5 Normalised summit contact area versus normalised approach.

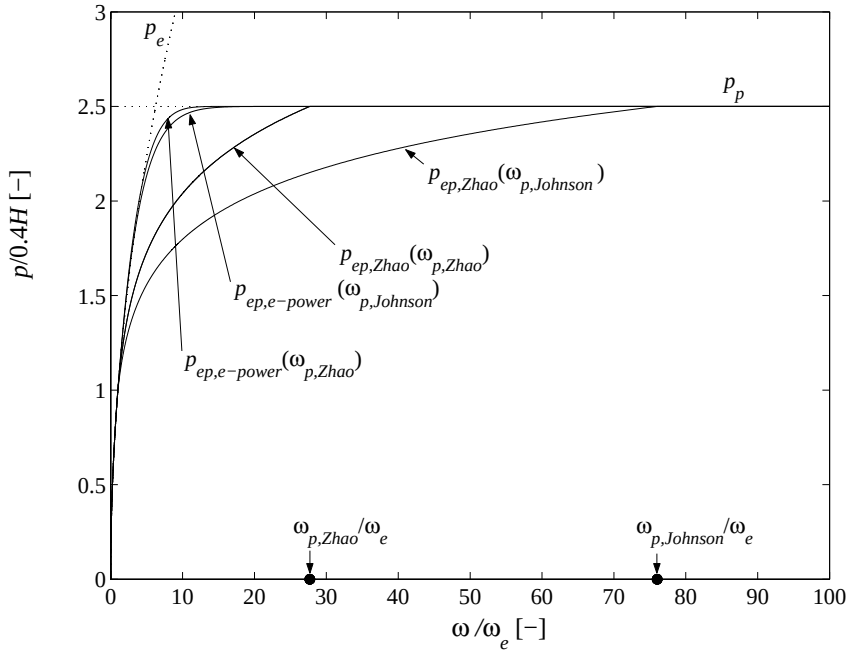

Figure 3.6 Normalised summit contact pressure versus normalised approach with $p_{mean,ep}$ according to Eq. (3.49) (Zhao) or Eq. (3.50) (e-power).

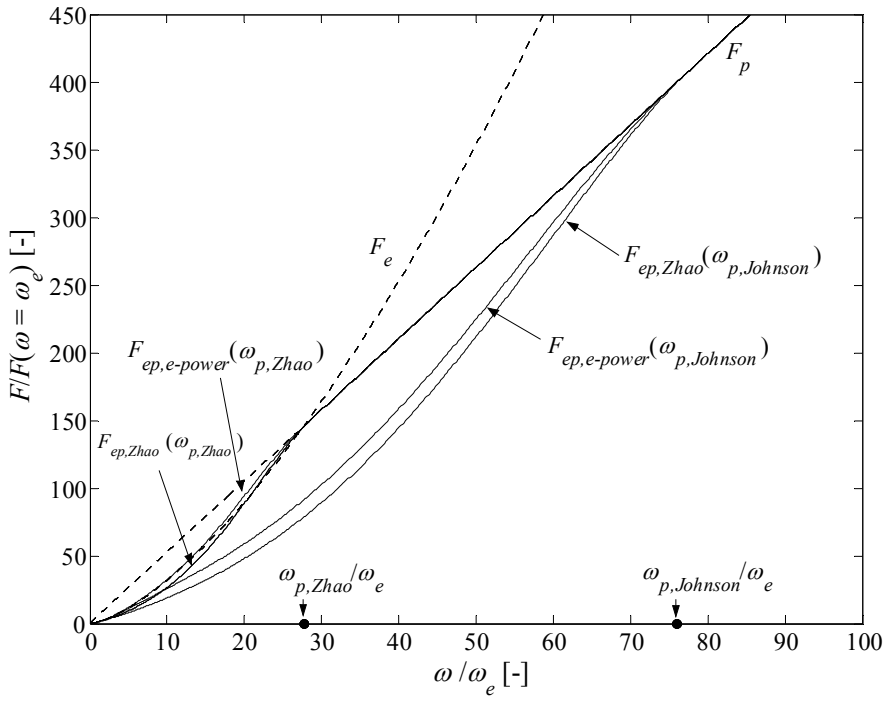

Figure 3.7 Normalised summit contact force versus normalised approach with $p_{mean,ep}$ according to Eq. (3.49) (Zhao) and Eq. (3.50) (e-power).

From Figure 3.7, it can be seen clearly that the expression for $p_{ep,mean}$ according to Zhao is based on the intersection point of F_e and F_p. Also, this figure obviously shows the factor 400 between $F_e(\omega_e)$ and $F_p(\omega_p)$ in case of Johnson's expression for ω_p, based on Eq. (3.42). Furthermore, the effect on F_{ep} of the two $p_{ep,mean}$ relations is small, therefore the smooth e-power function of Eq. (3.50) will be used in this thesis.

3.5 DEFORMATION MODEL

In order to calculate the flash temperature for every summit contact, the elastic and plastic contact characteristics (pressure, force, area and approach) per micro contact are needed. In order to get this information three steps are distinguished.

3.5.1 Step 1: Determine the Roughness Parameters

1.a. Input of measured roughness data *z(x,y)*;
1.b. Calculate the summits according to Eq. (3.3);
1.c. Calculate the summit curvatures and radii according to Eqs. (3.4) and (3.5).

3.5.2 Step 2: Macro Contact Characteristics

The measured roughness area from in this case interferometry is not equal to the deformed contact area. Therefore, the relation between these two has to be taken into account in order to calculate the ratio between the normal force of the macro contact (F) and the virtually applied normal force acting on the measured roughness area (F_{MRA}). Based on the assumption of a plan-parallel contact the average contact pressures must be the same, thus the force ratio can be defined as

$$F_{MRA} = \frac{A_{MRA}}{A_{Rough}} F \,, \tag{3.53}$$

where A_{Rough} is calculated for line contacts according to Eq. (A.7). This relation takes into account the influence of roughness in addition to the Hertzian solution for line contacts, see Appendix A. For point contacts, a similar analysis can be made based on the work of Greenwood and Tripp [29].

Up to now it was assumed that the total load F is only carried by the asperities, thus the contact is operating under BL conditions. From Chapter 2 it becomes clear that contacts can also fail from ML conditions. In ML (as pointed out in Section 1.2) the load is a combination of the load carried by the (E)HL film F_{EHL} and the contacting asperities F_C. According to Gelinck [25] this yields

$$F = F_C + F_{EHL} \,, \tag{3.54}$$

Based on Gelinck's relation for the coefficient of friction, μ, under ML conditions can be calculated by

$$\mu = \frac{\sum_{i=1}^{n} \iint_{A_{C_i}} \tau_{C_i} dA_{C_i} + \iint_{A_{EHL}} \tau_{EHL} dA_{EHL}}{F} = \frac{\mu_C F_C + \mu_{EHL} F_{EHL}}{F} \,, \tag{3.55}$$

in which τ_{C_i} and A_{C_i} are the shear stress and contact area at the asperity contact i and τ_{EHL} and A_{EHL} denote the shear stress and contact area of the hydrodynamic component. Furthermore, μ_C and μ_{EHL} are the coefficients of friction in the BL and EHL regime respectively.

The coefficient of friction for the boundary lubricated asperity contacts can be approximated as being constant and equal to μ_C, see Faraon [20]. Assuming the friction due to lubricant shear is small compared to the boundary component, Eq. (3.55) reduces to

$$\mu \approx \frac{\mu_C F_C}{F} \,. \tag{3.56}$$

Only the asperity force F_C has to be taken into account in Eq. (3.53), this leads to

$$F_{MRA} = \frac{A_{MRA}}{A_{Rough}} F_C \,. \tag{3.57}$$

3.5.3 Step 3: Micro Contact Characteristics

In order to calculate the normal force acting on a single summit, the macroscopic normal force acting in the contact is needed. The way this macroscopic normal force is divided over the several summits is presented here.

A separation h can be defined in which the sum of all the individual summit forces F_i equals the total normal force F_{MRA} according to

$$\sum_{i=1}^{N} F_i\left[h\left(s_i, \omega_i\right)\right] = F_{MRA}\,, \tag{3.58}$$

where N is the number of measured micro contacts.

The separation h can be defined as a function of the summit heights s_i and the approach ω_i according to (see Figure 3.1)

$$h = s_i - \omega_i \qquad \text{or} \qquad \omega_i = s_i - h\,. \tag{3.59}$$

The individual summit force is given by

$$F_i = p_i\left(\omega_i\right) A_i\left(\omega_i\right), \tag{3.60}$$

taking into account the elastic, elastic-plastic and plastic regimes as described in Section 3.4.

An iterative method is used to determine the resulting equilibrium separation h and corresponding ω_i for which Eq. (3.58) holds. With this separation h, the values for A_i, $a_{x,i}$, $a_{y,i}$, p_i and F_i for each asperity contact i can be calculated.

3.5.4 Example

As an example, the contact of the smooth cylinder against the rough flat surface is evaluated for a normal force F of 500 N under BL conditions. The roughness and mechanical characteristics are according to Table 3.1 and Table 3.2. In Figure 3.8, the distribution per summit of the pressure p_i, normal force F_i and contact area A_i is shown as a function of the dimensionless summit height s_i/σ_s. Furthermore, a 'pie' plot is presented in which the percentage of each deformation mode (elastic, elastic-plastic, plastic or undeformed) is shown.

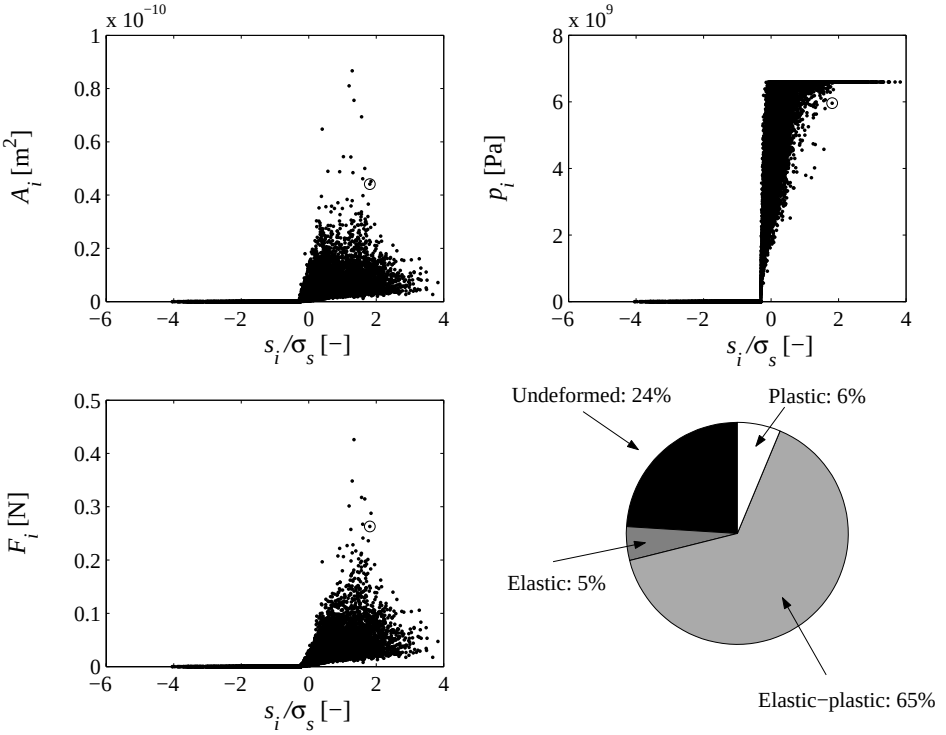

Figure 3.8 Distribution per summit of the pressure p_i, normal force F_i and contact area A_i as a function of the dimensionless summit height s_i/σ_s for the rough reference surface under conditions of boundary lubrication.

3.6 CONCLUSIONS AND SUMMARY

A deformation model is developed for lubricated rough contacts. This model takes into account the influence of surface roughness by means of a deterministic description. Furthermore, anisotropic asperities are incorporated in the model by assuming different summit radii in x and y direction. The mode of asperity deformation can be elastic, elastic-plastic or plastic. It takes into account the influence of lubricating regimes by incorporating Stribeck behaviour, meaning that part of the load is carried by the asperities and part by the (E)HL film. With this model, contact characteristics like pressure, force, area of contact and approach can be calculated for every single asperity. This model will serve as a basis for the temperature model as presented in the next chapter.

Chapter 4

Contact Temperature

4.1 INTRODUCTION

In Chapter 2 it is concluded that Blok's hypothesis of a critical contact temperature for scuffing, is the most promising one for further exploration and therefore this criterion is going to be evaluated in this thesis. The contact temperature according to Blok (Eq. (2.7)) consists of a quasi-steady surface or bulk temperature θ_s and an instantaneous contact or flash temperature rise θ_f. For the latter, Blok addressed the calculation only to the macro contact according to Eq. (2.9), resulting in one temperature for the contact situation, see Figure 4.1a. In Blok's approach scuffing will take place if

$$\theta_c = \theta_s + \theta_f \geq \theta_{cr} . \tag{4.1}$$

In this thesis a different approach is taken. The contact temperature will now be calculated for every micro contact *i*. In the new approach (Figure 4.1b) scuffing will take place if the contact temperature for a micro contact $\theta_{c,i}$ exceeds the critical temperature according to

$$\theta_{c,i} = \theta_s + \theta_{f,i} = \theta_j + \theta_{sr} + \theta_{f,i} \geq \theta_{cr} , \tag{4.2}$$

where the quasi-steady surface temperature θ_s consists of an inlet temperature θ_j and a quasi-steady surface temperature *rise* θ_{sr}.

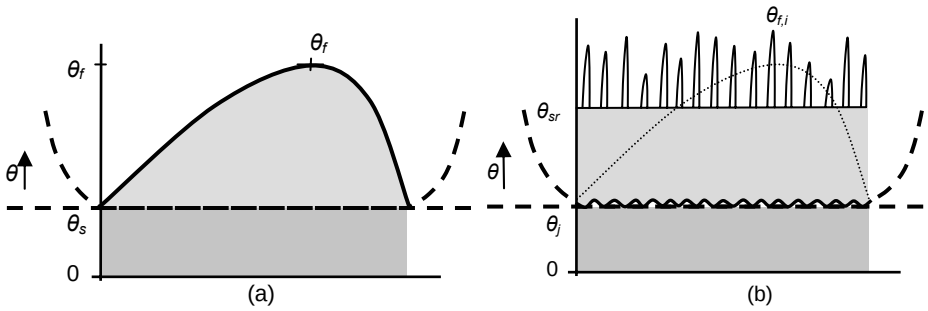

Figure 4.1 Contact temperature situation according to Blok (a) and this thesis (b).

4.2 CALCULATION OF CONTACT TEMPERATURE

4.2.1 Contact Temperature Model of Bos

In this section, a general method to calculate contact temperatures is presented according to a theory developed by Bos [8]. This theory will be used to calculate both the quasi-steady surface temperature θ_s (Section 4.2.2) and an instantaneous flash temperature rise per micro contact $\theta_{f,i}$ (Section 4.2.3).

Bos [8] has developed a model to predict contact temperatures for elliptical shaped heat sources. The results are presented in accurate close form fit formulas to avoid time-consuming numerical calculations and hence enhancing the practical applicability for the current multiple summit contact situation. Another advantage of this work is that the partition problem is solved simultaneously with the temperature problem, taking into account the division of the dissipated amount of generated heat in one body and the other. This approach is chosen instead of assuming a certain ratio for the partition of heat which is usually done.

As a basis for his work, Bos used the quasi-steady state surface temperature distribution for moving point sources of heat based on Green's function presented by Carslaw and Jaeger [11]. Heat is emitted at the origin of the heat source at the rate of one heat unit per unit time, and a semi-infinite homogeneous medium moves uniformly along the origin with velocity v parallel to the x-axis. This distribution is given by

$$G(x,y)=\frac{1}{2\pi K\sqrt{x^2+y^2}}\exp\left(-\frac{v}{2\kappa_{th}}\left(\sqrt{x^2+y^2}-x\right)\right), \tag{4.3}$$

where K is the thermal conductivity of the body and $\kappa_{th}=K\rho_d^{-1}c_p^{-1}$ its thermal diffusivity, with ρ_d the density and c_p the specific heat at constant pressure.

Taking into account a heat source of arbitrary shape and distribution $q(x,y)$ with area A_q, the quasi-steady state surface temperature rise is given by

$$\theta(x,y)=\int_{A_q} q(x',y')\,G(x-x',y-y')dx'dy'. \tag{4.4}$$

This integral for the temperature rise is solved for both high and low velocity cases indicated by θ_h and θ_l respectively. For the intermediate velocity case, an interpolation is used taking into account the elliptic shape of the contact according to

$$\theta^s=\theta_l^s+\theta_h^s \text{ with } s=0.5\cdot\exp(1-\kappa^{-1})-2.5, \tag{4.5}$$

in which κ is the contact ellipse axis ratio as discussed in Section 3.4.

Eq. (4.5) expresses the case in which all the heat is emitted to one single body. The next step is to take into account the tribological contact situation in which heat is generated at an elliptical shaped contact area and is dissipated to both interacting

surfaces. The way the heat is divided over the two bodies is called the heat partition problem. Bos [8] addressed this problem by assuming the following expression for the temperature rise θ as suggested by Archard [2]

$$\frac{1}{\theta} = \frac{1}{\theta_1} + \frac{1}{\theta_2}, \tag{4.6}$$

where θ_1 and θ_2 are the separate values for the maximum temperature rise for body 1 and 2 respectively and are given by Eqs. (4.4) and (4.5).

The shape of a contact can be assumed to be elliptical and the distribution of the heat supply can be assumed to be uniform or semi-ellipsoidal. Furthermore, the temperature is dependent of the direction of velocities of the bodies. Taking into account these factors, the temperature rise may be represented by

$$\theta = \frac{\mu F v}{\left(\frac{K_1}{\bar{\theta}_1} + \frac{K_2}{\bar{\theta}_2}\right)\sqrt{a_x a_y}}, \tag{4.7}$$

with μ the coefficient of friction, F the normal force, v the relative velocity between the two bodies, and a_x and a_y the elliptic half dimensions of the contact ellipse. An effective thermal conductivity K_{eff} can be defined as [47]

$$K_{eff} = \frac{K_1}{\bar{\theta}_1} + \frac{K_2}{\bar{\theta}_2}, \tag{4.8}$$

where the constants K_1 and K_2 represent the thermal conductivities for bodies 1 and 2 respectively. Combining Eq. (4.7) with Eq. (4.8) leads to the following equation for the temperature rise θ

$$\theta = \frac{\mu F v}{K_{eff}\sqrt{a_x a_y}}. \tag{4.9}$$

The dimensionless temperature numbers $\bar{\theta}_1$ and $\bar{\theta}_2$ in Eq. (4.8) are represented by

$$\bar{\theta}_1 = \left[\left\{\bar{\theta}_l^{kl}\mathbf{S}(\kappa)\right\}^s + \left(\bar{\theta}_h^{kl}\sqrt{\frac{\kappa}{Pe_1}}\right)^s\right]^{\frac{1}{s}} \text{ and } \bar{\theta}_2 = \left[\left\{\bar{\theta}_l^{kl}\mathbf{S}(\kappa)\right\}^s + \left(\bar{\theta}_h^{kl}\sqrt{\frac{\kappa}{Pe_2}}\right)^s\right]^{\frac{1}{s}}, \tag{4.10}$$

with s according to Eq. (4.5). The expression $\mathbf{S}(\kappa)$ in Eq. (4.10) is an elliptical shape factor given by

$$\mathbf{S}(\kappa) = \frac{2\sqrt{\kappa}}{1+\kappa}\frac{2}{\pi}\mathbf{K}\left(\frac{|1-\kappa|}{1+\kappa}\right), \tag{4.11}$$

where **K***(k)* represents the complete elliptical integral of the first kind with modulus k. The Péclet numbers Pe_1 and Pe_2 used in Eq. (4.10) are defined as (with the assumption that the x direction is the direction of motion)

$$Pe_1 = \frac{a_x v_1}{\kappa_{th,1}} \qquad \text{and} \qquad Pe_2 = \frac{a_x v_2}{\kappa_{th,2}}, \tag{4.12}$$

in which $\kappa_{th,1}$ and $\kappa_{th,2}$ are the respective thermal diffusivities of bodies 1 and 2.

In Eq. (4.10) the auxiliary temperature number for the high velocity case $\bar{\theta}_h^{kl}$ depends on the direction of the velocities with respect to the contact according to

$$\bar{\theta}_h^{kl} = \frac{\bar{\theta}_r^{kl} + t\bar{\theta}_s^{kl}}{1+t}, \tag{4.13}$$

in which

$$t = \max\left(0, \frac{-q}{1+q}\right) \tag{4.14}$$

and

$$q = sign(v_1 \cdot v_2)\min\left(p, \frac{1}{p}\right) \quad \text{and} \quad p = \sqrt{\left|\frac{Pe_2}{Pe_1}\right|}. \tag{4.15}$$

The dimensionless temperature numbers $\bar{\theta}_r^{kl}$, $\bar{\theta}_l^{kl}$ and $\bar{\theta}_s^{kl}$ depend on the indices k and l. The index l denotes whether an **a**verage or a **m**aximum temperature rise is concerned and the index k depicts the form of the heat supply distribution: **u**niform or semi-**e**llipsoidal. The values for these constants are listed in Table 4.1.

Table 4.1 Dimensionless temperature numbers [8].

	Uniform heat supply distribution		Semi-**e**llipsoidal heat supply distribution	
	Average	**M**aximum	**A**verage	**M**aximum
$\bar{\theta}_l$	$\bar{\theta}_l^{ua} = 0.270190$	$\bar{\theta}_l^{um} = 0.318310$	$\bar{\theta}_l^{ea} = 0.281250$	$\bar{\theta}_l^{em} = 0.375000$
$\bar{\theta}_r$	$\bar{\theta}_r^{ua} = 0.309955$	$\bar{\theta}_r^{um} = 0.507949$	$\bar{\theta}_r^{ea} = 0.322991$	$\bar{\theta}_r^{em} = 0.589487$
$\bar{\theta}_s$	$\bar{\theta}_s^{ua} = 0.406359$	$\bar{\theta}_s^{um} = 0.507949$	$\bar{\theta}_s^{ea} = 0.437504$	$\bar{\theta}_s^{em} = 0.700792$

For velocities of surfaces in the same direction, or when one of the surfaces has no velocity, t becomes zero and thus Eq. (4.13) reduces to

$$\bar{\theta}_h^{kl} = \bar{\theta}_r^{kl}. \tag{4.16}$$

4.2.2 Calculation of the Quasi-Steady Surface Temperature

When a contact runs some time under certain operating conditions, frictional heating takes place and depending on the heat dissipation a certain average temperature rise θ_{sr} arises. Together with the oil inlet temperature this yields the total quasi-steady surface temperature θ_s according to Ku et al. [41], see Eq. (2.10). In order to complete this relation, fit factors from measurements are used, which makes it less suitable for modelling purposes. Therefore, the theory of the previous section using the average macro contact properties, will be adopted. Eq. (2.10) can now be adapted and the time and space average quasi-steady surface temperature θ_s, taking into account Eq. (4.9), becomes

$$\theta_s = \theta_j + \theta_{sr} = \theta_j + \frac{\mu F v}{K_{eff}\sqrt{a_x a_y}}, \tag{4.17}$$

where μ is the average/macro coefficient of friction according to the Stribeck curve, F is the total normal force of the macro contact, K_{eff} is the effective macro thermal conductivity given by Eq. (4.8), a_x and a_y are the half dimensions of the macro contact ellipse. Furthermore, the average dimensionless temperature numbers have to be taken from Table 4.1 for the calculation of K_{eff}. θ_j is the oil inlet temperature or the bulk temperature.

4.2.3 Calculation of the Flash Temperature

Frictional heating takes place instantaneously in the micro contacts of two interacting surfaces. The resulting temperature rise in such a micro or asperity contact depends on the balance between the generation of heat by friction, and the dissipation of heat away from the asperity contact, and is labelled as flash temperature.

The flash temperature rise $\theta_{f,i}$ can be calculated by applying Eq. (4.9) for every single micro contact i. This yields

$$\theta_{f,i} = \frac{\mu_i F_i v}{K_{eff,i}\sqrt{a_{x,i} a_{y,i}}}, \tag{4.18}$$

with

$$K_{eff,i} = \frac{K_1}{\overline{\theta}_{1,i}} + \frac{K_2}{\overline{\theta}_{2,i}}. \tag{4.19}$$

The mechanical asperity contact properties, F_i, $a_{x,i}$ and $a_{y,i}$, are given by the deformation model developed in the previous chapter. The local coefficient of friction in an asperity contact can be assumed to be equal to the boundary lubrication value, μ_C.

4.2.4 Total Asperity Contact Temperature

The total asperity contact temperature at asperity i is labeled as $\theta_{c,i}$ and, analogous to Eq. (2.7), it results from combining Eq. (4.17) and (4.18). The quasi-steady surface temperature *rise* will be labeled as θ_{sr} from now. This all leads to the following expression for the total asperity contact temperature

$$\theta_{c,i} = \theta_j + \theta_{sr} + \theta_{f,i} \tag{4.20}$$

or

$$\boxed{\theta_{c,i} = \theta_j + \frac{\mu F v}{K_{eff}\sqrt{a_x a_y}} + \frac{\mu_i F_i v}{K_{eff,i}\sqrt{a_{x,i} a_{y,i}}}} \tag{4.21}$$

4.3 TEMPERATURE CALCULATION EXAMPLE

Again, the tribological contact situation of a stationary smooth surface (index 1) sliding against a moving flat rough surface (index 2) is taken as an example in order to calculate the contact temperature. For this reference case, the thermal properties are given in Table 4.2, whereas the roughness and mechanical characteristics of the two surfaces are according to Table 3.1 and Table 3.2.

Table 4.2 Thermal properties of the smooth and the rough surface (reference case).

surface	K [W m^{-1} K^{-1}]	ρ_d [kg m^{-3}]	c_p [J kg^{-1} K^{-1}]
1. smooth	45	7.8 10^3	477
2. rough	45	7.8 10^3	477

4.3.1 Quasi-Steady Surface Temperature: Macro Contact

The quasi-steady surface temperature can be calculated using Eq. (4.17). The oil inlet temperature θ_j is constant and equal to 100ºC. As explained in Section 4.2.2, the average contact properties have to be taken into account for the quasi-steady situation, leading to the use of the average, uniform dimensionless temperature numbers from Table 4.1 (indices k and l are u and a).

For the example cases, a line contact is taken with a smooth cylinder against a rough flat surface. In case of a line contact (see Appendix A), values for a_x and a_y can be approximated by $a_y = \ell/2$ and a_x then follows from area conservation: $A = \pi a_x a_y = 2b\ell$. This leads to $a_x = 4b/\pi$. The smooth surface is stationary, thus $t = 0$ and Eq. (4.16) is valid: $\bar{\theta}_h^{kl} = \bar{\theta}_r^{kl}$. Furthermore, $Pe_1 = 0$ and this reduces Eq. (4.10) for surface 1 to

$$\bar{\theta}_1 = \bar{\theta}_l^{ua}\mathbf{S}(\kappa). \tag{4.22}$$

For the moving surface 2, this yields

$$\overline{\theta}_2 = \left[\left\{ \overline{\theta}_l^{ua} \mathbf{S}(\kappa) \right\}^s + \left(\overline{\theta}_r^{ua} \sqrt{\frac{\kappa}{Pe_2}} \right)^s \right]^{\frac{1}{s}} . \tag{4.23}$$

For two example cases modelling results have been generated. In the first case, i.e. the reference case, the contact is loaded by F = 500 N with a velocity of v_2 = 1 m/s under conditions of boundary lubrication ($\mu = \mu_C$ = 0.15). In the second case, an example is given for a contact operating in the mixed lubrication regime. According to the Stribeck curve the coefficient of friction at higher velocities is lower than its boundary value (μ_C = 0.15), and at v = 5.25 m/s the coefficient of friction μ can be assumed to be 0.07. An overview of the modelling conditions and results is presented in Table 4.3.

Table 4.3 Modelling conditions and results.

		reference case 1	case 2		
	property	value	value	unit	description
Operating conditions	μ	0.15	0.07	[-]	coefficient of friction
	μ_C	0.15	0.15	[-]	coefficient of friction in BL
	F	500	100	[N]	load
	v	1	5.25	[m/s]	relative velocity
	R'	2	2	[mm]	reduced radius
	ℓ	3.4	3.4	[mm]	contact length
	θ_j	25	25	[ºC]	oil inlet temperature
Results	p_{mean}	1291	577	[MPa]	average Hertzian pressure
	p_h	1643	735	[MPa]	maximum Hertzian pressure
	A	$3.9\ 10^{-7}$	$1.7\ 10^{-7}$	[m^2]	Hertzian contact area
	b	$5.7\ 10^{-5}$	$2.5\ 10^{-5}$	[m]	Hertzian half width
	$p_{RoughLine}$	1130	396	[MPa]	rough line average pressure
	$A_{RoughLine}$	$4.4\ 10^{-7}$	$2.6\ 10^{-7}$	[m^2]	rough line area
	$b_{RoughLine}$	$6.5\ 10^{-5}$	$3.7\ 10^{-5}$	[m]	rough line half width
	κ	0.049	0.028	[-]	ellipse ratio
	a_x	$8.3\ 10^{-5}$	$4.8\ 10^{-5}$	[m]	ellipse semi axis in x direction
	a_y	$1.7\ 10^{-3}$	$1.7\ 10^{-3}$	[m]	ellipse semi axis in y direction
	Pe_1	0	0	[-]	Péclet number
	Pe_2	6.8	21.5	[-]	Péclet number
	$\overline{\theta}_1$	0.17	0.14	[-]	temperature number
	$\overline{\theta}_2$	0.03	0.01	[-]	temperature number
	K_{eff}	1997	4262	[$Wm^{-1}K^{-1}$]	effective conductivity
	θ_{sr}	100.1	30.4	[ºC]	quasi-steady surface temp. rise
	θ_s	125.1	55.4	[ºC]	quasi-steady surface temperature

It can be seen that for the reference case (case 1) the quasi-steady temperature rise θ_{sr} is 100.1ºC. Together with an oil inlet temperature of 25ºC, this results in a total quasi-steady surface temperature of 125.1ºC. For case 2, the average temperature rise is only 30.4ºC. The total average heat input Q is for case 1 is a factor of two higher than for case 2. The temperature rise difference is more than a factor of three, which is due to lower values of K_{eff} and a_x, which are both almost a factor of two lower.

Furthermore, these results show that for case 1 the relatively high normal force leads to a small difference (14%) when comparing p_{Hertz} and $p_{RoughLine}$, in contrast with case 2, where the lower normal force leads to a larger difference (46%) between p_{Hertz} and $p_{RoughLine}$, which is in accordance with Gelinck's theory as outlined in Appendix A.

4.3.2 Flash Temperature: Micro Contacts

4.3.2.1 General Considerations

In order to calculate the flash temperature for all asperity contacts Eq. (4.18) has to be evaluated. The contact characteristics given by the deformation model of Chapter 3 for the elliptical asperity contacts can be applied directly. In contrast to the quasi-steady surface temperature, now the maximum, elliptical temperature numbers (index e and m for k and l) of Table 4.1 have to be used. Similar to the quasi-steady surface temperature, $\overline{\theta}_{1,i}$ can be written as

$$\overline{\theta}_{1,i} = \overline{\theta}_l^{em} \mathbf{S}(\kappa_i) \tag{4.24}$$

and for asperities of the moving surface 2, $\overline{\theta}_{2,i}$ follows from

$$\overline{\theta}_{2,i} = \left[\left\{ \overline{\theta}_l^{em} \mathbf{S}(\kappa_i) \right\}^{s_i} + \left(\overline{\theta}_r^{em} \sqrt{\frac{\kappa_i}{Pe_{2,i}}} \right)^{s_i} \right]^{\frac{1}{s_i}}. \tag{4.25}$$

In Figure 4.2 the effective conductivity $K_{eff,i}$ as a function of Péclet number $Pe_{2,i}$ and axis ratio κ_i is presented for the parameter values as shown in Table 4.2. This figure reveals the necessity of taking into account the anisotropic nature of the roughness summits i.e. taking separate values for the summit radii β_i in x and y direction according to Eqs. (3.4) and (3.5) and leading to $\kappa_i \neq 1$.

In order to illustrate this influence of direction on the effective conductivity $K_{eff,i}$, two summits C and D are taken with the same area of contact A_i. This yields according to Eq. (3.20)

$$A_i = \left(\pi a_{x,i} a_{y,i}\right)_C = \left(\pi a_{x,i} a_{y,i}\right)_D \tag{4.26}$$

and assume

$$\left(\kappa_i\right)_C = \left(\kappa_i^{-1}\right)_D \Leftrightarrow \left(\frac{a_{x,i}}{a_{y,i}}\right)_C = \left(\frac{a_{y,i}}{a_{x,i}}\right)_D = \frac{1}{2}. \tag{4.27}$$

Furthermore, assume

$$\frac{v_2}{\kappa_{th,2}} = 1 \ , \ \left(a_{x,i}\right)_C = \left(a_{y,i}\right)_D = 5 \text{ and } \left(a_{y,i}\right)_C = \left(a_{x,i}\right)_D = 10 . \tag{4.28}$$

This leads to effective conductivity $K_{eff,i}$ values of 385.9 and 348.1 $Wm^{-1}K^{-1}$ for repectively C and D.

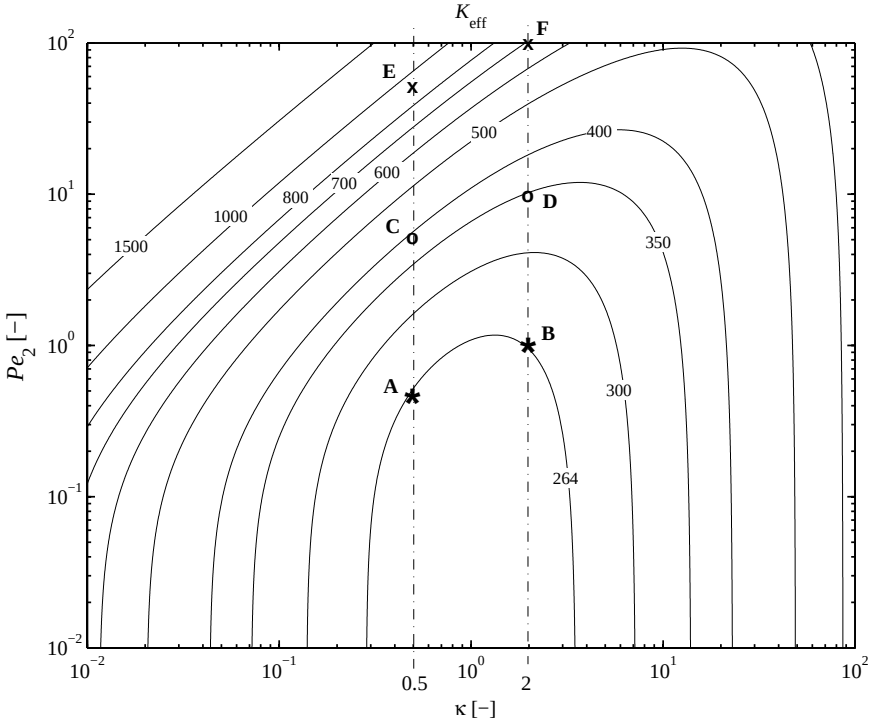

Figure 4.2 K_{eff} as a function of Pe_2 and κ with the assumption that $Pe_1 = 0$.

It can now be concluded that the summit with the narrow contact ellipse (in direction of velocity: *x*), i.e. summit C, is able to conduct the largest amount of heat and leads to lower flash temperatures according to Eq. (4.18). Summits C and D are indicated in Figure 4.2. These and other examples (A-B and E-F) are listed in Table 4.4. It can be seen that for higher *Pe* numbers (increasing velocity), the influence of direction on $K_{eff,i}$ is increasing.

Table 4.4 Influence of the shape of the contact ellipse on $K_{eff,i}$.

		$a_{x,i}$ [m]	$a_{y,i}$ [m]	κ_i [-]	$Pe_{2,i}$ [-]	$K_{eff,i}$ [$Wm^{-1}K^{-1}$]
1	A	0.5	1	0.5	0.5	*263.3*
	B	1	0.5	2	1	*264.8*
2	C	5	10	0.5	5	*385.9*
	D	10	5	2	10	*348.1*
3	E	50	100	0.5	50	891.8
	F	100	50	2	100	690.2

4.3.2.2 Reference Case

The flash temperatures will now be calculated for the reference case from the previous sections. The mechanical contact characteristics for this reference case are presented in Sections 2.3.5 and 2.4.4. The input parameters are presented in Table 4.3. The summit with the highest flash temperature will be indicated with a circle (o). From Figure 4.3 it can be seen that the highest flash temperatures $\theta_{f,i}$ do not occur at the highest peaks i.e. large values for the summit height s_i. Furthermore, it can be noticed that a large approach ω_i of a certain summit does not have to lead to the highest flash temperature $\theta_{f,i}$.

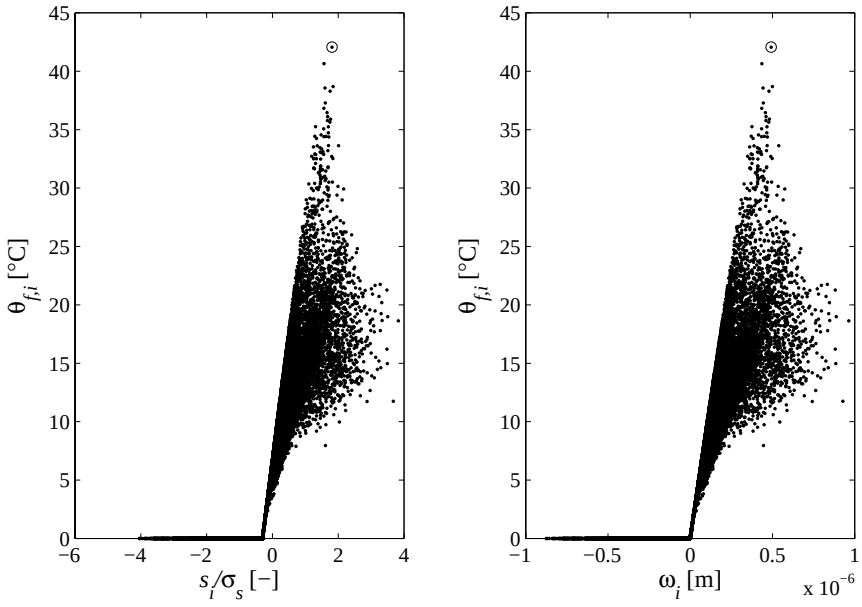

Figure 4.3 Micro contact flash temperature $\theta_{f,i}$ as a function of the dimensionless summit height s_i/σ_s for the reference case.

Figure 4.4 shows, for these cases, that high flash temperatures $\theta_{f,i}$ do not have to arise at summit radii close to the mean summit radius β (dashed line) as defined by Eq. (3.8). Additionally, it can be concluded that the contact model does not react with high flash temperatures $\theta_{f,i}$ to extreme values (due to possible measurement inaccuracies) for the three main input roughness parameters s_i, $\beta_{x,i}$ and $\beta_{y,i}$.

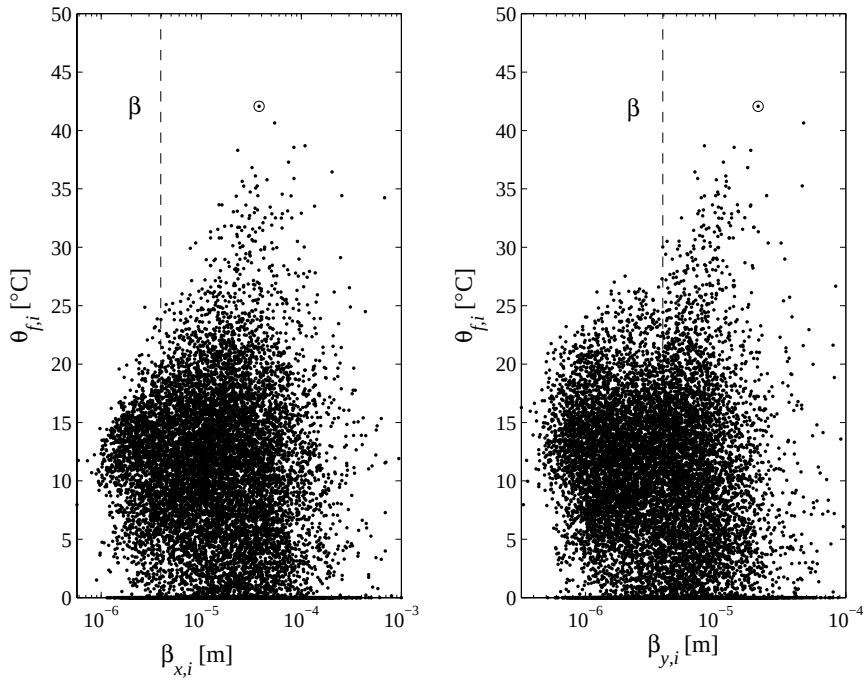

Figure 4.4 Micro contact flash temperature $\theta_{f,i}$ as a function of the summit radii in x and y direction ($\beta_{x,i}$ and $\beta_{y,i}$) for the reference case.

From Figure 4.5 it can be seen that both low and high values of the effective conductivity $K_{eff,i}$ exhibit the largest flash temperatures. The factor $(a_{x,i}a_{y,i})^{0.5}$ is an indication for the micro contact dimensions. It can also be said that both large and low values for this factor result in high flash temperatures.

In Figure 4.6 the denominator of the flash temperature equation (4.18), i.e. $K_{eff,i}(a_{x,i}a_{y,i})^{0.5}$ is presented as a function of the numerator, $Q_i = \mu_i F_i v$, for all micro contacts. It can be seen that the highest flash temperature value, indicated by a circle, does not occur at maximum heat input Q_i. This is different compared to the macroscopic situation according to Eq. (4.17), in which an increasing heat input always results in an increasing (quasi-steady surface) temperature, because the macroscopic product of $(a_{x,i}a_{y,i})^{0.5}$ and $K_{eff,i}$ decreases disproportionately slower than the increase of Q_i. In general, it can be concluded from Figure 4.5 and Figure 4.6 that a complex combination of factors is responsible for exhibiting the high micro contact flash temperature.

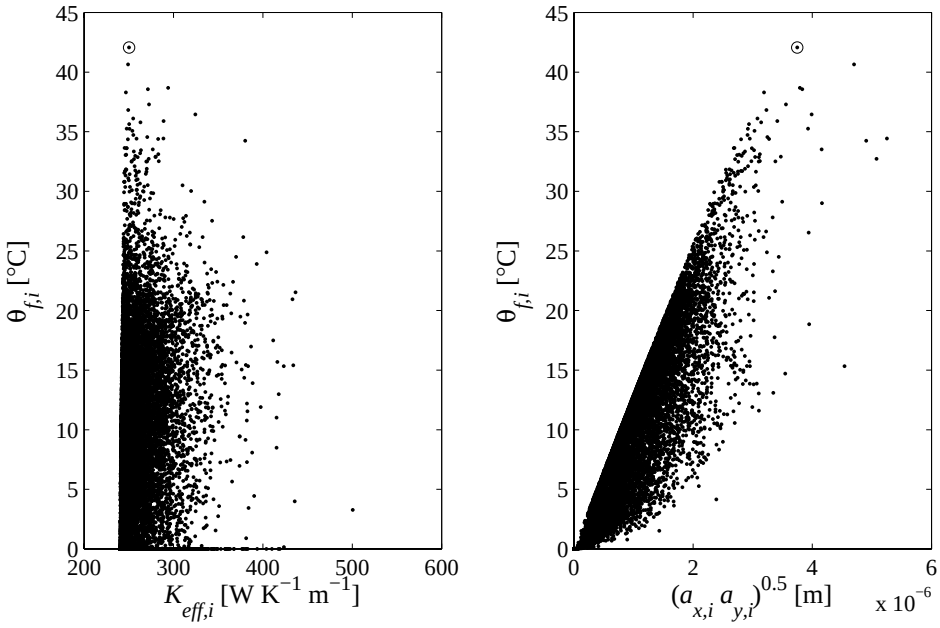

Figure 4.5 Micro contact flash temperature $\theta_{f,i}$ as a function of $K_{eff,i}$ and $(a_{x,i}.a_{y,i})^{0.5}$ for the reference case.

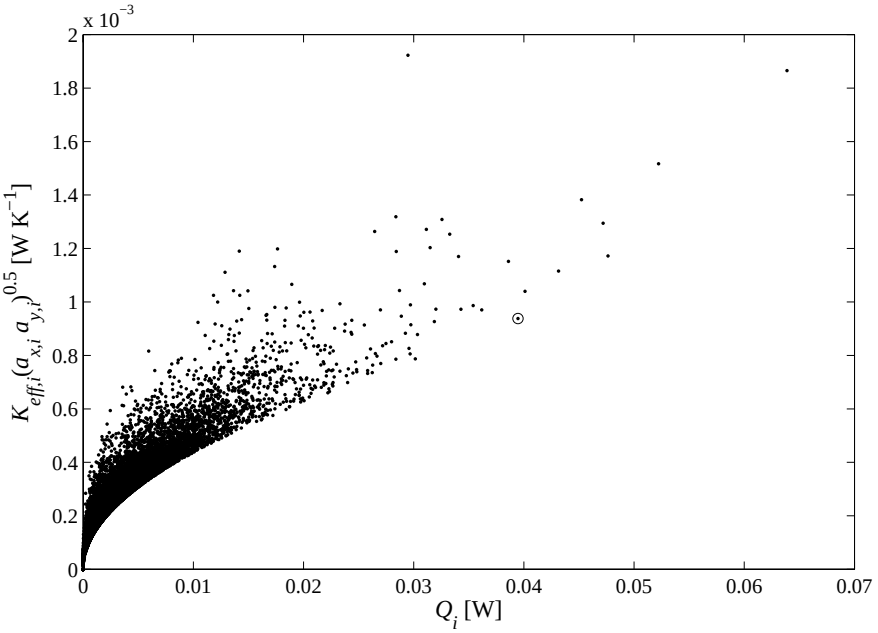

Figure 4.6 Heat dissipation $K_{eff,i}(a_{x,i}.a_{y,i})^{0.5}$ vs. heat generation $Q_i = \mu_i F_i v_i$ for the reference case.

4.4 CONCLUSIONS

The contact temperature model of Bos is used to calculate both the quasi-steady surface temperature and the micro contact flash temperature, in combination with the (mechanical) deformation model as developed in Chapter 3. Now, the total contact temperature can be calculated for combinations of operating conditions and structural parameters and hence with a certain critical temperature, a transition diagram can be determined for these parameters. The transition diagram is studied in the next chapter.

Chapter 5

Transition Diagram Model

5.1 INTRODUCTION

In the previous chapters, a method to predict the deformation and contact temperature of lubricated rough contacts was developed. The mechanical and thermal contact properties are now available at macro and micro scale for a wide range of operating conditions and structural parameters. A transition diagram can be modelled based on the constant critical temperature hypothesis. The calculated temperatures can be represented as iso-thermal lines and then the critical temperature iso-therm indicates the transition from mild to adhesive wear.

The transition I/II to III* (or III) is assumed to occur based on the hypothesis that the temperature (Eq. (4.20)) exceeds the critical temperature locally. Thus, local failure takes place if

$$\theta_{c,i} \geq \theta_{cr} \,. \tag{5.1}$$

Now, the following criterion can be constructed which represents the transition

$$\left(\theta_{c,i}\right)_{\max} = \theta_{cr} \tag{5.2}$$

with

$$\left(\theta_{c,i}\right)_{\max} = \theta_j + \theta_{sr} + \left(\theta_{f,i}\right)_{\max} . \tag{5.3}$$

5.2 TRANSITION DIAGRAM MODELLING

The transition diagram will be modelled using data from the reference case as presented in the previous chapters. In the next section, the transition diagram for a certain critical temperature is presented. But first, in this section, the separate contributions of θ_{sr} and $(\theta_{f,i})_{\max}$ to $(\theta_{c,i})_{\max}$ are presented.

In Figure 5.1, the quasi-steady surface temperature rise θ_{sr} is calculated as a function of F and v. In this case the coefficient of friction μ is constant. If there would only be the influence of heat generation, the contribution of only F and v should lead to hyperbolic equidistant iso-thermals. It can be seen clearly that for a certain load F, where $(a_x a_y)^{0.5}$ is constant, curves start to appear at larger intervals for increasing v. This clearly indicates the influence of the Pe number which leads to a higher effective conductivity K_{eff} at higher velocities and subsequently leads to a relatively lower temperature.

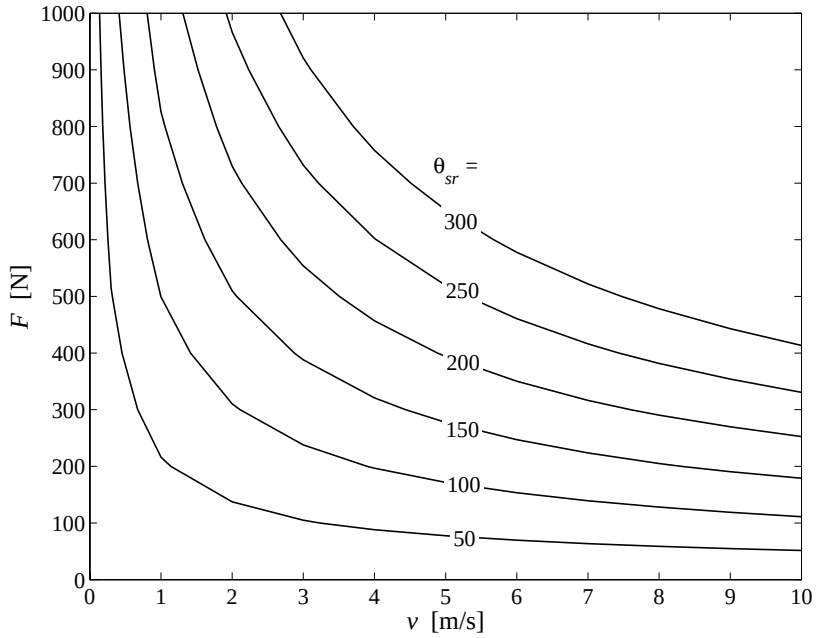

Figure 5.1 Quasi-steady surface temperature rise θ_{sr} as a function of F and v for the reference case (for input parameters: see Table 3.1, Table 3.2 and Table 4.3).

In Figure 5.2 the calculation of the maximum micro contact flash temperature $(\theta_{f,i})_{\max}$ is presented. From this figure, it can be seen that for low velocity, $(\theta_{f,i})_{\max}$ hardly changes with increasing applied (macroscopic) load F (again μ is assumed to be constant and equal to μ_C). At constant low velocity, this clearly indicates that the combination $F_i/(a_{x,i}a_{y,i})^{0.5}$ is nearly constant. For higher velocities, the Pe number increases and this leads to an increase of $K_{eff,i}$. Subsequently, this relatively lowers the increase in flash temperature, similar to the macroscopic case, for higher velocities.

An additional flash temperature lowering effect at higher loads at high velocity comes from the fact that $a_{x,i}$ is increasing with load F, leading to higher Pe numbers. In Figure 4.1 it is shown that $K_{eff,i}$ is increasing much faster for higher Pe numbers.

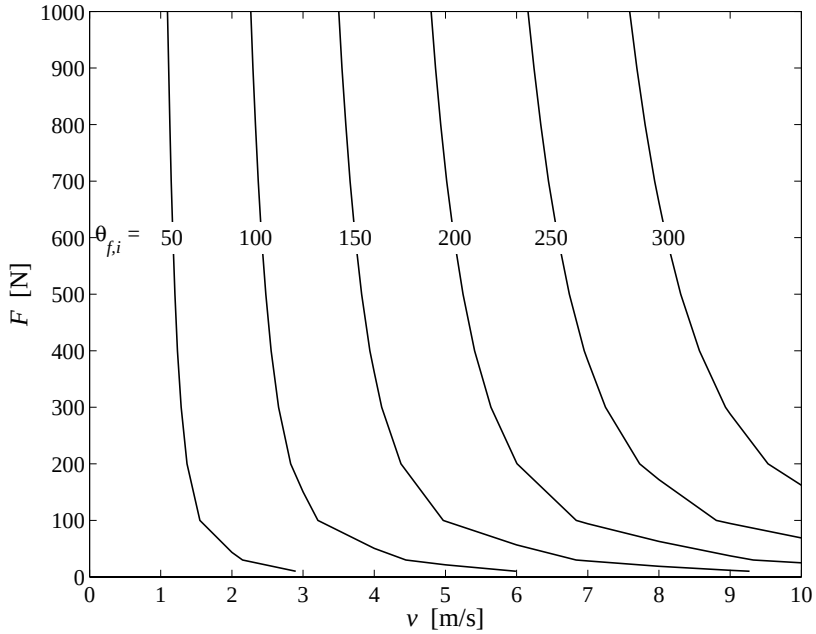

Figure 5.2 Maximum micro contact flash temperature $(\theta_{f,i})_{max}$ as a function of F and v for the reference case (for input parameters: see Table 3.1, Table 3.2 and Table 4.3).

The contributions of θ_{sr} and $(\theta_{f,i})_{max}$, together with a constant θ_j can be combined to achieve the F/v diagram for the total maximum micro contact temperature $(\theta_{c,i})_{max}$. Moreover, the inlet temperature θ_j is independent of F and v and therefore, Eq. (5.3) can be written as

$$\left(\theta^*_{c,i}\right)_{\max} \equiv \left(\theta_{c,i}\right)_{\max} - \theta_j = \theta_{sr} + \left(\theta_{f,i}\right)_{\max}, \tag{5.4}$$

where $\left(\theta^*_{c,i}\right)_{\max}$ is defined as the maximum micro contact temperature rise. For several values of the temperature rise $\left(\theta^*_{c,i}\right)_{\max}$, the resulting F/v diagram is shown in Figure 5.3. If the critical temperature of a certain lubricant is known in combination with the operating conditions and structural parameters, including the inlet temperature θ_j, the transition diagram can be determined.

In the next section, an investigation is carried out on the influence of several important parameters on this transition diagram, assuming a certain critical temperature rise.

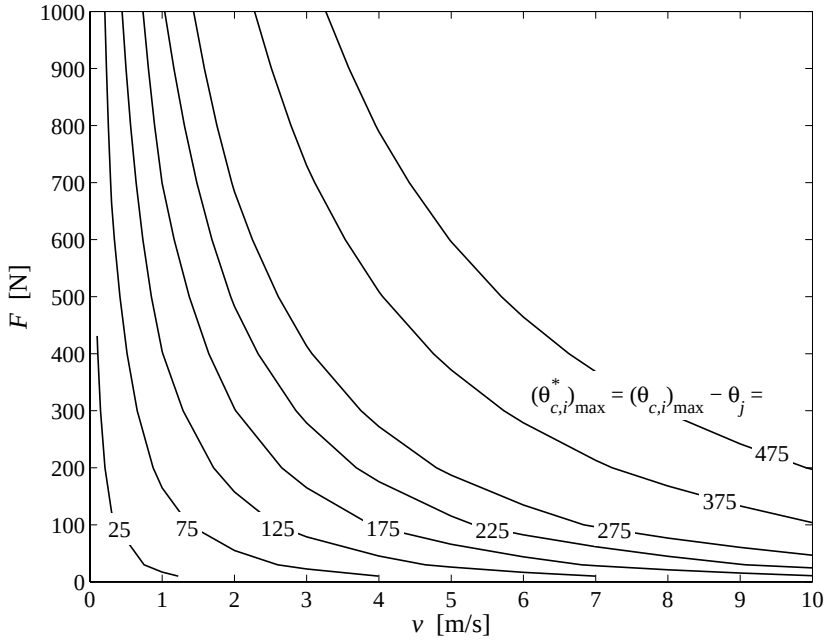

Figure 5.3 Total maximum micro contact temperature rise $(\theta^*_{c,i})_{max}$, according to Eq. (5.4), as a function of F and v for the reference case (for input parameters: see Table 3.1, Table 3.2 and Table 4.3).

5.3 PARAMETER STUDY

In this section the value of different parameters, which influence the transition diagram, will be varied. These parameters are: the reduced radius R', the reduced elasticity modulus E', the length of the line contact ℓ, the hardness H, the coefficient of friction μ, the critical temperature rise θ^*_{cr}, the thermal conductivity K, and the statistical roughness parameters η, β and σ_s.

The change of these parameters with regard to a reference case will be presented in F/v diagrams. The same reference case as described in the previous chapters is used, see Table 3.1, Table 3.2 and Table 4.3, in which a line contact situation is covered and in which body 1 is stationary and body 2 is moving. For the critical temperature a value of 150ºC is used for the reference case i.e. a typical value for the critical temperature for mineral oils that is found by several investigators, see [31]. For the inlet temperature θ_j, a room temperature value of 25ºC is assumed.

A critical temperature rise θ^*_{cr} can be defined, combining Eq. (5.2) and Eq. (5.4), according to

$$\theta^*_{cr} \equiv \theta_{cr} - \theta_j = \theta_{sr} + \left(\theta_{f,i}\right)_{\max} . \tag{5.5}$$

This leads to a critical temperature rise θ^*_{cr} of 125ºC for the reference case. Furthermore, for the reference case the coefficient of friction μ is kept constant at a value equal to the boundary lubrication value $\mu = \mu_C = 0.15$.

5.3.1 Influence of Radius

Considering the relation for the total asperity contact temperature, Eq. (4.20), the reduced radius R' of the macro contact has an influence on the a_x, a_y and $K_{eff}(a_x)$ in term θ_{sr}. Furthermore, R' influences the resulting separation h from the iterative process as described in Section 3.5.3 and thus changes the values for F_i, $a_{x,i}$ and $a_{y,i}$ in term $\theta_{f,i}$. In Figure 5.4, the effect of varying the reduced radius R' is shown for values, next to the reference case where R' equals 2 mm, of respectively 1, 10 and 100 mm. It can be observed that with increasing radius, the transition (for θ^*_{cr} = 125ºC) shifts to the right and enhances the load carrying capacity largely.

The effect of the reduced radius on the transition can be quantified by Eq. (5.6), resulting from curve fitting. According to this equation, F can be written as a function of v and R' (with coefficient of determination: $r^2 = 0.9992$).

$$\ln F = F(v) + a_1 \ln R' \quad \text{with} \quad a_1 = 0.34796847 \;\rightarrow\; a_1 \approx 0.35. \tag{5.6}$$

Rearranging Eq. (5.6) gives

$$\ln\left(\frac{F}{R'^{a_1}}\right) = F(v)\,. \tag{5.7}$$

5.3.2 Influence of Elasticity Modulus

Similar to the effect of the reduced radius R' on the transition, the reduced elasticity modulus E' also influences a_x, a_y and $K_{eff}(a_x)$ in the macroscopic term θ_{sr} and F_i, $a_{x,i}$ and $a_{y,i}$ in the microscopic term $\theta_{f,i}$. The results of calculations with different elasticity moduli are shown in Figure 5.5, in which next to the reference value of E' = 231 GPa, E' of 50, 100 and 300 GPa are evaluated. It is shown that the load carrying capacity is increasing with decreasing E'. For instance at v = 1 m/s the maximum allowable load increases from 300 to 800 N for E' decreasing from 300 to 50 GPa.

Curve fitting ($r^2 = 0.9952$) with regard to $F = F(v,E')$ gives

$$\ln F = F(v) - a_2 \ln E' \quad \text{with} \quad a_2 = 0.50632267 \;\rightarrow\; a_2 \approx 0.51 \tag{5.8}$$

and thus

$$\ln\left(FE'^{a_2}\right) = F(v)\,. \tag{5.9}$$

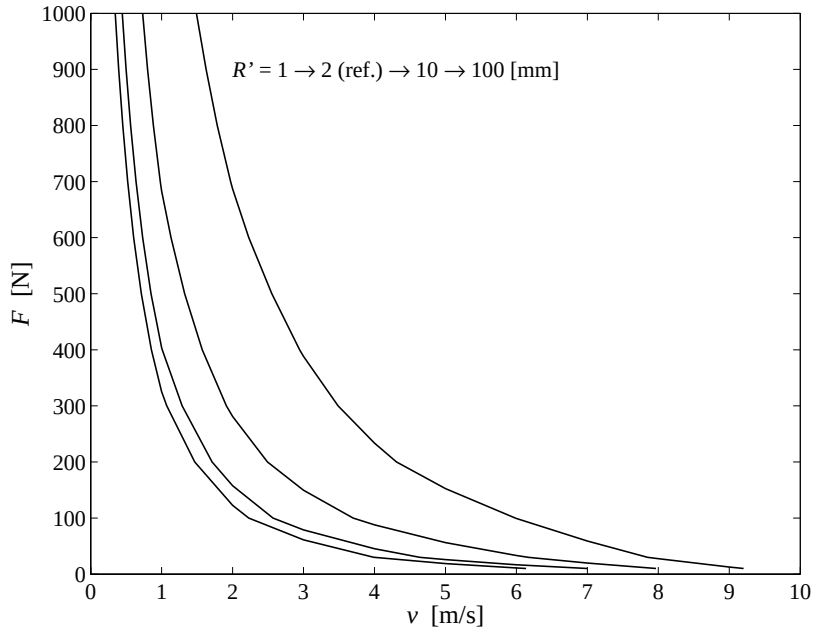

Figure 5.4 Effect of the reduced radius *R'* on the *F*/*v* transition diagram for the reference critical temperature rise θ^*_{cr} of 125ºC.

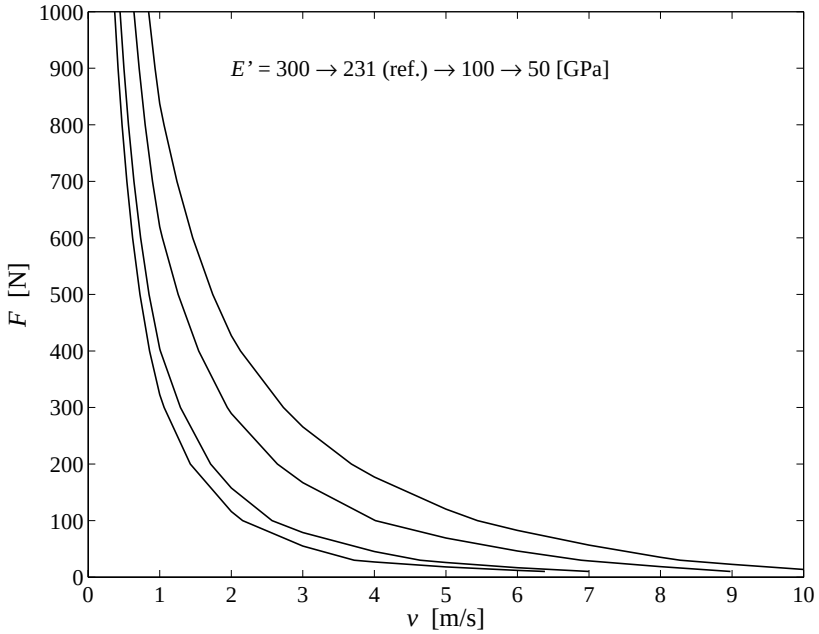

Figure 5.5 Effect of the reduced elasticity modulus *E'* on the *F*/*v* transition diagram for the reference critical temperature rise θ^*_{cr} of 125ºC.

5.3.3 Influence of Contact Length

The length of the line contact ℓ also influences θ_{sr} and $\theta_{f,i}$ and is similar to the effects of R' and E'. In Figure 5.6 ℓ is varied with values of 1, 10 and 100 mm, next to the reference case in which a value of 3.4 mm is used for ℓ. Again curve fitting (r^2 = 0.9992) with regard to $F = F(v, \ell)$ yields

$$\ln F = F(v) + a_3 \ln \ell \quad \text{with} \quad a_3 = 0.96963365 \;\rightarrow\; a_3 \approx 0.97 \tag{5.10}$$

and

$$\ln\left(\frac{F}{\ell^{a_3}}\right) = F(v)\,. \tag{5.11}$$

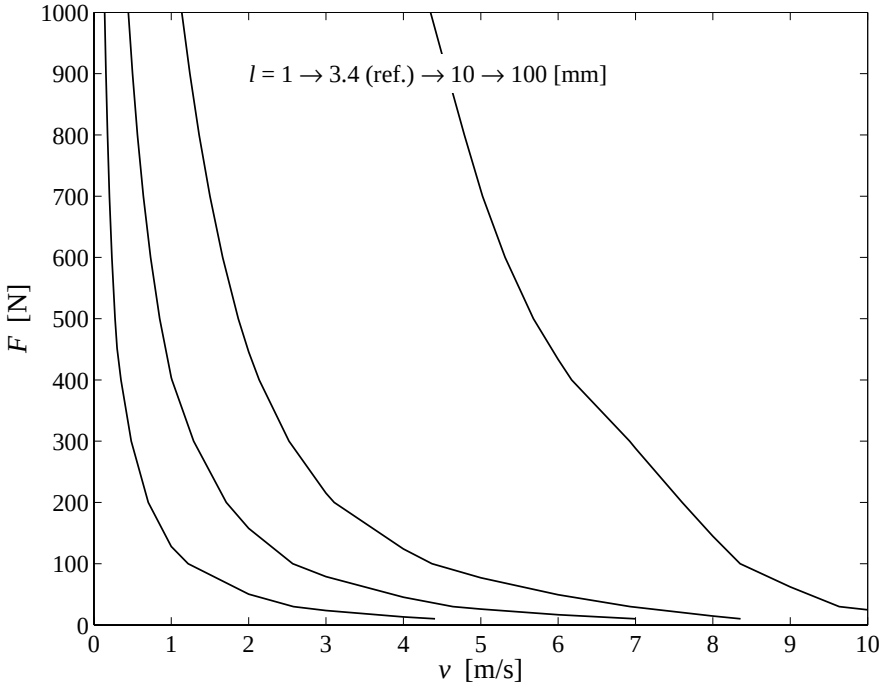

Figure 5.6 Effect of the contact length ℓ on the F/v transition diagram for the reference critical temperature rise θ^*_{cr} of 125ºC.

5.3.4 Influence of Hardness

The hardness H does not appear in the term for θ_{sr} and therefore only affects $\theta_{f,i}$. In Figure 5.7 H is varied with values of 5, 10 and 15 GPa, next to the reference case in which a value of 6.6 GPa is used for H. It is shown that the change in hardness value, hardly affects the transition curves. This is also reflected in the curve fit (r^2 = 0.9964) according to

$$\ln F = F(v) - a_4 \ln H \quad \text{with} \quad a_4 = 0.072912622 \;\rightarrow\; a_4 \approx 0.07 \tag{5.12}$$

and

$$\ln\left(FH^{a_4}\right) = F(v)\,, \tag{5.13}$$

where the low value of the fit parameter a_4 indicates a small effect on the transition curve.

The hardness value is limiting the maximum occurring pressure in the, now plastically deforming, micro contacts as discussed in Section 3.4. Subsequently, this leads to lower forces per micro contact as is shown in Figure 3.7. In Figure 5.7 the dashed line indicates the case in which plasticity is not taken into account in the model ($H \rightarrow \infty$). It can clearly be seen that in that case the load carrying capacity is largely underestimated and it can be concluded that plasticity should be taken into account in the model.

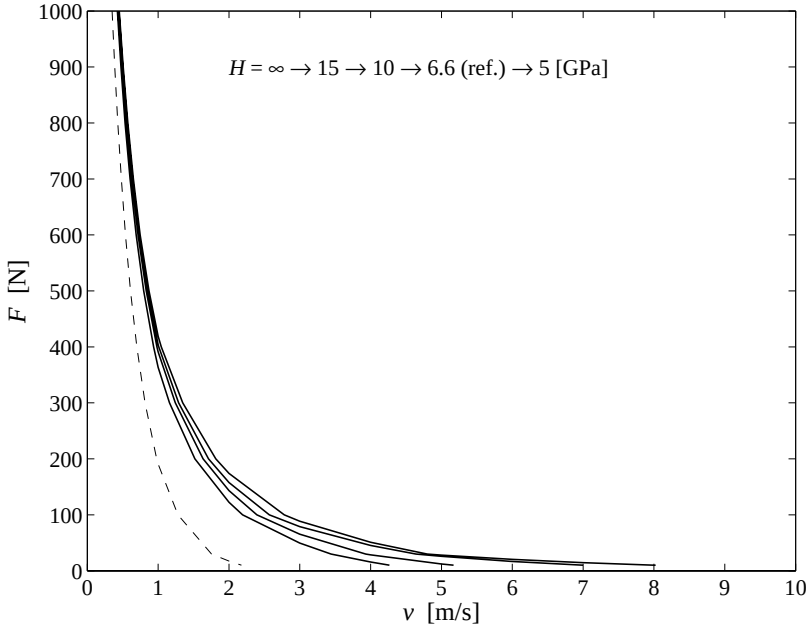

Figure 5.7 Effect of the hardness H on the F/v transition diagram for the reference critical temperature rise θ^*_{cr} of 125ºC.

5.3.5 Influence of Critical Temperature Rise

Another parameter that is varied, is the critical temperature rise θ_{cr}^{*}. In the reference case 125ºC is assumed for θ_{cr}^{*}. Next to this value, the transition diagram is calculated for several critical temperature rise values as already shown in Figure 5.3.

It can be seen that with increasing critical temperatures, the transition curves shift considerably to the right, meaning a large increase of the load carrying capacity. This is also reflected in the following curve fit ($r^2 = 0.9981$)

$$\ln v = v(F) + b_3 \ln \theta_{cr}^{*} \quad \text{with} \quad b_3 = 1.2084151 \rightarrow b_3 \approx 1.21. \tag{5.14}$$

This leads to

$$\ln\left(\frac{v}{\left(\theta_{cr}^{*}\right)^{b_3}} \right) = v(F)\,. \tag{5.15}$$

5.3.6 Influence of Thermal Conductivity

In this section, the influence to the transition diagram of different thermal conductivity values for both K_1 and K_2 is discussed. The influence of the thermal conductivity of the stationary body K_1 is shown in Figure 5.8. The following curve fit ($r^2 = 0.9985$) can be made:

$$\ln v = v(F) + b_5 \ln K_1 \quad \text{with} \quad b_5 = 0.38429594 \rightarrow b_5 \approx 0.38. \tag{5.16}$$

This leads to

$$\ln\left(\frac{v}{K_1^{b_5}} \right) = v(F)\,. \tag{5.17}$$

The influence of the thermal conductivity of the moving body K_2 is presented in Figure 5.9.

It can be seen that when comparing the effects of K_1 vs. K_2, the change in K_2 has a larger influence on the transition diagram. This is due to the fact that the dimensionless temperature number for the moving body ($\bar{\theta}_2$) is much smaller than for the stationary body ($\bar{\theta}_1$), see Eq. (4.10) and for instance Table 4.3. According to Eq. (4.8), this leads to a relatively larger K_{eff} when increasing K_2 compared to increasing K_1. This is also reflected in the fit parameter b_6 (larger than b_5) that follows from curve fitting ($r^2 = 0.9985$) with regard to K_2:

$$\ln v = v(F) + b_6 \ln K_2 \quad \text{with} \quad b_6 = 0.47269206 \rightarrow b_6 \approx 0.47 \tag{5.18}$$

and

$$\ln\left(\frac{v}{K_2^{b_6}} \right) = v(F)\,. \tag{5.19}$$

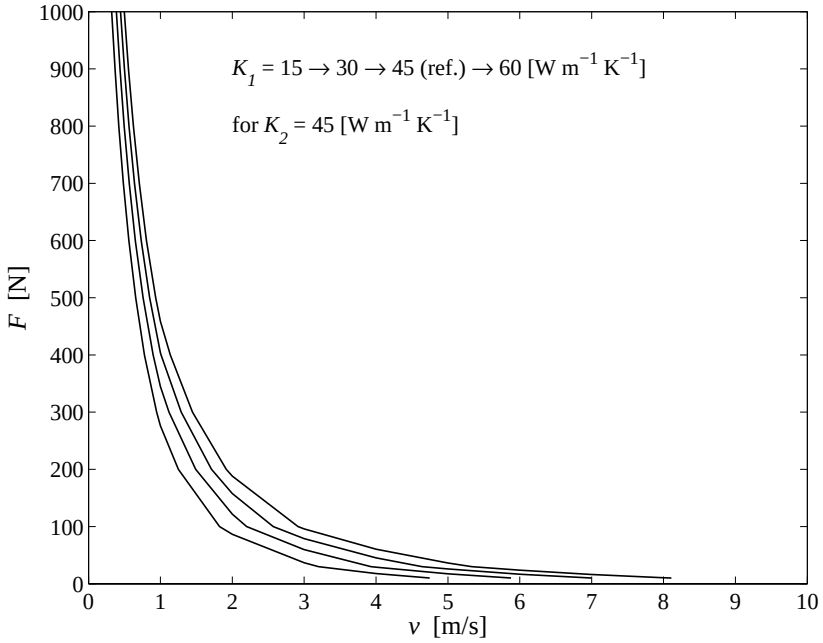

Figure 5.8 Effect of the thermal conductivity of the stationary body K_1 on the F/v transition diagram for the reference critical temperature rise θ^*_{cr} of 125ºC.

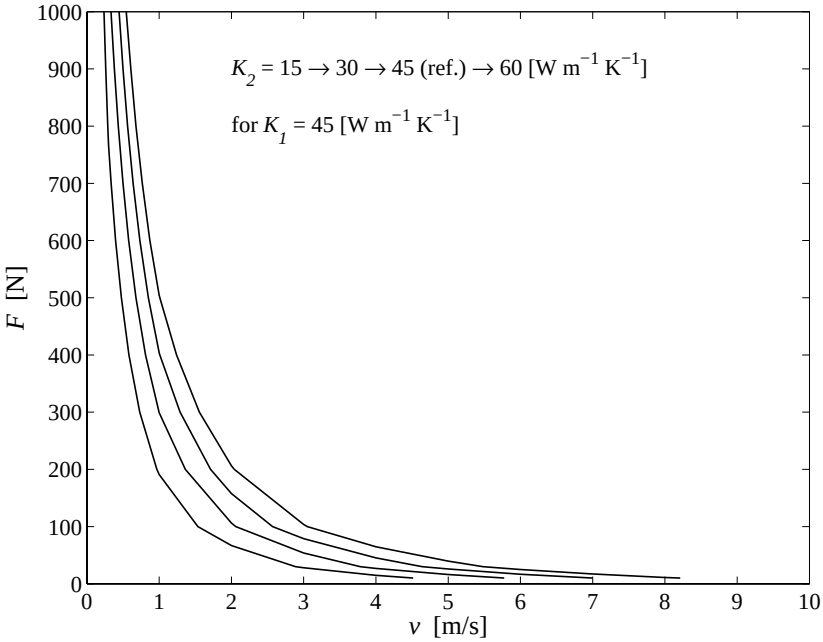

Figure 5.9 Effect of the thermal conductivity of the moving body K_2 on the F/v transition diagram for the reference critical temperature rise θ^*_{cr} of 125ºC.

5.3.7 Influence of Roughness

In order to see the influence of the roughness on the transition diagram, the three main statistical roughness parameters will be varied i.e. density of asperities η, the mean radius of asperities β and the standard deviation of the summit heights σ_s.

Transition diagram calculations are made for variations of each roughness parameter with respect to its reference case value. The results for variations of the standard deviation of the summit heights σ_s are presented in Figure 5.10. It can be seen that the load carrying capacity decreases for higher σ_s values. It should be noted that these calculations are made for boundary lubrication conditions in which a constant coefficient of friction μ is assumed. An additional effect of σ_s is to be expected in the mixed lubrication regime when varying μ which is a function of σ_s (see next section and for instance [25]). Curve fitting ($r^2 = 0.9946$) gives

$$\ln v = v(F) - b_7 \ln \sigma_s \quad \text{with} \quad b_7 = 0.25285498 \rightarrow \; b_7 \approx 0.25, \tag{5.20}$$

and

$$\ln\left(v \sigma_s^{b_7}\right) = v(F)\,. \tag{5.21}$$

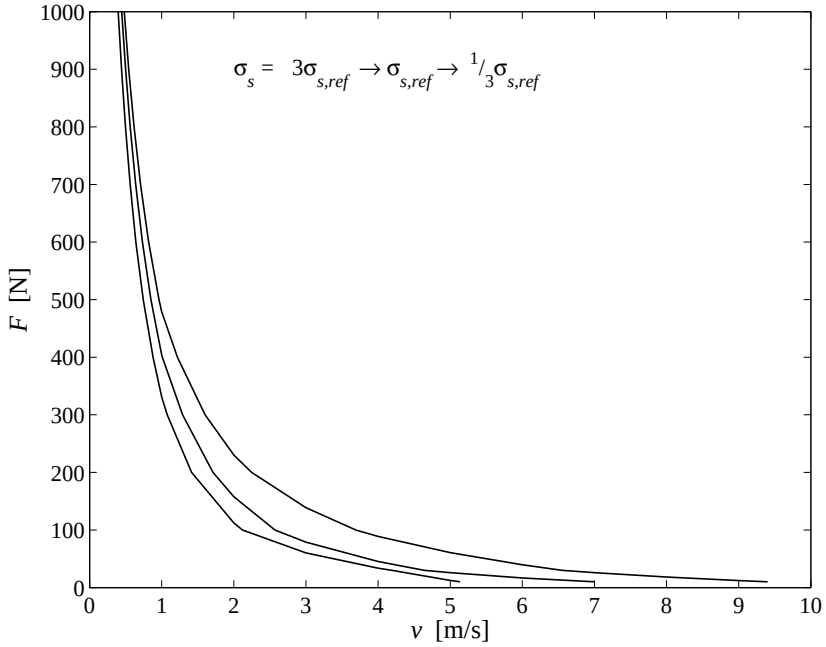

Figure 5.10 Effect of the standard deviation of the summit heights σ_s on the F/v transition diagram for the reference critical temperature rise θ^*_{cr} of 125ºC.

From Figure 5.11 it can be concluded that a change in the mean summit radius β value is nearly unaffecting the transition, which means that the load carrying capacity is hardly changing with varying β. It can be assumed that

$$v = v(F, \beta) \approx v(F) \tag{5.22}$$

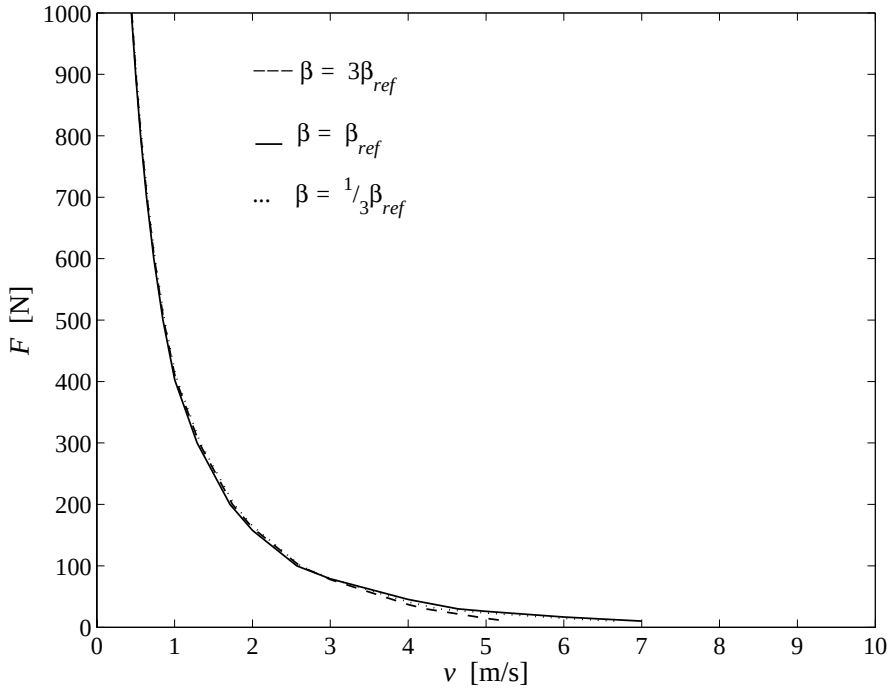

Figure 5.11 Effect of the mean summit radius β on the F/v transition diagram for the reference critical temperature rise θ^*_{cr} of 125ºC.

In Figure 5.12 the effect on the transition of varying the densitity of asperities η is presented. It can be seen that for a higher number of asperities per area, the load carrying capacity is increasing. This is primarily due to the fact that the total load F is carried by a larger number of asperities, which lowers the load per asperity F_i and subsequently lowers the $\theta_{f,i}$ term. Curve fitting ($r^2 = 0.9935$) gives

$$\ln v = v(F) + b_8 \ln \eta \quad \text{with} \quad b_8 = 0.19575722 \;\rightarrow\; b_8 \approx 0.2 \tag{5.23}$$

and

$$\ln\left(\frac{v}{\eta^{b_8}}\right) = v(F)\,. \tag{5.24}$$

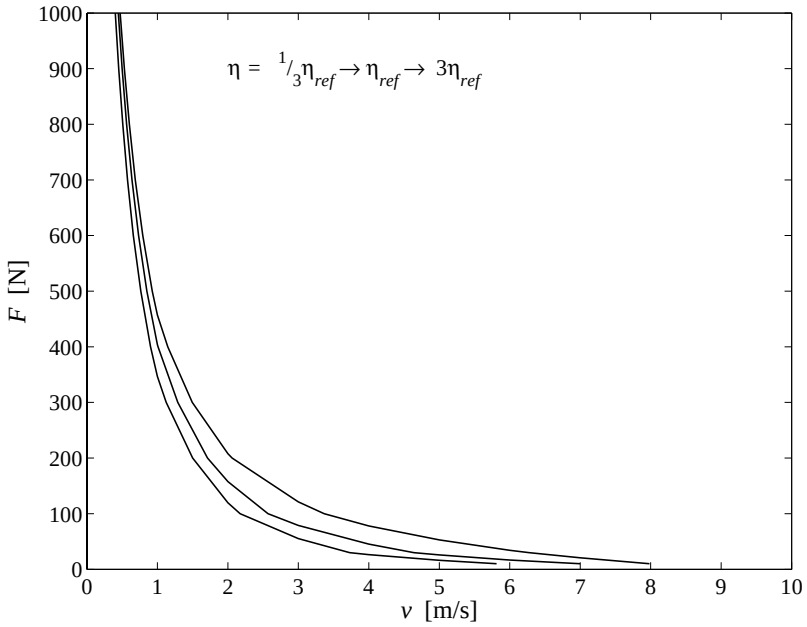

Figure 5.12 Effect of asperity density η on the F/v transition diagram for the reference critical temperature rise θ^*_{cr} of 125ºC.

5.3.8 Influence of Coefficient of Friction

Two sets of calculations are made with regard to the coefficient of friction μ:

1. $\mu = \mu_C$ = constant; only valid for contacts operating under boundary lubrication (BL) conditions.
2. $\mu \neq \mu_C$ and $\mu \neq$ constant; not limited to BL situations and also valid for ML conditions.

For the first set of calculations, $\mu = \mu_C = 0.15$ = constant is taken for the reference case. Furthermore, the $\mu = \mu_C$ is varied with values of 0.05, 0.10 and 0.20. The results are shown in the transition diagram of Figure 5.13. An increase in μ is directly influencing contributions of θ_{sr} and $\theta_{f,i}$ through $\mu = \mu$ and $\mu_C = \mu$ respectively. As expected, an increase in μ is lowering the load carrying capacity and thus shifting the transition curve to the left. Curve fitting ($r^2 = 0.9961$) gives the following relation

$$\ln v = v(F) - b_1 \ln \mu_C \quad \text{with} \quad b_1 = 1.2421478 \;\rightarrow\; b_1 \approx 1.24 \tag{5.25}$$

and

$$\ln\left(v\mu_C^{b_1}\right) = v(F)\,. \tag{5.26}$$

This clearly indicates the big influence of the coefficient of friction on the transition.

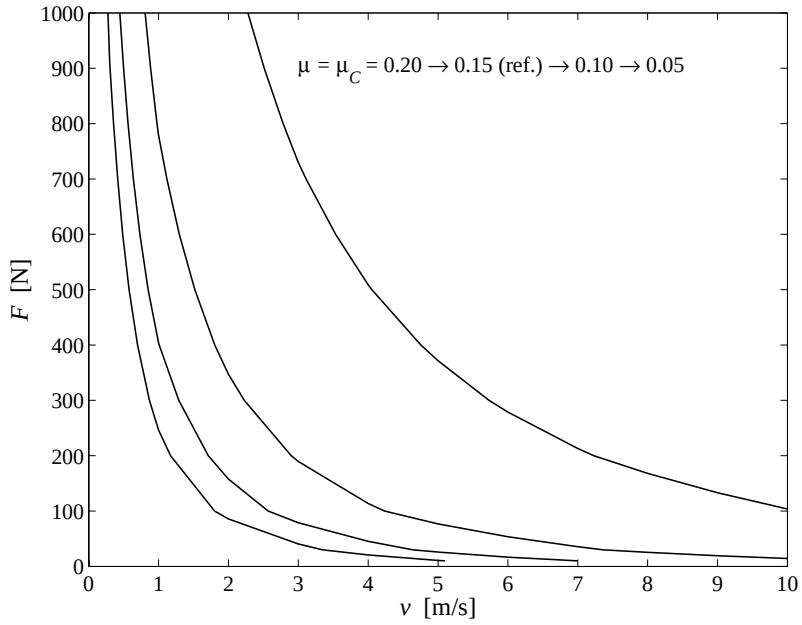

Figure 5.13 Effect of constant coefficient of friction with the value of μ_C on the *F*/*v* transition diagram for the reference critical temperature rise θ^*_{cr} of 125ºC.

A second set of calculations is made for a situation in which the coefficient of friction is not constant. It would be ideal to incorporate Stribeck curve behaviour, but this is very difficult for a separate single parameter. This is due to the fact that μ itself depends on several parameters including F and v (see [20], [25] and [50]). Therefore a different approach is taken in this thesis: for a certain μ_C, variations are made to the actual μ (for instance 0.05) and keeping μ_C constant (for instance 0.15) for variations in F and v. Then, for a certain (available and not constant) μ and for certain other operational conditions it is possible to determine the transition point instead of transition line for each value of μ. This is shown in Figure 5.13. Curve fitting is now possible with regard to the additional parameter μ, next to μ_C

$$\ln v = v(F) - b_2 \ln \mu \quad \text{with} \quad b_2 = 0.39214817 \;\rightarrow\; b_2 \approx 0.39 \tag{5.27}$$

and

$$\ln\left(v\mu^{b_2}\right) = v(F)\,. \tag{5.28}$$

The accuracy of this curve fit is rather low, regarding a coefficient of determination $r^2 = 0.9748$, and therefore it is decided to search for a better prediction. This is found in the form of $\ln F = F(v) - c \ln \mu$. For the following curve fit an r^2 of 0.9998 is found

$$\ln F = F(v) - a_5 \ln \mu \quad \text{with} \quad a_5 = 1.2912684 \;\rightarrow\; a_5 \approx 1.29 \tag{5.29}$$

and

$$\ln\left(F\mu^{a_5}\right) = F(v)\ . \tag{5.30}$$

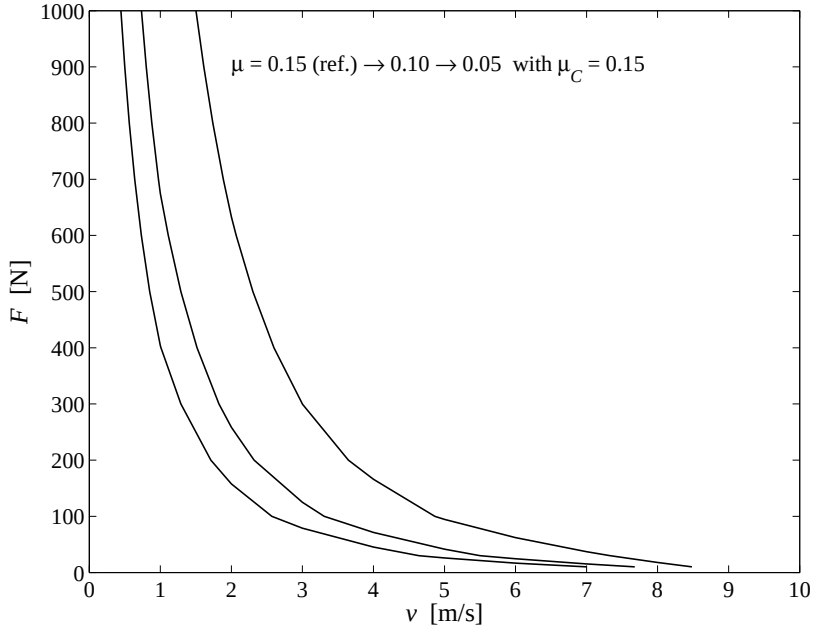

Figure 5.14 Effect of constant coefficient of friction with the value of μ with μ_C = 0.15 (ref.) on the F/v transition diagram for the reference critical temperature rise θ^*_{cr} of 125ºC.

5.4 COMBINED TRANSITION DIAGRAM

The analysis of the separate factors of influence from the previous sections is used to construct one overall transition diagram incorporating all these factors. This is done by an adaptation of F and v into an F^* and v^* parameter. For the F^* parameter the following expression can be written

$$F^* = F \cdot \frac{\mu^{a_5} E'^{a_2} H^{a_4}}{R'^{a_1} \ell^{a_3}} \approx F \cdot \frac{\mu^{1.29} E'^{0.50} H^{0.07}}{R'^{0.35} \ell^{0.97}} \tag{5.31}$$

and for the v^* parameter can be written

$$v^* = v \cdot \frac{\mu_C^{b_1}}{K_1^{b_5} K_2^{b_6} \left(\theta_{cr} - \theta_j\right)^{b_3}} \cdot \frac{\sigma_s^{b_7}}{\eta^{b_8}} \approx v \cdot \frac{\mu_C^{1.24}}{K_1^{0.38} K_2^{0.47} \left(\theta_{cr} - \theta_j\right)^{1.21}} \cdot \frac{\sigma_s^{0.25}}{\eta^{0.20}} \tag{5.32}$$

It should be noted that cross relations between the separate factors of influence are not taken into account in this engineering approach. In Figure 5.15 the combined transition diagram is presented based on the new F^* and v^* parameters on a linear scale. In Figure 5.16 the combined transition diagram is shown on a logarithmic scale.

Furthermore, this diagram can be used to find the total contact temperature $(\theta_{c,i})_{max}$ for a certain contact situation. The value for $(\theta_{c,i})_{max}$ follows from the value of the critical temperature θ_{cr} which is obtained by fitting the data point to the transition line, see Eq. (5.4).

The relation $F^*(v^*)$ can be expressed as

$$F^* = c_1 + c_2 (v^*)^2 + c_3 (v^*)^{-1} \tag{5.33}$$

where $c_1 = -4.763 \cdot 10^{10}$, $c_2 = 9.747 \cdot 10^{25}$ and $c_3 = 468.56$ ($r^2 = 0.9994$).

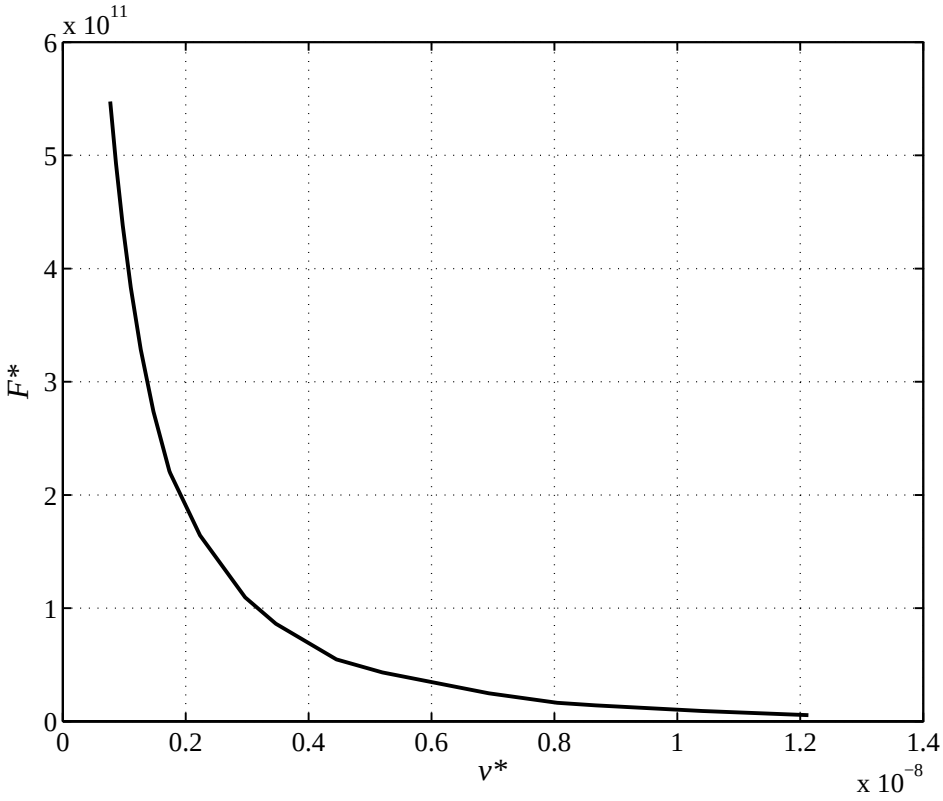

Figure 5.15 Combined transition diagram on linear scale as a result of combining the factors of influence into the new F^* and v^* parameters.

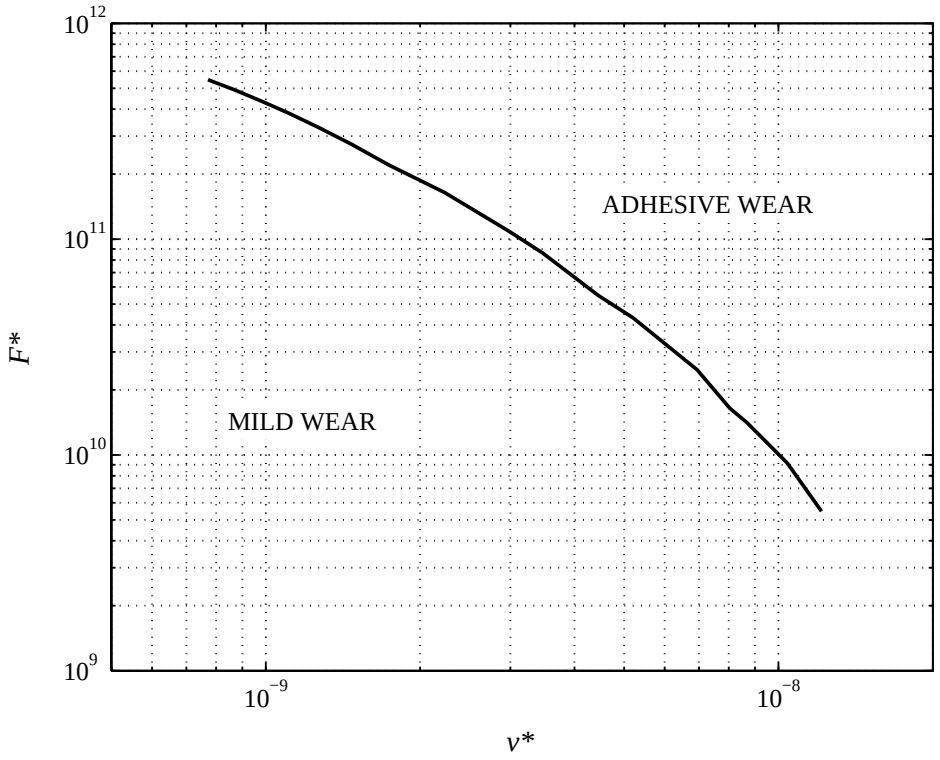

Figure 5.16 Combined transition diagram on logarithmic scale as a result of combining the factors of influence into the new F^* and v^* parameters.

5.5 CONCLUSIONS AND SUMMARY

In this chapter an F/v diagram with iso-thermal curves for θ_{sr}, $\theta_{f,i}$ and θ_{cr}^* is modelled, based on the deformation and contact temperature models developed in the previous chapters. For a reference critical contact temperature rise $\theta_{cr}^* = \theta_{cr} - \theta_j$ of 125ºC a parameter study is carried out in order to determine the influence on the transition of the parameters: radius, elasticity modulus, contact length, hardness, critical temperature rise, thermal conductivity, roughness and coefficient of friction. Accurate curve fits ($r^2 > 0.99$) are obtained with regard to the influence of each parameter on the transition in the transition diagram. The contribution of each parameter is combined in the form of an adaptation of F and v in an F^* and v^* parameter. Finally, an overall combined transition diagram is established with F^* and v^* parameters incorporating the factors of influence.

Chapter 6

Tribological Test Methods

6.1 INTRODUCTION

In the previous chapters, a calculation model has been developed in order to predict the transition from mild to adhesive wear for the lubricated contact situation of for instance a smooth cylinder sliding against a rough flat surface. According to Blok's failure hypothesis (see Eq. (2.8)), the transition takes place when the total asperity contact temperature θ_c reaches a certain critical value θ_{cr}.

Now two items have to be verified experimentally. Firstly, it has to be demonstrated that the transition from I/II to III* or III takes place at a constant value for θ_c for all operating conditions. This means that for the measured failure diagram the transition from I/II to III* or III equals an iso-temperature line i.e. θ_{cr}. Secondly, this θ_{cr} needs to be determined for different oils under investigation. This will be done by means of a high temperature tribotester by increasing the inlet oil temperature at negligible frictional heat (i.e. low load and velocity) in order to determine for which value of the temperature, the contact fails i.e. has no protective boundary layer present anymore. This value is an indication for θ_{cr}.

For the first item, i.e. the measurement of the failure diagram, a new tribological test device is developed in order to handle a large range of load and velocity settings. The new test device is a pin-on-disk type tribotester and is able to represent the cylinder-disk configuration in which a stationary cylinder is loaded against a rotating disk in order to facilitate the sliding motion. The friction force and normal force are measured independently in order to enable accurate measurements. The development and performance of this new test rig is presented in Section 6.2. From now on this rig will be called the high load pin-on-disk tribotester.

For the second item, i.e. the increase of the inlet oil temperature to determine θ_{cr}, a commercially avialable pin-on-disk type tribotester is used, which is able to handle very high temperatures. A description can be found in Section 6.3. This tester will be denoted as the high temperature pin-on-disk tribotester from now on.

6.2 DEVELOPMENT AND PERFORMANCE OF THE HIGH LOAD PIN-ON-DISK TRIBOTESTER

6.2.1 Configuration

For the experimental evaluation of the cylinder-disk tribological contact situation four main parameters are distinguished which also have to be reflected in the pin-on-disk configuration, i.e.

1. normal force F
2. friction force F_f
3. sliding velocity v
4. oil inlet temperature θ_j

These parameters have to be applied in a controllable and precise way and also need to be accurately measured. The important parameter, the coefficient of friction μ can be derived from the normal and friction force signals according to Eq. (1.1). In Figure 6.1 the new pin-on-disk test device is shown in which the four main units are indicated (A, B, C and D).

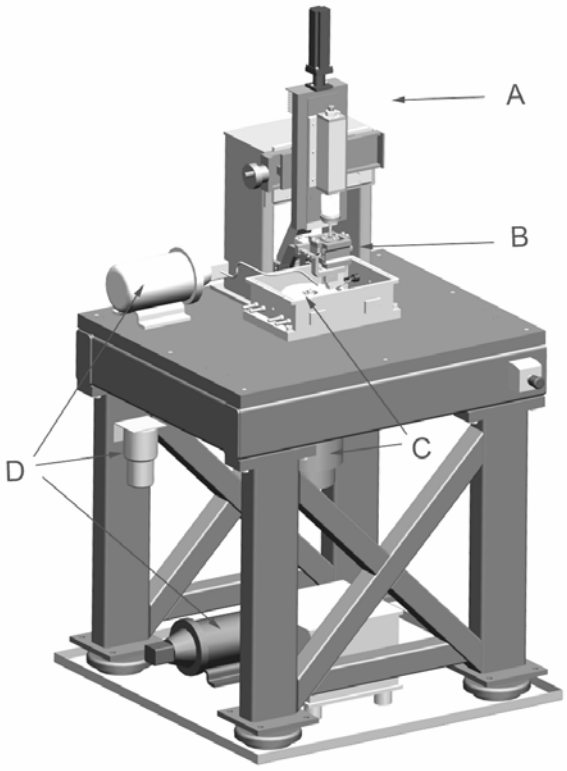

Figure 6.1 High load pin-on-disk tribotester configuration.

These four main units consist of:

A. motor and spindle unit for normal force actuation and measurement
B. friction measurement unit
C. motor and disk unit to impose the sliding velocity
D. lubrication and heating unit to ensure the oil supply at a certain temperature

Below, details are presented of the way each of the four important parameters is treated in the test device.

Normal Force

For the normal force actuation, a force is applied to the pin by means of a spindle (1), which is driven by a servomotor (2) as shown in Figure 6.2. The spindle converts a rotational speed into a translation in z or normal direction. A guiding system (3) is attached to the spindle, on which a shaft (4) with a bush (5), exerts a force through a coupling (7), a normal force transducer (8), a friction measurement unit (9) and a bracket (10) to the pin holder. The pin holder holds a cylinder in this case.

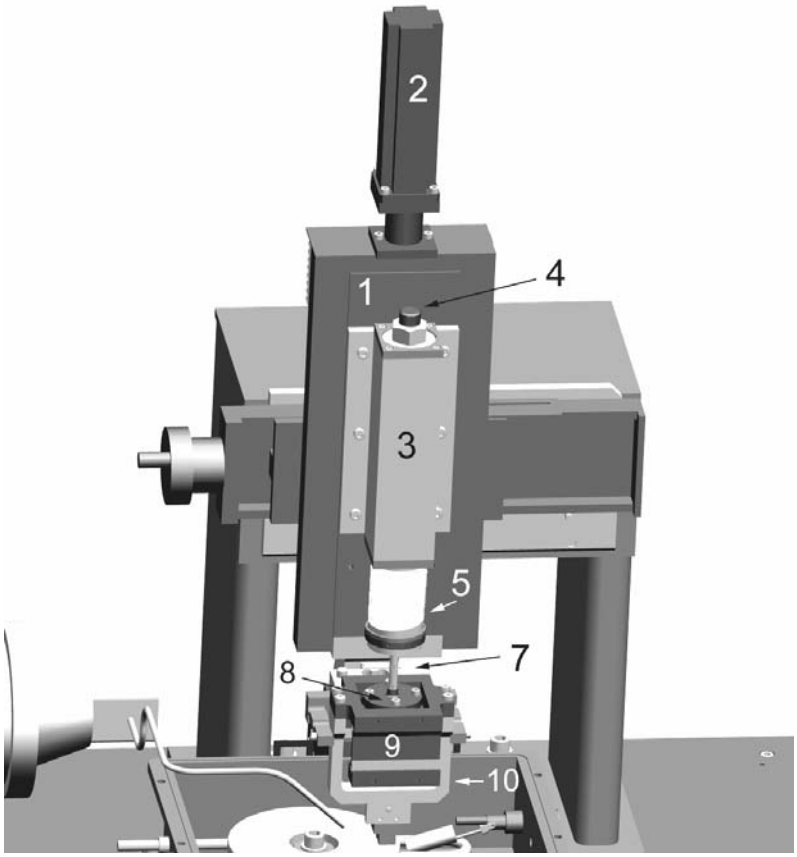

Figure 6.2 Normal force actuation and measurement.

Furthermore, it can be seen that the normal force is applied exactly in line from the shaft to the pin-disk contact, which eliminates extra moments in the system. The elastic joints of the friction force measurement unit (9) are subjected to tensile forces. The friction force measurement unit is further discussed in the next section.

Measurement of the Friction Force

For the measurement of the friction force in a pin-on-disk tribotester, often the torque T of the disk motor is measured, taking into account the frictional torque T at a certain running radius R_r according to $F_f = T/R_r$. Unfortunately, also disproportional contributions from other than the frictional pin-disk contact to the torque and friction force appear, e.g. bearings. In order to measure the friction force more accurately, a special unit is developed, which is schematically presented in Figure 6.3.

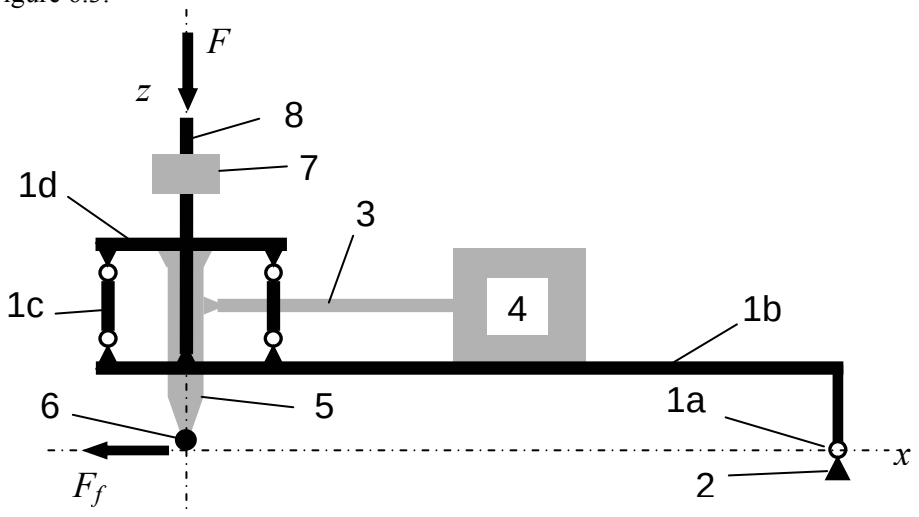

Figure 6.3 Friction force measurement unit.

The aim of this friction force measurement unit is to measure the friction force and at the same time transfer the normal force independently. The lever mechanism (1) is attached to the spindle (2) which is fixed to the frame and the lever is able to pivot around the cross elastic joints (1a). In order to avoid moments, the pivot point is located exactly in the plane of the pin-disk contact and in the direction of the friction in this contact. The bracket (5) is mounted to the lever arm at (1d) and the elastic joint set-up (1c) ensures a degree of freedom in x direction. Arm (3) is attached to the load cell (4) preventing displacement of this bracket (5) in the x direction. This load cell measures the friction force in the pin-disk contact. The normal load is applied to arm (8) by a spindle and measured by the load cell (7).

Disk Rotation

A servomotor enables the rotational speed of the disk, which leads to the pin-disk sliding velocity in combination with a stationary pin.

Oil Supply and Heating

Oil lubrication of the pin-disk contact is ensured in two ways. The first is that the disk is fully emersed with oil in an oil bath. From an oil reservoir, oil is transported via a pump to the oil bath in which the oil is heated by means of heater elements and the oil is thermostatically controlled. The second way is an extra oil supply through a nozzle to enable a fully flooded situation also at high rotational/slip speeds, in cases when centrifugal forces prevent sufficient oil supply to the contact zone. A second pump transfers the heated oil from the oil bath to the nozzle, which ensures oil flow directly into the contact.

The oil is filtered at two places in the oil circuit. The first filter unit is placed in between the oil reservoir and the oil bath when the oil is conveyed towards the oil bath. The second filter unit is placed in the oil reservoir itself and the oil is filtered when the oil is pumped back from the oil bath into the oil reservoir.

6.2.2 High Load Tribotester: Specifications and Performance

In Table 6.1 an overview is given of the specifications of the developed high load pin-on-disk tribotester.

Table 6.1 High load pin-on-disk specifications (F.S.: full scale).

property	symbol	range	precision
normal force	F	50 – 1000 N	0.2% F.S. – 2 N
friction force	F_f	0 – 500 N	0.05% F.S. – 0.025 N
sliding velocity	v	0.01 – 22 m/s	0.05% F.S. – 0.01 m/s
oil temperature	θ_j	θ_{room} – 140ºC	1ºC

Test experiments were carried out for the validation of the newly developed tribotester. These experiments consist of Stribeck curve measurements, in which the coefficient of friction μ is plotted as a function of the velocity v; see also Figure 1.3. In Figure 6.4, examples of the test measurements are shown. This figure demonstrates excellent reproducibility of the tests. The measurements were performed at a constant load of 200 N, viscosity of 7 mPa.s, combined initial CLA roughness of pin and disk of 0.2 μm, and for a large range of sliding velocities: from 0.025 up to 5 m/s and back. Before these Stribeck curve measurements were carried out, running-in was established by applying a normal load of 500 N for one hour at 0.1 m/s first and then for one hour at 1 m/s.

The first series of measurements resulted in the Stribeck curve marked (●) for increasing sliding velocity. The second series, marked (▼), was measured with decreasing velocity and the third series, marked (■), was measured again for increasing sliding velocity.

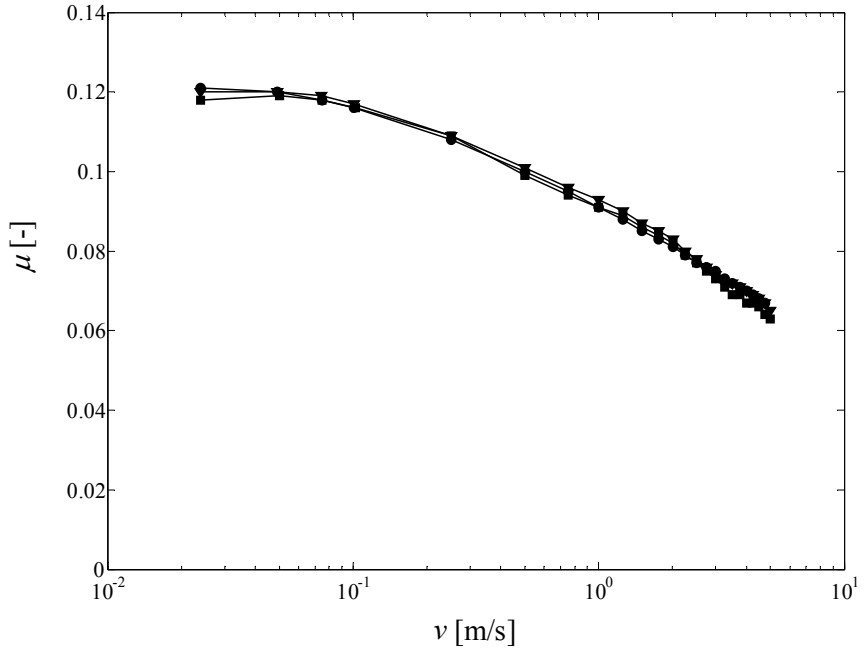

Figure 6.4 Three Stribeck curves measured with the high load pin-on-disk tribotester, F = 200 N and θ_j = 100ºC.

6.3 HIGH TEMPERATURE PIN-ON-DISK TRIBOTESTER

For the determination of the critical temperature θ_{cr}, a commercially available pin-on-disk tribotester is used. This test rig is developed by CSEM, Switzerland. The set-up of this apparatus is shown in Figure 6.5. The pin (1) is put onto the disk (2) by a dead weight (3). In order to avoid alignment problems, a ball is used as the pin. The ball is mounted in a ball holder which is attached rigidly to an elastic joint unit (4), of which the degree of freedom in the direction of the friction force is used to measure this force by means of a displacement transducer (not shown). The specifications of this test rig are presented in Table 6.2. For more information about this apparatus, the reader is referred to [20], [47] and [48].

Table 6.2 CSEM high temperature pin-on-disk tribotester specifications.

property	symbol	range
normal force	F	1 – 20 N
friction force	F_f	0 – 20 N
sliding velocity	v	0.005 – 5 m/s
oil temperature	θ_j	θ_{room} – 800ºC

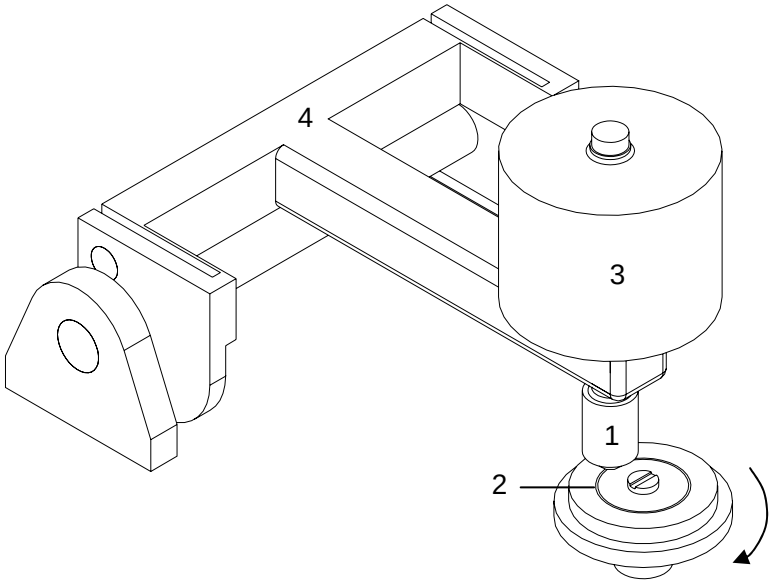

Figure 6.5 CSEM high temperature pin-on-disk tribotester.

6.4 CONCLUSIONS AND SUMMARY

In order to validate the model for predicting the load carrying capacity of lubricated contacts as described in Chapter 5, two types of measurements have to be performed. The first is to determine the transition as a function of a range of operating conditions and structural parameters. For this purpose a custum-built high load pin-on-disk tribotester is developed, of which the configuration and main features are described in Section 6.2. It is shown that good reproducibility during friction measurements is achieved. The second type of measurement that needs to be carried out, is a test to determine the critical temperature for the oils under investigation. For this purpose, a commercially available high temperature pin-on-disk tribotester (CSEM) is used as is briefly discussed in Section 6.3. In Chapter 7 the verification of the model with the experimental results is presented.

Chapter 7

Transition Diagram Model Validation with Experimental Results

7.1 INTRODUCTION

In Chapter 5 a model for the prediction of the transition diagram is discussed. This model is based on the hypothesis that the transition to adhesive wear occurs when the total local contact temperature exceeds a critical temperature of the boundary layer created by the lubricant and the surface. Therefore, two types of experiments are needed to verify the transition diagram model, i.e.

1. Measurements to determine the transition diagram as a function of operating conditions and structural parameters.
2. Measurements to determine the critical temperature of the lubricants under investigation.

For the first type of measurements, a high load tribotester is developed. For the second type a commercial high temperature tribotester is available. Both tribotesters are described in Chapter 6.

In the next section, the materials used in the experiments are discussed. In Section 7.3 the experimental procedures are described. The measurement results are presented in Section 7.4 and in Section 7.5, the transition diagram model from Chapter 5 is verified with these experimental results. Finally, conclusions are drawn in Section 7.7.

7.2 MATERIALS

In this section a brief overview of the materials used in the experiments is given. For the transition diagram measurements with the high load pin-on-disk tribotester, the following materials for the pin and disk are used:

- Pin: Commercially available cylinder bearing rollers of low alloyed chromium steel with a diameter of 4 mm, nominal length of 4 mm and effective contact length due to round edges of 3.4 mm. The surface finish processes applied are grinding and polishing.
- Disk: The disk of diameter 150 mm is made of case hardening steel. The surface finish process applied is grinding.

For the measurements to determine the critical temperature with the high temperature pin-on-disk tribotester, the following materials for pin and disk are used:

- Pin: Commercially available austenitic stainless steel (grade 316) balls with a diameter of 10 mm. Surface finish process: grinding and polishing.
- Disk: The disk of diameter 40 mm is made of austenitic stainless steel, grade 316. The surface is machined by turning and then polished.

The experiments have been performed under lubricating conditions. Two commercially available oils are evaluated, denoted as oil A and oil B. Oil A is highly doped heavy duty oil, whereas oil B is highly refined, light duty mineral white oil. Viscosity and density values of these oils are presented in Table 7.1.

Table 7.1 Oil density and viscosity specifications.

Oil	density ρ_d [kg/m^3]	kinematic viscosity ν_k [mm^2/s]		dynamic viscosity η_0 [mPa.s]	
	θ = 25ºC	θ = 40ºC	θ = 100ºC	θ = 40ºC	θ = 100ºC
A – Commercial	862	40	9	35	7
B – Shell Ondina 32	866	32	5	28	4

7.3 EXPERIMENTAL PROCEDURES

7.3.1 Transition Diagram Procedure

Before the start of an actual transition measurement, the samples were cleaned with acetone and the roughness was measured with the 3D interference microscope. The transition to adhesive wear was determined according to the traditional procedure A (see Section 2.2.3) on the high load pin-on-disk tribotester. No running-in procedure was employed, so every time new specimens were used for several combinations of normal load F and velocity v.

After heating up the pin, disk and the lubricant to the selected temperature, the velocity was increased to the required value and the normal force was applied fast, usually in one to four seconds depending on the value of the normal force. In a time interval of two minutes it was determined if adhesive wear took place or not. After two minutes, first the load and then the velocity was lowered to zero. For the case in which adhesive wear occurred, it was accompanied by a lot of noise. It was decided

that the rig should be stopped after the first sign of adhesive wear to avoid damage to the cylinder holder. During a measurement the normal force F, velocity v, inlet temperature θ_j and friction force F_f was accurately monitored with a sample frequency of 100 Hz.

7.3.2 Critical Temperature Procedure

A procedure to determine the critical temperature is described in detail by Grew and Cameron [31]. They analysed scuffing behaviour of mineral oils and related scuffing to desorption of surface active agents (surfactants) at a certain critical/transition temperature. Next to (physical) adsorption/desorption, also chemical adsorption or even chemical reaction may occur (see Section 1.3.2.1).

Grew and Cameron state in their paper that in a lubricated concentrated contact, in case the total contact temperature is composed of a steady state contact temperature and a flash temperature, the flash temperatures are of very short duration. So short (μs to ms) that the oil (surfactant) desorps before it is able to react.

In order to develop a suitable test to determine the critical temperature for mineral oils, the temperature must be increased under conditions of negligible frictional heat and in which desorption takes place without being masked by chemisorption. Grew and Cameron concluded that materials (pin/disk) should be used that are unreactive, thus preventing chemisorption. They used austenitic stainless steel for this purpose, which are used in this investigation as well.

Before an actual measurement is carried out, the pin and disk are thoroughly cleaned with acetone and heated up to the required temperature level. Then oil is added and in a short time the temperature of the oil is accomodated to the pin and disk temperature monitored by a thermocouple. Next, the actual measurement is carried out: first, the velocity v is set to 0.065 m/s and then the load F of 10 N is applied. Attention is paid to the friction signal within one revolution (about two seconds). If the friction rises sharply within this first revolution ($\mu > 0.4$), it can be concluded that the critical temperature is reached.

Besides mineral oils (oil B), highly doped oils with extreme pressure (EP) additives and friction modifiers are evalutated as well (oil A). Now, a more complex situation arises: EP additives are designed to reach the surface and form a chemisorbed layer to protect the surfaces from scuffing. Unfortunately, the method above is not capable of determining the critical temperature for these oils, because the temperatures in which the EP additives loose their working capacity are exceeding the flame point of the (base) oil.

7.4 EXPERIMENTAL RESULTS

7.4.1 Transition Diagram Results

In order to validate the model, three transition diagrams are obtained i.e. for oil A at room temperature and at 100ºC, and for oil B at room temperature (25ºC). The traditional procedure A (see Section 2.2.3) is applied, so no running-in procedure is employed.

A representative example of a measurement in which no adhesive wear occurs is shown in Figure 7.1 for oil B at room temperature. It can be seen that the normal force F of 400 N is applied shortly after the velocity v is set to 1.5 m/s. Furthermore, the coefficient of friction μ is sharply increasing with increasing normal load. From the moment the required normal force level is reached, μ is first a bit unstable before it reaches a more stable level. An example of a cylinder after a test in which no adhesive wear occurs is presented in Figure 7.4a.

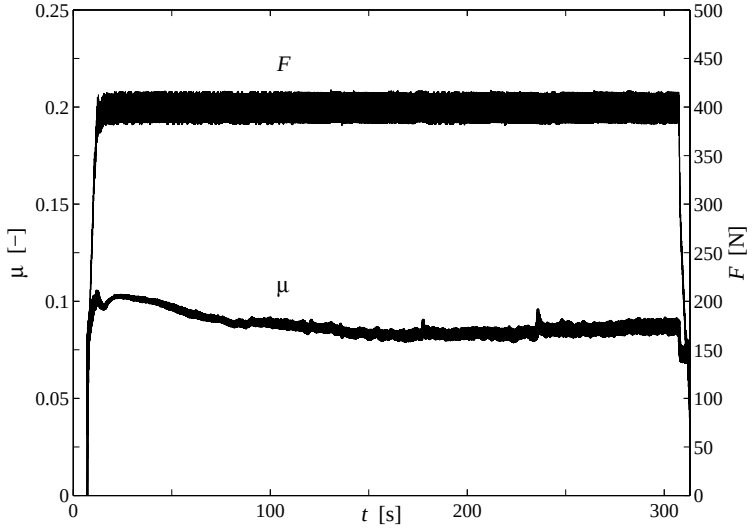

Figure 7.1 Measurement according to procedure A for oil B – typical measurement in which no adhesive wear occurs (F = 400 N and v = 1.5 m/s).

In Figure 7.2 an example is shown in which the contact almost immediately fails after the total load is applied ($\mu \rightarrow 0.4$). It can be seen that it takes about four seconds to reach the load of 600 N. Two stages can be distinguished for the coefficient of friction μ. During the first stage, the accurately monitored coefficient of friction μ increases sharply. Then, during the second stage, μ still increases but more slowly, due to thermal effects. It should be noted that it was not possible to apply the normal force faster, due to non-infinite system stiffness.

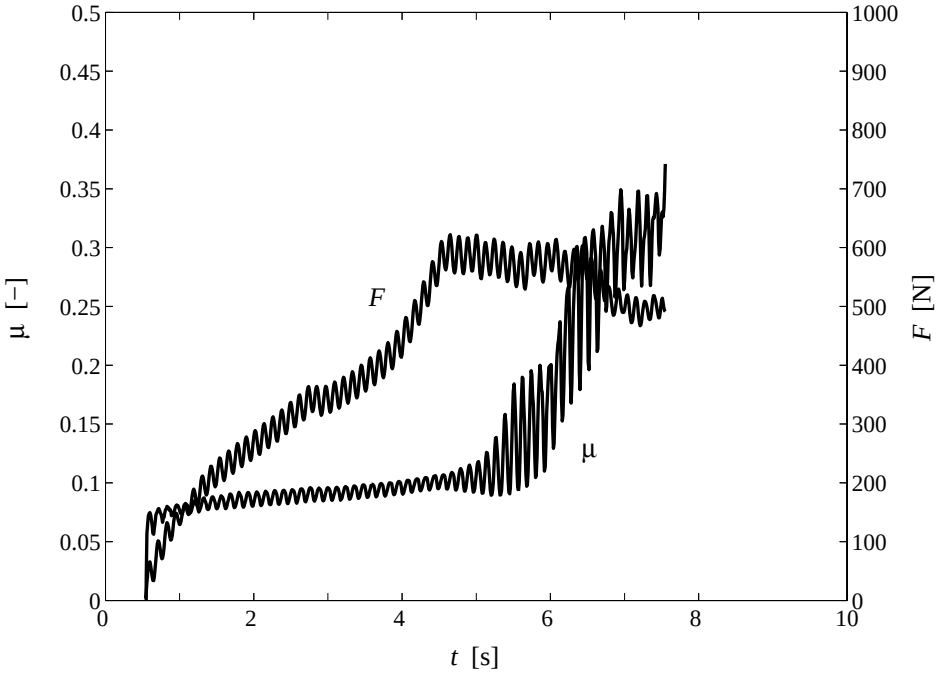

Figure 7.2 Measurement according to procedure A for oil B – measurement in which adhesive wear occurs almost immediately after the load is fully applied (F = 600 N and v = 1.5 m/s).

A measurement was stopped when a lot of noise was detected. Usually, the coefficient of friction μ reaches values of 0.35 to 0.4. In all those cases, material inspection showed severe adhesive wear, see Figure 7.4b, indicating a clear transition from I/II to III. It must be noted that the transition I/II to III* was not found at these velocities.

Furthermore, in Figure 7.5 an interferometry image is presented of adhesive wear in the track on the disk. A lot of material is transferred from the cylinder to the disk, demonstrated by maximum surface heights of about 40 μm, whereas normal roughness values are of the order of 0.1 μm. More adhesive wear regions can be identified in one single wear track, indicating the adhesive wear originating from roughness spot(s).

In Figure 7.3, an example is given of a situation in which the contact fails due to adhesive wear ($\mu \rightarrow 0.4$), not immediately but after a certain period. Up to this moment the coefficient of friction μ slowly increases, again due to thermal effects.

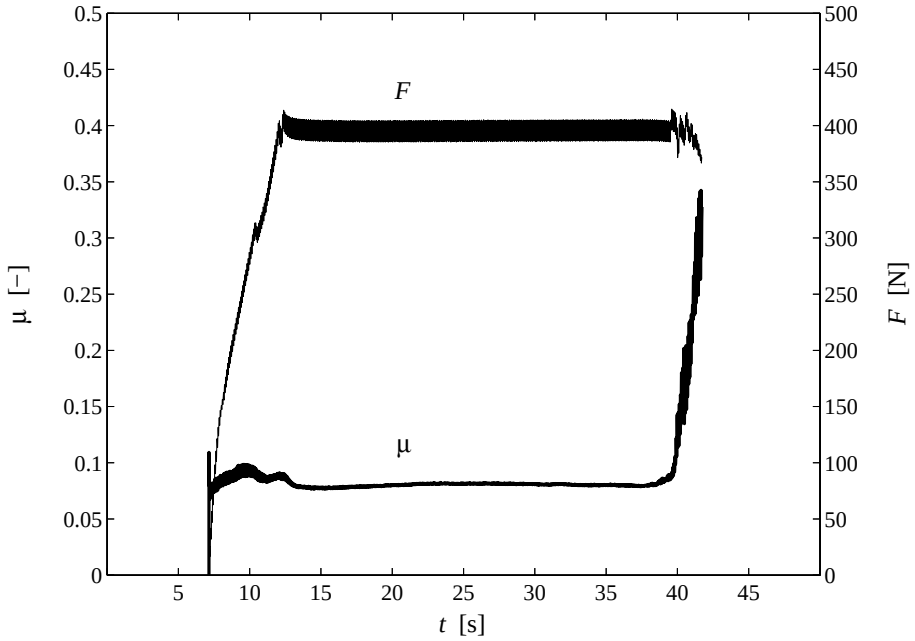

Figure 7.3 Measurement according to procedure A for oil B – measurement in which adhesive wear occurs a few seconds after the load is fully applied (F = 400 N and v = 2.5 m/s).

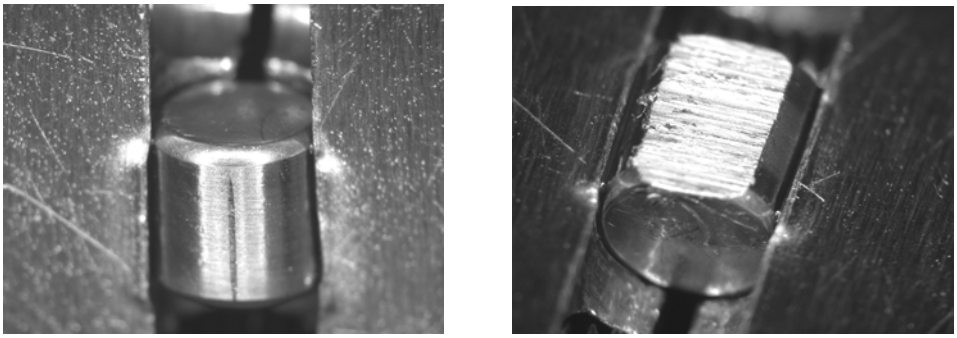

(a) (b)

Figure 7.4 Microscopic images of cylinder after test: (a) no adhesive wear observed (b) severe adhesive wear observed.

In Figure 7.6 the resulting transitions from mild to adhesive wear are shown for both oils A and B. As expected, the load carrying capacity of oil A at room temperature (25ºC) is much larger than at 100ºC. Furthermore, it can be seen that the load carrying capacity of the highly doped oil A at 100ºC is almost the same as for the mineral oil B at 25ºC, clearly indicating the positive influence of additives on the adhesive wear transition. Details are presented in Table 7.2 and Table 7.3.

Figure 7.5 Interferometry image of the disk after a test in which severe adhesive wear tracks are observed (height scale min-max: 40 µm).

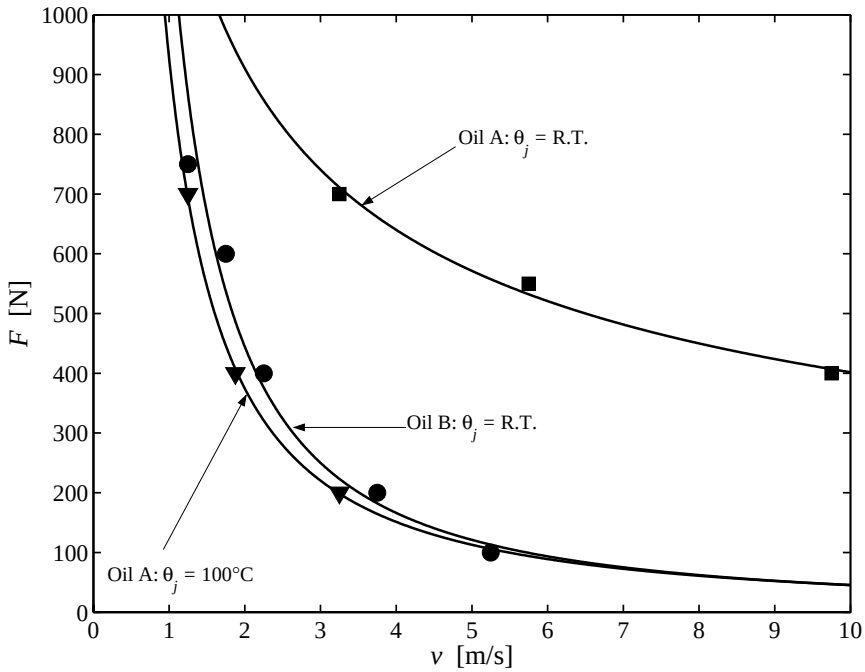

Figure 7.6 Measured mild to severe adhesive wear transitions for oils A and B.

7.4.2 Critical Temperature Results

For the mineral white oil (oil B), the critical temperature is determined according to the procedure described in Section 7.3.2. The temperature is increased in steps of about 20ºC (for every time step new materials are used) and the coefficient of friction μ within the first revolution is accurately monitored. Results are presented in Figure 7.7. It can be seen that for a temperature of 130ºC, the coefficient of friction μ peaks to large values.

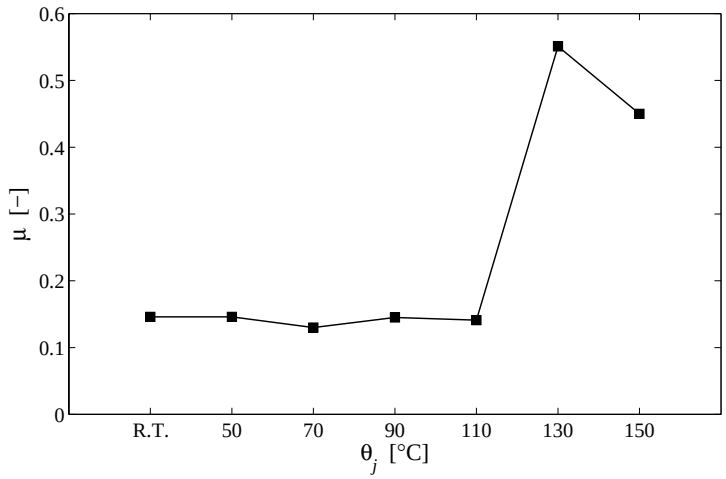

Figure 7.7 Coefficient of friction μ as a function of the inlet temperature θ_j for oil B (R.T.: room temperature), measured with the high temperature pin-on-disk tribotester.

7.5 MODEL VALIDATION

The results from the transition diagram and critical temperature measurements from the previous sections are used to validate the transition diagram model. Two steps are distinguished. The first is to calculate the total temperature at the transition for a certain oil and find out if the transition is represented by a single value. The second step is to compare this value with the measured critical temperature. This is only possible for oil B, as explained in Section 7.3.2. The possible resulting constant temperature can be taken as the critical temperature for oil A.

All the input values for the model are based on the values as used for the reference case throughout this thesis. Only information about the coefficient of friction, both the μ_C and the actual occurring μ, is not available yet. The coefficient of friction in the boundary regime μ_C for oil A is estimated to be 0.145 based on the critical temperature measurements from Section 7.4.2. For oil B, a value of 0.12 is used for μ_C as shown in Figure 6.4. For the actual occurring coefficient of friction μ, the measured value is taken just before the sharp increase of μ to high values. Values are presented in Table 7.2 for oil B and in Table 7.3 for oil A.

Furthermore, from these values, the course of μ in time and in visual inspection, it can be concluded that running-in is already present within the first few seconds of loading in a way that it causes a deviation in the nominal contacting area as modelled in Chapter 3, in which no running-in is taken into account. Therefore, a correction in the calculations is needed to incorporate the initial wear during loading.

In order to determine the resulting contact width of the line contact, the measurement is used at the same load and at a velocity just before the adhesive wear occurs. It is assumed that this value is an indication for the contact width of the situation in which adhesive wear occurs. This value, b_{meas}, is compared with the modelled $b_{RoughLine}$ (see Appendix A). Now an equivalent radius R_{eq} can be defined as the radius through which in the model $b_{RoughLine}$ becomes b_{meas}. This is calculated, together with the ratio $\xi = R_{eq}/R$. Now, the total contact temperature $(\theta_{c,i})_{\max}$ can be calculated. Values are presented in Table 7.2 and Table 7.3. Furthermore, the total contact temperature $(\theta_{c,i})_{\max}$ is calculated for the average value of ξ: $\xi_{av} = 8$.

For the mineral white oil B, the calculated temperatures are rather constant with an average value of 135ºC for both cases (where ξ or ξ_{av} is used) and have values close to the temperature for which adhesive wear occurs for the first time in the critical temperature measurements: 130ºC. It can be concluded that here good agreement is found between model and measurement.

For the highly doped oil A the calculated temperatures deviate a bit more from a single value. Minimum to maximum values are 206.9 to 272.0ºC and 208.4 to 257.7ºC for ξ and ξ_{av} respectively. The average values are 230ºC and 237ºC for ξ and ξ_{av} respectively.

The transition points can be expressed in terms of F^* and v^*. They can be presented in the combined transition diagram as discussed in Section 5.4 (Figure 5.15). The results are shown in Figure 7.8 for $\xi_{av} = 8$ and in Figure 7.9 for the actual ξ. It can be seen that for oil B, the resulting F^* and v^* combinations lie close to the transition line for a θ_{cr} of 130ºC as determined in Section 7.4.2 and therefore this transition is well predicted, using the combined transition diagram. For oil A, the average value of 230ºC is chosen as the critical temperature value and inserted in the v^* parameter. Again it is shown that the resulting F^* and v^* combinations lie close to the transition line for a θ_{cr} of 230ºC.

From these results, it can be concluded that the transition diagram as advanced in this thesis, can very well be used as an engineering design tool to predict and avoid the occurrence of adhesive wear.

7.6 BLOK'S CONTACT TEMPERATURE APPROACH

The calculation of the contact temperature according to Blok is discussed in Section 4.1. In contrast to the current approach, in which the flash temperature is calculated based on micro contacts, Blok used a macro contact approach for the flash temperature calculation according to Eq. (4.1). Blok used the value of the inlet temperature θ_i for the quasi-steady contact temperature θ_s. Furthermore, for the flash temperature θ_f two techniques can be employed. The first technique is to use Eq.

(2.9) to calculate θ_f. The resulting total contact temperature will be labelled as $\theta_{c,BlokA}$. The second technique is to apply the method of Bos to calculate a maximum temperature for a macro contact using the $\overline{\theta}^{em}$ numbers from Table 4.1 as discussed in Section 4.2.1. The resulting contact temperature will be denoted as $\theta_{c,BlokB}$.

These two calculation methods are applied to the transition diagram results for oil A and B from Figure 7.6 (for ξ_{av} = 8). The results are shown in Table 7.2 and Table 7.3. It can be seen that the results for $\theta_{c,BlokA}$ are quite similar to the results for $\theta_{c,BlokB}$. However, the contact temperature results largely deviate and are therefore far from constant. From this it must be concluded that Blok's approach cannot be used to calculate the total temperature in the prediction of the transition to adhesive wear.

7.7 CONCLUSIONS

The critical temperature for mineral white oil could be determined based on a measurement method with austenitic stainless steel specimens. At 130ºC and above, adhesive wear occurred.

Transition diagram measurements were succesfully carried out for mineral light duty white oil (B) and highly doped heavy duty oil (A). The load carrying capacity is much larger for the doped oil when compared to the mineral white oil at the same inlet temperature.

In order to model the measured transitions, the input value for the coefficient of friction, the actual occurring μ just before adhesive wear occurred during a measurement, was used. Furthermore, examination of the specimens revealed that initial wear during the first stages of the measurements cannot be neglected and a correction needs to be applied to the modelling. For the increase in contact width, an average equivalent radius R_{eq} is determined, which is about a factor 8 more than the original R value.

The measured transition points for both oil A and B have been evaluated using the transition diagram model. The calculated temperatures of the transitions found with the mineral white oil B are quite constant (around 135ºC) and were close to the value of 130ºC which was found with the critical temperature measurement method. The temperature results for the doped oil A show a bit more deviation from a single value, but it may still be concluded that the calculated temperature is rather constant.

The transition points for oil A and B are expressed in terms of the F^* and v^* parameters and are inserted in the combined F^*/v^* diagram as developed in Chapter 5. It can be seen that these points are very closely located to the transition line. Therefore, this diagram can be used as a tool for designers to predict and avoid adhesive wear.

Furthermore, the existing contact temperature calculation methods from literature (advanced by Blok), in which the contribution of micro contact temperatures is not taken into account, have been used to evaluate the transition diagram results as well. The calculated temperatures based on these methods deviate strongly and therefore these methods cannot be used to predict the transition to adhesive wear.

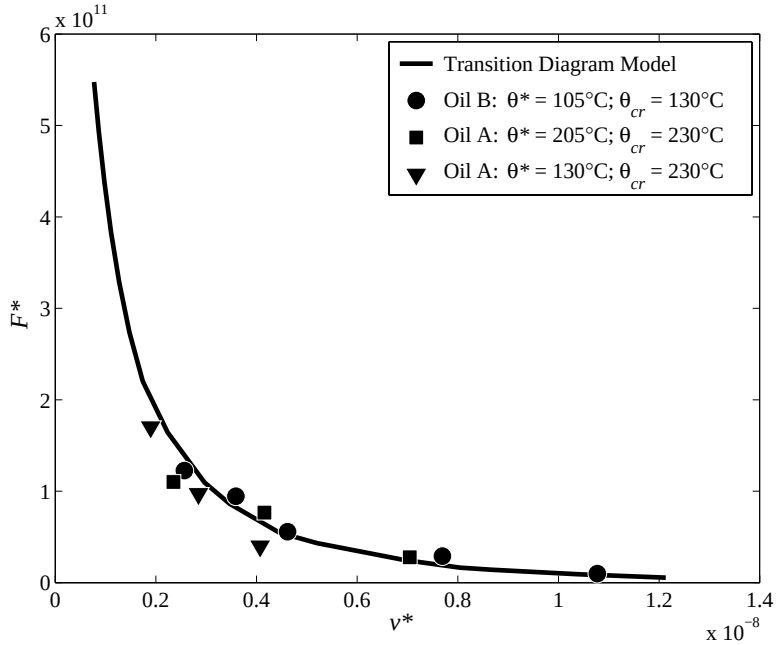

Figure 7.8 Transition diagram measurement results from Figure 7.6 presented in the combined transition diagram (ξ_{av} = 8).

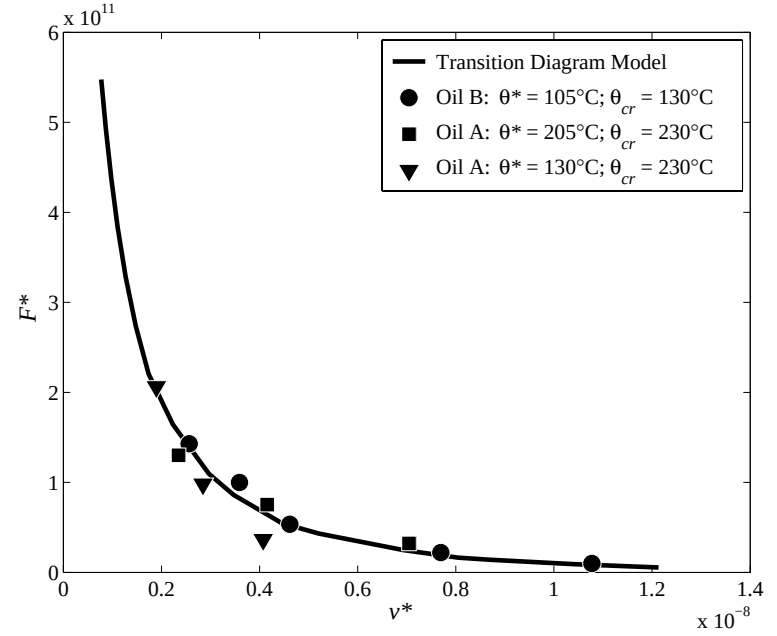

Figure 7.9 Transition diagram measurement results from Figure 7.6 presented in the combined transition diagram (ξ from measurements).

Table 7.2 Transition diagram measurement and modelling results for oil B at room temperature.

		Oil B at θ_j = R.T. = 25 ºC				
F	[N]	750	600	400	200	100
v	[m/s]	1.25	1.75	2.25	3.75	5.25
μ	[-]	0.103	0.100	0.091	0.094	0.070
μ_C	[-]	0.145	0.145	0.145	0.145	0.145
$b_{RoughLine}$	[m]	$7.7\cdot10^{-5}$	$7.0\cdot10^{-5}$	$6.0\cdot10^{-5}$	$4.6\cdot10^{-5}$	$3.7\cdot10^{-5}$
$2b_{meas}$	[µm]	348.6	364.2	354.8	384.0	210.1
R_{eq}	[m]	0.0103	0.0136	0.0180	0.0354	0.0164
ξ	[-]	5.15	6.8	9.0	17.7	8.2
F^*		$1.43\cdot10^{11}$	$9.99\cdot10^{10}$	$5.35\cdot10^{10}$	$2.20\cdot10^{10}$	$9.84\cdot10^{9}$
v^*		$2.56\cdot10^{-9}$	$3.59\cdot10^{-9}$	$4.62\cdot10^{-9}$	$7.69\cdot10^{-9}$	$1.07\cdot10^{-8}$
$(\theta_{c,i})_{max}$	[ºC]	***139.2***	***144.1***	***128.8***	***128.7***	***132.0***
ξ_{av}	[-]	8	8	8	8	8
$R_{eq,av}$	[m]	0.016	0.016	0.016	0.016	0.016
F^*		$1.23\cdot10^{11}$	$9.44\cdot10^{10}$	$5.57\cdot10^{10}$	$2.90\cdot10^{10}$	$9.93\cdot10^{9}$
v^*		$2.56\cdot10^{-9}$	$3.59\cdot10^{-9}$	$4.62\cdot10^{-9}$	$7.69\cdot10^{-9}$	$1.07\cdot10^{-9}$
$(\theta_{c,i})_{max}$	[ºC]	***129.5***	***140.2***	***131.3***	***143.3***	***132.4***
$\theta_{c,BlokA}$	[ºC]	136.2	133.1	107.3	90.2	59.2
$\theta_{c,BlokB}$	[ºC]	146.4	144.1	114.9	94.5	59.5

Table 7.3 Transition diagram measurement and modelling results for oil A at room temperature and 100ºC.

		Oil A at θ_j = R.T. = 25 ºC			Oil A at θ_j = 100 ºC		
F	[N]	700	550	400	700	400	200
v	[m/s]	3.25	5.75	9.75	1.25	1.88	3.25
μ	[-]	0.100	0.091	0.053	0.14	0.14	0.12
μ_C	[-]	0.12	0.12	0.12	0.14*)	0.14*)	0.12
$b_{RoughLine}$	[m]	$7.5\cdot10^{-5}$	$6.8\cdot10^{-5}$	$6.0\cdot10^{-5}$	$7.5\cdot10^{-5}$	$6.0\cdot10^{-5}$	$4.6\cdot10^{-5}$
$2b_{meas}$	[µm]	332.4	390.2	270.3	321.5	333.1	293.7
R_{eq}	[m]	0.0099	0.0168	0.0104	0.0093	0.0156	0.0103
ξ	[-]	5.0	8.4	5.2	4.6	7.8	10.3
F^*		$1.30\cdot10^{11}$	$7.53\cdot10^{10}$	$3.22\cdot10^{10}$	$2.06\cdot10^{11}$	$9.80\cdot10^{10}$	$3.65\cdot10^{10}$
v^*		$2.35\cdot10^{-9}$	$4.16\cdot10^{-9}$	$7.05\cdot10^{-9}$	$1.90\cdot10^{-9}$	$2.85\cdot10^{-9}$	$4.07\cdot10^{-9}$
$(\theta_{c,i})_{max}$	[ºC]	***226.1***	***255.6***	***272.0***	***239.9***	***222.9***	***206.9***
ξ_{av}	[-]	8	8	8	8	8	8
$R_{eq,av}$	[m]	0.016	0.016	0.016	0.016	0.016	0.016
F^*		$1.10\cdot10^{11}$	$7.66\cdot10^{10}$	$2.77\cdot10^{10}$	$1.70\cdot10^{11}$	$9.72\cdot10^{10}$	$3.98\cdot10^{10}$
v^*		$2.35\cdot10^{-9}$	$4.16\cdot10^{-9}$	$7.05\cdot10^{-9}$	$1.90\cdot10^{-9}$	$2.85\cdot10^{-9}$	$4.07\cdot10^{-9}$
$(\theta_{c,i})_{max}$	[ºC]	***208.4***	***257.7***	***252.6***	***225.3***	***222.3***	***212.6***
$\theta_{c,BlokA}$	[ºC]	190.3	192.0	122.3	356.9	215.7	177.5
$\theta_{c,BlokB}$	[ºC]	214.2	218.1	137.5	397.1	225.2	182.1

*) For these cases, μ_C is assumed to be equal to μ i.e. 0.14.

Chapter 8

Conclusions and Recommendations

8.1 CONCLUSIONS

In this section the main conclusions are summarised.

Chapter 1: Introduction

- The transition from mild to adhesive wear in lubricated contacts can lead to scuffing and may result in catastrophic failure of engineering components.

Chapter 2: Transition from Mild to Adhesive Wear

- The *F*/*v* transition diagram can be used to characterise the transition from mild to adhesive wear. In this diagram, three regions are distinguished: I/II (mild wear), III* (adhesive wear on micro scale: incipient adhesive wear) and III (adhesive wear on macro scale: severe adhesive wear).
- The transition to adhesive wear is governed by breaking through the surface protecting layers caused by exceeding a critical contact temperature as hypothesised by Blok. Several attempts to link the modelled contact temperature to Blok's critical temperature hypothesis failed so far.
- Improvement of contact temperature modelling on micro contact level is expected to be the key in predicting the transition to adhesive wear. This idea has been omitted in the models so far.

Chapter 3: Elastic/Plastic Deformation of an Anisotropic Deterministic Rough Contact

- An asperity deformation model, which takes into account deterministic anisotropic surface roughness, is developed. Asperity deformation can be elastic, elastic-plastic or plastic. Mechanical contact characteristics like pressure, force, area and approach can be calculated for every single asperity contact.
- Stribeck curve behaviour is incorporated in the deformation model, taking into account that part of the load is carried by asperities and the remaining part by the (E)HL film.

Chapter 4: Contact Temperature

- A model for the calculation of the total contact temperature has been developed.
- The total local contact temperature rise is assumed to consist of a quasi-steady surface temperature and a flash temperature, based on macro and micro contact properties respectively.

Chapter 5: Transition Diagram Model

- Based on the asperity contact model and the temperature model, F/v diagrams with iso-thermal curves for the quasi-steady surface temperature, flash temperature rise and the resulting total contact temperature are modelled. The iso-thermals are used for the adaptation of Blok's critical temperature hypothesis. The influence of several parameters on the transition to adhesive wear has been determined and combined in the form of a modification of F and v in an F^* and v^* parameter.
- An overall combined (engineering) transition diagram is developed comprising the factors of influence which are investigated.

Chapter 6: Tribological Test Methods

- A high load pin-on-disk tribotester is developed, that is capable of accurately measuring the load carrying capacity of concentrated lubricated contacts.
- A high temperature pin-on-disk tribotester is discussed, which is used to determine the critical temperature of the lubricants under investigation.

Chapter 7: Transition Diagram Model Validation with Experimental Results

- Transition diagram measurements were succesfully carried out for a mineral light duty white oil and a highly doped heavy duty oil. The calculated temperatures of the transitions found for the mineral white oil as well as for the highly doped heavy duty oil are quite constant and equal to the critical temperature.
- The measured transition points to adhesive wear are expressed in terms of the F^* and v^* parameters for both oils and are inserted in the combined F^*/v^* diagram. The measurement points are very closely located to the transition line. Therefore, this diagram can be used as a tool for designers to predict and avoid adhesive wear.
- Furthermore, the existing contact temperature calculation methods from literature (advanced by Blok), in which the contribution of micro contact temperatures is not taken into account, have been evaluated and it is shown that these methods cannot be used to predict the transition to adhesive wear.

8.2 DISCUSSION

The analysis to determine the transition diagram, has so far been focussed on line contacts, which are common in engineering practice, e.g. cam/follower mechanisms and piston/cylinder contacts. Up to now the line contact is assumed to be formed by the deformation of a cylinder with a reduced radius R_x in direction of motion x and a contact length ℓ in y direction. The resulting contact width in x direction $2b$ is much smaller than ℓ, leading to a wide equivalent contact ellipse, as is used for the macro temperature calculations. In this section this situation is compared with a narrow equivalent contact ellipse, obtained by the deformation of a cylinder with reduced radius R_y in y direction and a contact length ℓ in x direction.

Another situation which is common, is the point/circular contact, e.g. ball on flat. This can be seen as an intermediate situation (assuming the same area A), because the determining dimensions a_x and a_y (which are now equal) are in between the line contact dimensions.

In Figure 8.1 these three situations are compared. It is shown that going from a wide to a narrow contact, this leads to a substantial decrease in load carrying capacity. This is only due to the fact that equivalent contact ellipse dimension a_x appears in $\overline{\theta}_2$, leading from a narrow contact to a large macro K_{eff} value resulting in much larger contact temperatures. Futhermore, it can be seen that the transition for the point contact situation is in between the line contact transitions.

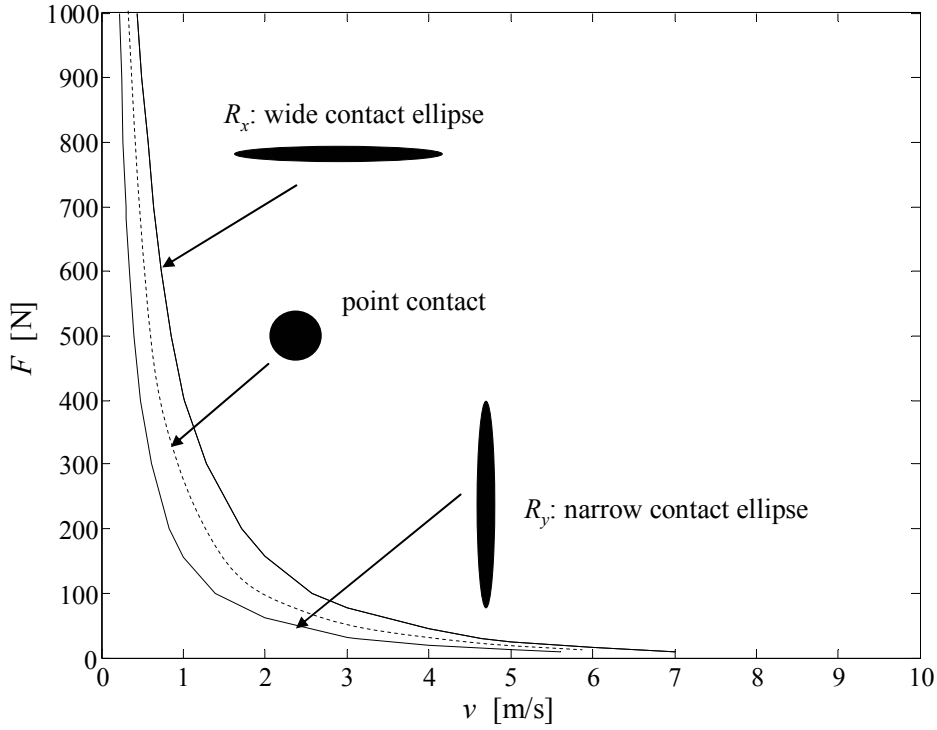

Figure 8.1 Effect of the contact orientation of the line contact on the *F*/*v* transition diagram for the reference critical temperature rise θ^* of 125ºC.

8.3 RECOMMENDATIONS

- Based on the previous section, the engineering F^*/v^* diagram should be adapted in order to incorporate the different elliptical and point contact situations.
- Experiments pointed out that the nominal contact area increases by mild wear. This revealed the need to include a mild wear model in the present transition diagram model.

Appendix

Appendix A

Hertzian Theory with Statistical Roughness for Line Contacts

In Chapter 3, the deformation of rough line contacts is presented. The micro and macro deformations are decoupled. A deterministic approach is taken for the micro contacts. The resulting micro contact characteristics are added to a plan parallel macro contact situation. The macro contact characteristics are considered to be elastic and are given by the Hertz theory for line contacts [36].

Suppose two cylinders with radii $R_{x,1}$ and $R_{x,2}$ are in contact under normal load, then the reduced radius R is given by

$$\frac{1}{R'} = \frac{1}{R_{x,1}} + \frac{1}{R_{x,2}}. \tag{A.1}$$

The reduced Young's Modulus E' can be calculated by

$$\frac{1}{E'} = \frac{1}{2}\left(\frac{1-\nu_1^2}{E_1} + \frac{1-\nu_2^2}{E_2}\right). \tag{A.2}$$

The load per unit length w is defined as

$$w = \frac{F}{\ell}. \tag{A.3}$$

Now, the half Hertzian contact width b can be expressed by

$$b = \left(\frac{8wR'}{\pi E'}\right)^{1/2}. \tag{A.4}$$

The maximum Hertzian pressure p_h is given by

$$p_h = \frac{2w}{\pi b} = \left(\frac{wE'}{2\pi R} \right)^{1/2} \tag{A.5}$$

and the mean Hertzian pressure p_{mean} is

$$p_{mean} = \frac{\pi}{4} p_h \,. \tag{A.6}$$

Gelinck [25] showed that the macro contact properties change significantly by incorporating roughness. He presented accurate close form curve fits for the macro contact characteristics in relation to their Hertzian solutions, using the statistical roughness parameters η, β and σ_s. In Eq. (3.53) the macro contact area is required. Now, according to Gelinck, the contact area for a rough line contact reads

$$A_{RoughLine} = 2 b_{RoughLine} \ell \,, \tag{A.7}$$

where $b_{RoughLine}$ is the half width according to

$$b_{RoughLine} = \left(1 + \left(a_1 \cdot \overline{\eta}^{\,a_2} \cdot \overline{\sigma}_s^{\,a_3} \right)^{a_4} \right)^{1/a_4} \cdot b \,, \tag{A.8}$$

with b the Hertzian half width and

$$\overline{\eta} = 4 \eta b^2 \sqrt{\frac{\beta}{R}} \tag{A.9}$$

and

$$\overline{\sigma}_s = \frac{\sigma_s R}{b^2} \,, \tag{A.10}$$

with a_i

$$a_1 = 1.235 \,,\; a_2 = -0.0345 \,,\; a_3 = 0.439 \;\text{ and }\; a_4 = 1.71 \,. \tag{A.11}$$

References

[1] **Abbott, E.J. and Firestone, F.A.**, (1933), "Specific Surface Quality – A Method Based on Accurate Measurement and Comparison," Mech. Engr., Vol. 55, p. 569.

[2] **Archard, J.F.**, (1959), "The Temperature of Rubbing Surfaces," Wear, Vol. 2, pp. 438-455.

[3] **Begelinger, A. and Gee, A.W.J. de**, (1979), "Thin Film Lubrication of Sliding Point Contacts – Formulation of a 'Collapse Parameter'," Proc. 5th Leeds-Lyon symposium, Leeds 1978, Institution of Mech. Engineers, London, pp. 291-298.

[4] **Begelinger, A. and Gee, A.W.J. de**, (1981), "Failure of Thin Film Lubrication – The Effect of Running-in on the Load Carrying Capacity of Thin Film Lubricated Concentrated Contacts," Journal of Lubrication Technology, Vol. 103, pp. 203-210.

[5] **Bell, J.C., Dyson, A. and Hadley, J.W.**, (1975), "The Effect of Rolling and Sliding Speeds on the Scuffing of Lubricated Steel Discs," ASLE Transactions, Vol. 18, 1, pp. 62-73.

[6] **Bhushan, B.**, (1999), "Principles and Applications of Tribology," Wiley, New York, USA.

[7] **Bjerk, R.**, (1973), "Oxygen – an Extreme-Pressure Agent", ASLE Trans., Vol. 16 (2), pp. 97-106.

[8] **Bos, J.**, (1995), "Frictional Heating of Tribological Contacts," Ph.D. thesis, University of Twente, The Netherlands.

[9] **Blok, H.**, (1937), "Theoretical Study of Temperature Rise at Surface of Actual Contact under Oiliness Lubricating Conditions", Proc. of the General Discussion on Lubrication and Lubricants, Inst. Mech. Engrs, Vol. 2, pp. 222-235.

[10] **Blok, H.**, (1939), "Seizure Delay Method for Determining the Protection Against Scuffing Afforded by Extreme Pressure Lubricants," SAE Journal, Vol. 44, pp. 193-204.

[11] **Carslaw, H.S. and Jaeger, J.C.**, (1959), "Conduction of Heat in Solids," Oxford University Press, Oxford, UK.

[12] **Chou, C.C. and Lin, J.F.**, (2002), "A New Approach to the Effect of EP Additive and Surface Roughness on the Pitting Fatigue of a Line Contact System," ASME Journal of Tribology, Vol. 124, pp. 245-258.

[13] **Cowan, R.S. and Winer, W.O.**, (1994), "Thermomechanical Wear Modelling," Tribotest Journal 1-2, pp. 111-123.

[14] **Cutiongco, E.C. and Chung, Y.-W.**, (1994), "Prediction of Scuffing Failure Based on Competitive Kinetics of Oxide Formation and Removal: Application to Lubricated Sliding of AISI 52100 Steel on Steel," STLE Tribology Transactions, Vol. 37, 3, pp. 622-628.

[15] **Czichos, H. and Kirschke, K.**, (1972), "Investigations into Film Failure (Transition Point) of Lubricated Concentrated Contacts," Wear, Vol. 22, pp. 321-336.

[16] **Czichos, H.**, (1974), "Failure Criteria in Thin Film Lubrication – the Concept of a Failure Surface," Tribology, pp. 14-20.

[17] **Czichos, H.**, (1992), "Presentation of Friction and Wear Data," ASM Handbook, Vol. 18, pp. 489-492.

[18] **DIN 50320**, (1979), "Verschleiß – Begriffe, Systemanalyse von Verschleißvorgängen, Gliederung des Verschleißgebietes, Beuth Verlag, Berlin, Germany.

[19] **Dyson, A.**, (1976), "The Failure of Elastohydrodynamic Lubrication of Circumferentially Ground Discs," Proc. Inst. Mech. Engrs., Vol. 190, No.1, pp. 52-76.

[20] **Faraon, I.C.**, (2005), "Mixed Lubricated Line Contacts", Ph.D. thesis, University of Twente, The Netherlands.

[21] **Francis, H.A.**, (1976), "Phenomenological Analysis of Plastic Spherical Indentation," ASME Journal of Engineering Materials and Technology, Vol. 76, pp. 272-281.

[22] **Gee, A.W.J. de, Begelinger, A. and Solomon, G.**, (1979), "Failure of Thin Film Lubrication; Function Oriented Charaterization of Additives and Steels," ASLE Trans., Vol. 23. No.1, pp.23-34.

[23] **Gee, A.W.J. de and Begelinger, A.**, (1984), "Failure Mechanisms in Sliding Lubricated Concentrated Contacts," Proceedings of the 11th Leeds-Lyon Symposium on Mixed Lubrication and Lubricated Wear, Vol. 2, pp. 105-116.

[24] **Gee, A.W.J. de**, (1996), "Tribotechniek – deel E: Toestandsdiagrammen," Lecture notes, University of Twente, The Netherlands (in Dutch).

[25] **Gelinck, E.R.M.**, (1999), "Mixed Lubrication of Line Contacts," Ph.D. thesis, University of Twente, The Netherlands.

[26] **Godfrey, D.**, (1968), "Boundary Lubrication", in P.M. Ku (Ed.), "Interdisciplinary Approach to Friction and Wear," NASA Sp-181, pp. 335-384.

[27] **Greenwood, J.A.**, (1984), "A Unified Theory of Surface Roughness," Proc. Roy. Soc. Lon., A 393 (1804), pp. 133-157.

[28] **Greenwood, J.A. and Williamson, J.B.P.**, (1966), "Contact of Nominally Flat Surfaces," Phil. Trans. R. Soc. London, Series A295, pp. 300-319.

[29] **Greenwood, J.A. and Tripp, J.H.**, (1967), "The Elastic Contact of Rough Spheres," ASME Journal of Applied Mechanics, Vol. 34, pp. 153-159.

[30] **Greenwood, J.A. and Tripp, J.H.**, (1970), "The Contact of Nominally Flat Rough Surfaces," Proc. Instn. Mech. Engrs., Vol. 185, pp. 625-633.

[31] **Grew, W.J.S. and Cameron, A.**, (1972), "Thermodynamics of Boundary Lubrication and Scuffing," Proc. R. Soc. London, Series A327, pp. 47-59.

[32] **Haar, R. ter**, (1996), "Friction in Sheet Metal Forming – the Influence of (Local) Contact Conditions and Deformation," Ph.D. thesis, University of Twente, The Netherlands.

[33] **Heide, E. van der**, (2002), "Lubricant Failure in Sheet Metal Forming Processes," Ph.D. thesis, University of Twente, The Netherlands.

[34] **Heijningen, G.J.J. van and Beek, A. van**, (1993), "Tribotechniek; Deel B: Dunne film theorie," Lecture Notes, TU Delft, The Netherlands (in Dutch).

[35] **Hershberger, J., Ajayi, O.O., Zhang, J., Yoon, H. and Fenske, G.R.**, (2005), "Evidence of Scuffing Initiation by Adiabatic Shear Instability," Wear, Vol. 258, pp. 1471-1478.

[36] **Hertz, H.**, (1881), "Über die Berührung fester elastischer Körper," Journal für die reine und angewandte Mathematik, Vol. 92, pp.156-171 (in German).

[37] **Horng, J.H.**, (1998), "True Friction Power Intensity and Scuffing in Sliding Contacts," ASME Journal of Tribology, Vol. 120, pp. 829-834.

[38] **Horng, J.H., Lin, J.F. and Li, K.Y.**, (1996), "Scuffing as Evaluated from the Viewpoint of Surface Roughness and Friction Energy," ASME Journal of Tribology, Vol. 118, pp. 669-675.

[39] **Johnson, K.L.**, (1999), "Contact Mechanics," Cambridge, UK.

[40] **Ku, P.M., Staph, H.E. and Carper, H.J.**, (1978), "On the Critical Contact Temperature of Lubricated Sliding-Rolling Disks," ASLE Transactions, Vol. 21, 2, pp. 161-180.

[41] **Ku, P.M., Staph, H.E. and Carper, H.J.**, (1978), "Frictional and Thermal Behaviors of Sliding-Rolling Concentrated Contacts," Journal of Lubrication Technology, Vol. 100, pp.121-128.

[42] **Landheer, D. and Gee, A.W.J. de**, (1994), "Tribologie – deel A: Inleiding dynamische contactverschijnselen," Lecture notes, University of Twente, The Netherlands (in Dutch).

[43] **Lim, S.C. and Ashby, M.F.**, (1987), "Wear-mechanism Maps," Acta Metall., Vol. 35, pp. 1-24.

[44] **Lim, S.C., Ashby, M.F. and Bruton, J.H.**, (1987), "Wear-rate Transitions and their Relationship to Wear Mechanisms," Acta Metall., Vol. 35, pp. 1343-1348.

[45] **Matveevsky, R.M.**, (1965), "The Critical Temperature of Oil with Point and Line Contact Machines," Trans. AMSE/Journal of Basic Engineering, Vol. 87, pp.754-760.

[46] **Meng, V.V.**, (1960), "The Investigation of Steel Seizure with Disc Machine," Friction and Wear of Machines, Vol. 14, pp. 222-327.

[47] **Metselaar, H.S.C.**, (2001), "Thermally Induced Wear Transition in Ceramics," Ph.D. thesis, University of Twente, The Netherlands.

[48] **Pasaribu, H.R.**, (2005), "Friction and Wear of Zirconia and Alumina Cermanics Doped with CuO", Ph.D. thesis, University of Twente, The Netherlands.

[49] **Rooij, M.B. de**, (1998), "Tribological Aspects of Unlubricated Deepdrawing Processes," Ph.D. thesis, University of Twente, The Netherlands.

[50] **Schipper, D.J.**, (1988), "Transitions in the Lubrication of Concentrated Contacts," Ph.D. thesis, University of Twente, The Netherlands.

[51] **Schipper, D.J. and Gee, A.W.J. de**, (1995), "Lubrication Modes and the IRG Transition Diagram," Lubrication Science, Vol. 8-1, pp. 27-35.

[52] **Schipper, D.J., Steenmeijer, R.C. and Gee, A.W.J. de**, (1994), "The Effects of Variations in the Procedure of Loading on the Load Carrying Capacity of Thin Film Lubricated Concentrated Contacts," Proceedings of the 4th International Tribology Conference, Austrib94, Vol. I, pp. 105-112, ISBN 0 646 21097 1.

[53] **Spikes, H.A. and Cameron, A.**, (1974) "A Comparison of Adsorption and Boundary Lubricant Failure," Proc. Roy. Soc., London, Series A336, pp. 407-419.

[54] **Tabor, D.**, (1951), "The Hardness of Metals," Oxford University Press, UK.

[55] **Wang, Y., Lei, T., Yan, M. and Gao, C.**, (1992), "Frictional Temperature Field and its Relationship to the Transition of Wear Mechanisms of Steel 52100," J. Phys. D: Appl. Phys., Vol. 25, pp. A165-169.

[56] **Visscher, H.**, (2001), "On the Friction of Thin Film Rigid Disks," Ph.D. thesis, University of Twente, The Netherlands.

[57] **Yang, J., R.S. Cowan and Winer, W.O.**, (1993), "Prediction of Failure Transitions in Sliding Contacts by a Thermomechanical Wear Model," ASME Journal of Tribology, Vol. 115, pp. 432-438.

[58] **Yu, H., Liu, S. and Chung, Y.-W.**, (2004), "Influence of Temperature-dependent Yield Strength on Thermomechanical Asperity Contacts," Tribology Letters, Vol. 17, No. 2, pp. 155-163.

[59] **Zhang, C., Cheng, H.S. and Wang, Q.J.**, (2004), "Scuffing Behavior of Piston-Pin/Bore Bearing in Mixed Lubrication – Part II: Scuffing Mechanism and Failure Criterion," STLE Tribology Transactions, Vol. 47, pp. 1-8.

[60] **Zhao, Y., Maietta, D.M. and Chang, L.**, (2000), "An Asperity Microcontact Model Incorporating the Transition from Elastic Deformation to Fully Plastic Flow," ASME Journal of Tribology, Vol. 122, pp. 86-93.